Synthesis and Validation of Vision Based Spacecraft Navigation

Massaro, Alessandro Salvatore

Publication date:
2013

Document Version
Publisher's PDF, also known as Version of record

Synthesis and Validation of Vision Based Spacecraft Navigation

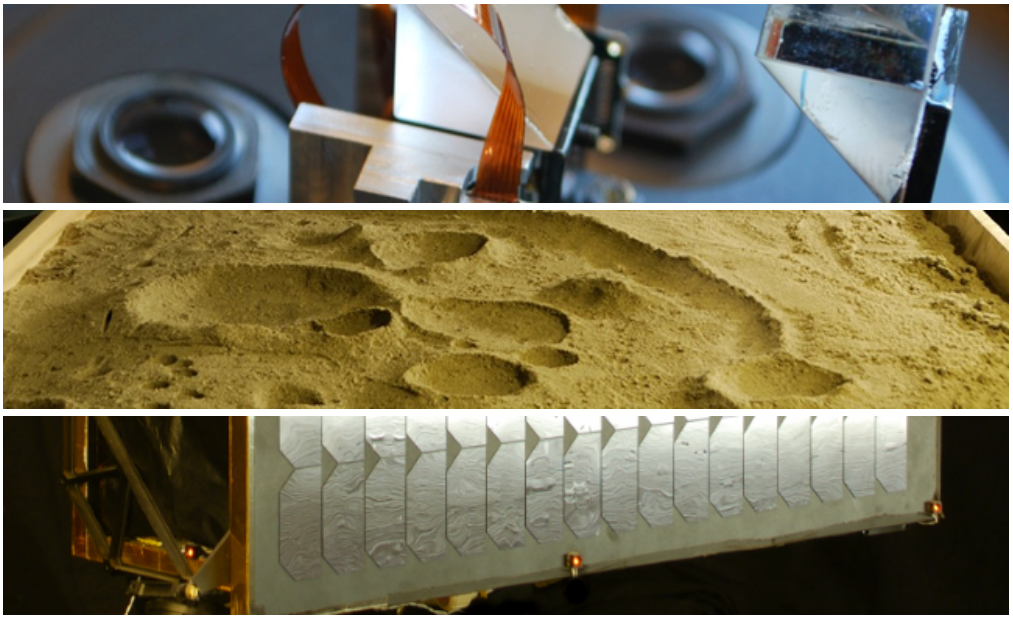

Alessandro S. Massaro

Ph.D. Dissertation
May 2013

DTU Space
National Space Institute

Synthesis and Validation of Vision Based Spacecraft Navigation

Alessandro S. Massaro

Ph.D. Dissertation
May 2013

Technical University of Denmark
DTU Space – National Space Institute
Measurement and Instrumentation Systems
Building 327, DK-2800 Kgs. Lyngby
Phone: +45 4525 3438, Fax: +45 4588 7133
www.space.dtu.dk

Colophon

This dissertation was typeset with LaTeX 2$_\varepsilon$ using the *memoir* document class and compiled with MiKTeX v2.9.3888 within the Texmaker editor. The manuscript has been prepared for 17×24 cm format with two-side, open-right printing.

Graphs, figures and diagrams have been produced personally using the following tools: MathWorks MATLAB, Microsoft Visio, Autodesk Inventor, GIMP and Blender. External sources are referenced, where applicable.

"Passion starts the journey and discipline guides around the curves."

Abstract

This dissertation targets spacecraft navigation by means of vision based sensors. The goal is to achieve autonomous, robust and efficient navigation through a multi-disciplinary research and development effort, covering the fields of computer vision, electronics, optics and mechanics.

The attention of space organizations worldwide, both public and private, is once again directed at our natural satellite. The Moon offers an unimaginably rich reservoir of resources exposed on its surface; a prime example being Helium-3. Furthermore, its distance from Earth's electromagnetic interferences and its lack of atmosphere make it a naturally optimal location for scientific observation of Earth and outer space. Finally, it is an ideal location for establishing outposts for deeper Solar System exploration. Despite the successful endeavours of the past century, direct or remote manned operation of vehicles directed to the Moon's surface is still prohibitively expensive and not ideal for missions such as cargo delivery. The first part of this book focuses on a lunar landing scenario as case study and discusses software and hardware components for an optimal vision based sensor for precision planetary landing. Computer vision techniques are applied to the problems of horizontal velocity estimation, and hazard detection. Experimental implementations are henceforth presented and the results show their potential for integration on a space qualified processing unit. The study concludes with recommendations for key physical parameters of the camera system.

In connection with the PRISMA experimental mission for rendezvous and docking and formation flight, DTU Space has implemented, flown and validated the Vision Based Sensor (VBS). This sensor has required development of novel techniques for calibration of the target optical model and custom hardware verification tools, both described in this book. One such tool personally developed is Pharos, an electro-opto-mechanical stimulator that physically interfaces with the camera to simulate the conditions of far range rendezvous in space. Pharos is now also being used by the Department to verify algorithms for asteroid detection, installed on the Juno spacecraft on its way to Jupiter.

Another important outcome of the R&D effort of this project has been the integration of a calibration and validation facility for the vision based sensors developed at DTU Space. The author's work has covered all phases from concept to design and construction of the laboratory, which is equipped with precise manipulators and a controlled lighting setup in order to simulate the kinematics and optical conditions under which the sensors will operate. Testing of sensors and algorithms for the upcoming ESA PROBA-3 mission is currently under way. The laboratory also includes a physical analog terrain for verification of planetary landing algorithms.

The general methods of autonomous navigation investigated and described in this book have also been applied to two external projects. The research stay at the NASA Ames Research Center's Intelligent Robotics Group (ARC-IRG) resulted in the successful implementation of an infrastructure-free global localization algorithm for surface robotic navigation. The algorithm is now integrated with other rover navigation routines developed by IRG. Finally, collaboration with DTU Automation culminated in the development of a novel terrain mapping and obstacle detection technique based on Gaussian processes. These results have been published on a peer-reviewed conference paper at the 2011 IEEE International Conference on Machine Learning and Applications.

Project supervisor:

Head of Section, Professor John Leif Jørgensen

DTU Space – Measurement and Instrumentation Systems

Resumé

Denne afhandling er rettet mod navigering af rumfartøjer ved hjælp af billed sensorer. Målet er at opnå selvstændig, robust og effektiv navigation gennem en tværfaglig R&D indsat, der omfatter områder som computer vision, elektronik, optik og mekanik.

Verdens rumorganisationer, både offentlige og private, fokusere nu deres opmærksomed imod vores naturlige satellit. Månen tilbyder et ufatteligt rigt reservoir af ressourcer på dens overflade, f.eks. Helium-3. Desuden gør afstanden fra Jordens elektromagnetiske interferens og manglen på atmosfære den til en naturlig optimal placering for videnskabelig observation af Jorden og det ydre rum. Endelig er det et ideelt sted for oprettelse af forposter til videre eksploration af solsystemet. På trods af de vellykkede bestræbelser i det sidste århundrede er direkte eller fjern bemandet styring af rumfartøjer, der er rettet mod Månens overflade, stadig uoverkommeligt dyre, og ikke ideel til opgaver som nyttelast levering. Den første del af denne bog fokuserer på et månelandings scenario som case studie og diskuterer software og hardware komponenter for en optimal visionbaseret sensor til præcisionsplanetlanding. Computer vision teknikker anvendes på problemer som horisontal hastigheds vurdering og detektion af farlige forhindringer. Eksperimentelle implementeringer er nu fremlagt, og resultaterne viser deres potentiale til integration på en rum kvalificeret computer. Undersøgelsen slutter med anbefalinger af fysiske nøgle parametre i kamerasystemet.

I forbindelse med den eksperimentelle PRISMA mission til rendezvous og docking og formations flyvning, har DTU Space gennemført, fløjet og valideret Vision Based Sensoren (VBS). Denne sensor har krævet udvikling af nye teknikker til kalibrering af den optiske model og specifikke hardware verifikationsværktøjer, som er beskrevet i denne bog. Et sådant personligt udviklet værktøj er Pharos, en elektro-opto-mekanisk stimulator, der fysisk har grænseflader med kameraet for at simulere betingelserne for rendezvous på langt afstand i rummet. Pharos bruges nu også i afdelingen for at teste de algoritmer til asteroide detektering som er installeret på Juno rumfartøjet på vej til Jupiter.

Et andet vigtigt resultat af dette forskningsprojekt har været integrationen af en kalibrering og valideringsfacilitet for DTU Spaces VBS. Forfatterens arbejde har dækket alle faser fra koncept til design og konstruktion af dette laboratorium, som er udstyret med præcise manipulatorer og en kontrolleret belysning til at simulere de samme kinematiske og optiske betingelser hvorunder sensorerne skal operere. Test af sensorer og algoritmer til den kommende ESA PROBA-3 mission er nu i gang. Laboratoriet omfatter også et fysisk analog terræn til verifikation af planetlandings algoritmer.

De generelle metoder til autonom navigation, der er undersøgt og beskrivet i denne bog, er også blevet anvendt til to eksterne projekter. Udlandsopholdet på NASA Ames Research Center Intelligent Robotics Group (ARC-IRG) resulterede i en vellykket gennemførelse af en infrastruktur-fri global lokaliseringsalgoritme til overflade robot navigation. Algoritmen er nu integreret med andre rover navigation-srutiner udviklet af IRG. Endelig, kulminerede samarbejde med DTU Automation i udviklingen af en ny terrænkortlægning og teknik til detektering af forhindringer baseret på Gaussprocesser. Disse resultater er blevet offentliggjort i en peer-reviewed konference artikel på 2011 IEEE International Conference on Machine Learning and Applications.

Projektvejleder:
Sektionsleder, Professor John Leif Jørgensen
DTU Space – Måling og Instrumentering

Preface

This dissertation is submitted in partial fulfilment of the requirements for obtaining the Ph.D. Degree at the Technical University of Danmark (DTU). The work described herein has been conducted at Measuring and Instrumentation Systems – DTU Space, under the Ph.D. program of Electronics, Communication and Space Science.

Acknowledgements

I am very grateful to John, for giving me the opportunity to embark on this very exciting and formative voyage.

A thank you to all by-goers of the Ph.D. office, present and past, for all the good times. More so to Jack, for his workshop expertise, and to David for his help in revising this book.

The friendliness and support from the rest of MIS colleagues on matters of research, development or cake relishing was also much appreciated. A direct thanks to Fritz for reviewing the Danish Resumé included above.

I would also like to thank Dr. Terry Fong at NASA ARC for hosting me and the rest of the IRG group for the good comradeship, particularly the guys at the Pirate Lab and the Advanced Nav group.

I will also acknowledge my friends Morten and Enis at DTU Automation for the good work and fruitful cooperation.

Further, I am grateful to Otto Mønsted Fond for contributing to the expenses for the conference and external stays undertaken during this period.

Finally, I am obliged to my family for being always close and supportive, even from afar.

Contents

List of Figures

List of Tables

Nomenclature

TYPOGRAPHICAL CONVENTIONS

The citations and references format used throughout this book consists of the first one to two authors' last name, followed by the year of publication as in Massaro (2009). Where more than two authors are present, the *et al.* suffix is added after the first author, replacing all the following. All citations and references have been included in the Bibliography at the end of the book.

Figures, tables and equations are numbered incrementally and by chapter. A list of figures and tables is included after the table of contents. Angles are defined with the Greek alphabet set. The period sign marks a decimal point and no space separator is used for large quantities (e.g. 1737.5 km).

The notation uses bold letters for matrices and vectors, respectively in upper and lower case, as in the following examples. All quantities are reported in SI units, unless otherwise noted.

$$\mathbf{f} = m\mathbf{g} \tag{1}$$

$$\mathbf{p}' = \mathbf{R} \cdot \mathbf{p} + \mathbf{t} \tag{2}$$

ACRONYMS AND ABBREVIATIONS

The acronyms and abbreviations used throughout the book are listed below. Optional affixes are marked within parentheses.

(μ)ASC	(micro) Advanced Stellar Compass
AU	Astronomical Unit
BRDF	Bidirectional Reflectance Distribution Function
CHU	Camera Head Unit
DEC	DEClination
DTU	Technical University of Denmark (Danish acronym)
DOF	Degree(s) Of Freedom
EDL	Entry, Descend and Landing
EGSE	Electrical Ground Support Equipment
ESA	European Space Agency
FF	Formation Flight
FOV	Field Of View
FPS	Frames Per Second
FWC	Full Well Capacity
GNC	Guidance, Navigation and Control
IMU	Inertial Measuring Unit
JAXA	Japan Aerospace Exploration Agency
JPL	Jet Propulsion Laboratory
LEO	Low Earth Orbit
LIDAR	LIght Detection And Ranging
MER	Mars Exploration Rover
MOHVE	MOnocular Horizontal Velocity Estimator
MOSARD	MOnocular SAfe Region Detector
MSR	Mars Sample Return
NASA	National Aeronautics and Space Administration
OGSE	Optical Ground Support Equipment
PPL	Precision Planetary Landing
PRISMA	Prototype Research Instruments and Space Mission technology Advancement
PROBA	PRoject for On-Board Autonomy
RA	Right Ascension
RANSAC	RANdom SAmple Consensus
ROI	Region Of Interest
RV(D)	RendezVous (and Docking)
TD	Terminal Descent
TRL	Technological Readiness Level
TRN	Terrain Relative Navigation
VBLS	Vision Based Landing Sensor
VBS	Vision Based Sensor

TERMINOLOGY AND DEFINITIONS

Accuracy	A measure of closeness of a measurement to the true value.
Arcsecond	An arcsecond is a sub-unit of angular measurement defined as $\frac{1}{3600}$ parts of a degree and represented by the symbol ["].
Attitude	The orientation of an object or coordinate system. Can be absolute or relative when it is expressed respectively w.r.t. a fixed reference frame or a moving coordinate system.
Irradiance	The total incident power per unit of surface area $[W\,m^{-2}]$. Used to represent light arriving at a surface.
Outlier	An observation that appears to deviate considerably from other elements of a data set/sample.
Radiance	The power travelling at a point in a direction per unit of area (perpendicular to the direction of travel) and solid angle $[W\,m^{-2}\,sr^{-1}]$. Used to represent light travelling in free space or reflected from a surface.
Radiometry	The field of optics measuring electromagnetic radiation.
Precision	Also known as repeatability, is the degree to which repeated measurements show the same results.

PHYSICAL CONSTANTS AND QUANTITIES

Gravitational constant	$G = 6.673 \times 10^{-11}\,m^3\,kg^{-1}\,s^{-2}$
Planck constant	$h = 6.626 \times 10^{-34}\,J\,s$
Boltzmann constant	$k_B = 1.381 \times 10^{-23}\,J\,K^{-1}$
Speed of light	$c = 2.998 \times 10^{8}\,m\,s^{-1}$
Mass of the Sun	$M_S = 1.989 \times 10^{30}\,kg$
Radius of the Sun	$R_S = 6.963 \times 10^{8}\,m$
Mass of the Earth	$M_E = 5.974 \times 10^{24}\,kg$
Radius of the Earth	$R_E = 6.378 \times 10^{6}\,m$
Mass of the Moon	$M_M = 7.348 \times 10^{22}\,kg$
Radius of the Moon	$R_M = 1.737 \times 10^{6}\,m$
Astronomical unit	$AU = 1.496 \times 10^{11}\,m$

CHAPTER 1

Introduction

This first chapter opens up the book by introducing the background and raison d'etre of the project. It includes an outline of the current state of the art of vision based navigation for science and exploration and discusses prospects on upcoming and future missions. Finally, the scope and content of the dissertation is described.

1.1 BACKGROUND

Space sciences and technology have the potential to improve human life across the board. Our natural desire for exploration and thirst for knowledge can be unleashed against the infinite horizon before us. Space travels will help us expand our presence in the Solar System and beyond. Unravelling the secrets of space physics and weather will improve our understanding of the effects on us and our home planet. Harvesting exotic resources will support our endeavours. New engines will power our ships towards distant stars.

All of it can be achieved, one piece of technology after the other. Autonomous systems can improve safety, efficiency and precision. The complex problems of space flight dynamics can be solved by computers in fractions of seconds and with high precision, thereby enabling the deployment of new technologies where human presence is undesired or simply impractical. Whether it is delivering cargo to the International Space Station (ISS) or on the surface of a distant planet, autonomous navigation systems will be desired. Ideally, entire space stations (if not ground bases) could be transported and assembled to other planets prior to humans' arrival. In order to gain perception of the environment in which they operate, these systems

require sensors. One particular category, which is by no coincidence outfitted on essentially every single evolved living being on Earth, is the vision based sensor. In space, vision based sensors can be utilized on a wide range of mission classes:

- Rendezvous and docking (RVD) of spacecraft, for orbital inspection, servicing or even construction of satellites;
- Formation flight (FF), for deploying large aperture scientific telescopes;
- Precision planetary landing (PPL) and surface navigation.

PRISMA was the first civilian experiment of its kind for the validation of navigation systems and sensors for FF and RVD. Missions specifically designed for high precision formation flight are already under development. The solar coronagraph PROBA-3 mission is a good example of a scientific experiment benefiting from the technological advances introduced by the PRISMA VBS sensor.

Undeniably, the interest of space agencies worldwide for planetary exploration is high. Scientific and technological demonstration missions are expected to be launched towards the Moon and Mars in the next years. Mars sample return (MSR) is still a major goal for ESA and NASA. The outlook for the time frame 2013 to 2020, is filled with missions with landing capabilities targeting the Moon: JAXA's SELENE-2, ESA's Lunar Lander, the Chinese CHANG'E-3 and 4, the Indian CHANDRAYAAN-3 and the Russian LUNA-GLOB. In addition, Google's X-Prize might reserve some surprises.

1.2 SCOPE OF DISSERTATION

The scope of this dissertation is to provide optimal solutions to the development of robust and efficient vision based autonomous navigation sensors. In this book I target two specific aspects. The first is a feasibility study for the development of an optimal awareness sensor for lunar precision planetary landing, based on a background scene and constraints analysis. A study of the theoretical background in computer vision and optics is applied to key problems that the landing spacecraft faces under this scenario. Experimental solutions will be discussed, focused on reliability and execution time.

The second part of this book is focused on the subject of calibration and validation (C&V). Calibration is of utmost importance for producing precise metrology, although with the design of a new class of instrument, such as the PRISMA VBS, novel techniques have to be devised. Validation is essential for ensuring that the instrument will perform according to the specifications when operative. This is done under circumstances that mimic the real world scenario with the highest fidelity achievable on ground. The report thus documents the efforts undertaken for the development of software and hardware tools towards improved sensor performance and reliability.

The dissertation holds four main chapters:

- Chapter 3 reports study and proposed solutions to the precision planetary landing case study.
- Chapter 4 reports developed algorithms and techniques for calibrating the PRISMA VBS target optical model.
- Chapter 5 reports the design and development of the Pharos OGSE tool for far range optical stimulation of the VBS camera.
- Chapter 6 reports the design and integration of the calibration and validation facility for vision based sensors.

1.3 SUPPLEMENTARY WORK ON SURFACE NAVIGATION

This section recounts additional work performed during the course of the Ph.D. study period that is not treated in this book, but is still very relevant to the field of spaceborne vision based navigation. The subject is robotic surface navigation, directed at two classical problems: terrain mapping and global localization. Robots are proposed by all space agencies as precursors and eventually assistants to all future manned exploration missions, as well as several unmanned scientific missions. These machines, typically dubbed rovers for their motive capabilities, can address cheaply and safely tasks of survey, analysis and reconnaissance. While very promising, robots still have some way to go before competing with humans in situ, in terms of timeliness when performing their tasks. The development of optimized algorithms for a faster, robust and fully autonomous execution of their functions is a major milestone in this direction. The two methods are described below.

1.3.1 A Method for Terrain Mapping and Obstacle Detection

Human remote operation of vehicles stationed at remote locations around the Solar System should be minimised due to the high running costs and low efficiency due to the long communication delays. Autonomous terrain mapping is one among several primary functions, required by robots to autonomously and safely navigate through remote unstructured landscapes. Little or lacking previous knowledge is available about the terrain morphology and the potential hazards for the safety of the vehicle. Sensing and interpretation of the surrounding environment is achieved by equipping the vehicle with a suite of instruments for acquiring the necessary information (typically in the form of 3D point clouds of terrain physical locations). This data is naturally subject to noise and uncertainty, affected by systematic or random errors.

A joint research effort with the department of DTU Automation resulted in the project described here. The idea behind this project was to find a simple way to

represent the map and hazard information while maintaining the estimate uncertainty. An investigation identified Gaussian processes as a valid candidate for a probabilistic approach to the problem. A following implementation was built upon the theory of Gaussian Process Regression (GPR), and verified on real world data acquired with LIDAR and stereo camera sensors on structured and unstructured terrains. A heuristic approach is used for obstacle classification, from the detection of discontinuities in the terrain. The results, published in Kjaergaard et al. (2011), show that the algorithm is able to estimate a correct surface map and identify obstacles, given operator defined parameters, with both data sets. In the documented naive implementation, the process results in sub optimal execution time, although there is still considerable room for further optimization.

1.3.2 A Method for Global Surface Localization

The problem of localization on Earth is nowadays relatively simple, thanks to global satellite positioning systems. This infrastructure provides very accurate 3D localization information at virtually any place on the planet's surface. Although most robotic systems nowadays are equipped with the associated sensors, vehicles developed for navigation over other celestial bodies will not have positioning satellites at their disposal, at least in the short term. The focus of my external stay at the NASA Ames Research Center Intelligent Robotics Group (ARC IRG - Moffett Field, CA) has been to implement an algorithm for global infrastructure-free localization of a rover.

Localization cannot be solved without knowledge of the surrounding terrain, in the form of a map or a collection of distinguishable landmarks. Thanks to laser altimeters equipped on reconnaissance spacecrafts such as the lunar LRO and martian MRO, digital elevation maps (DEM) are easy to obtain. By matching a reference map point cloud with a sensor point cloud, representing the surroundings of the vehicle, it is possible to obtain localization information with high accuracy[1] on a non flat terrain. This technique, commonly known as registration, consists in the alignment of one data set over the other with six degrees of freedom. The iterative closest point (ICP) algorithm is a robust and accurate method to solve this problem by iteratively minimizing an appropriate error metric. ICP was first described by Besl and McKay (1992) and is, to date, known in two variants: point to point ICP and point to plane ICP, depending on the error metric used. A simple implementation of the first has been evaluated during the project, while core components of the point to plane ICP have been developed. The algorithm has finally been tested with terrain data – from LIDAR and stereo cameras – gathered on a lunar analog site by the IRG rover team and has been validated with GPS ground truth data.

[1] The accuracy can, at best, be as good as the map resolution.

CHAPTER 2

Theory

This chapter briefly covers background theoretical notions of relevance for the following study.

2.1 SURFACE REFLECTANCE

The light collected by an image sensor targeting a surface is dependent on the light falling on the surface and the portion being reflected towards the sensor. The geometry is described in Figure 2.1. If **n** is the surface normal vector, the problem is defined by the three angles of incidence θ_i, emittance θ_e and phase. In technical terms: "scene radiance depends on the amount of light that falls on a surface and the fraction of the incident light that is reflected" (Horn, 1986). The ratio of radiance to irradiance is defined as

$$f(\theta_i, \phi_i; \theta_e, \phi_e) = \frac{\delta L(\theta_e, \phi_e)}{\delta E(\theta_i, \phi_i)} \tag{2.1}$$

and is referred to as bidirectional reflectance distribution function (BRDF). The angles ϕ_e and ϕ_i are the azimuth angles that completely define the pointing directions. A simple case is a Lambertian surface, which appears equally bright from all viewing directions, reflecting all incident light. Its BRDF is $1/\pi$ and the commonly known cosine reflection law is

$$L = \frac{1}{\pi} E \, cos\theta_i \tag{2.2}$$

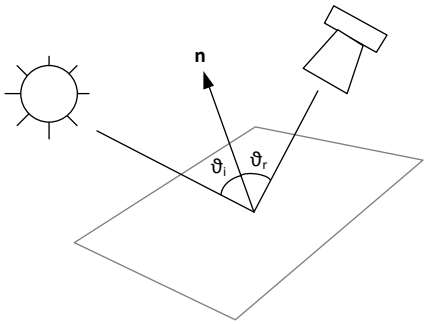

Figure 2.1: Geometry of incident and reflected light rays on a surface with normal **n**.

For $\theta_i \geq 0$. In general, scene brightness is also determined by intrinsic material properties of the surface (composition, granularity and roughness) and surface topography. These properties can be modelled theoretically or by experimental observations. General parametric methods were found in the literature for modelling surface reflectance, which incorporate most of the aforementioned properties. These will be discussed further in Section 3.3.2.

2.2 CCD NOISE MODEL

Optical imaging sensors are subject to noise effects at each stage of image formation (see 2.2). Specifically to a CCD sensor, we can identify three primary components of noise: photon noise, dark current noise and read noise. Photon (or shot) noise results from inherent quantum fluctuations of the incoming photons and obeys a Poisson distribution. This is normally modelled as the square root of the signal. Dark current is the contribution of electrons released by thermal energy on the silicon structure. This effect can be controlled by cooling down the camera. Read noise derives from the conversion of charge carriers to voltage and the following process of A/D conversion. Proper electronics design helps reducing this effect. Read noise and other sources, such as bias, can often be neglected. The signal to noise ratio can be calculated as follows

$$SNR = \frac{S}{N} = \frac{N_{e^-}}{\sqrt{N_{e^-} + Dt + N_r^2}} \tag{2.3}$$

where N_{e^-} is the number of electrons released on the sensor by the light signal, and the three noise components just described at the denominator. D is the dark current and t the integration time.

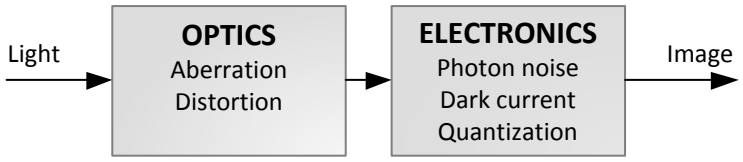

Figure 2.2: Some examples of the noise components introduced in the image formation process at each step.

2.3 NOTIONS OF COMPUTER VISION

The development of algorithms requires, just like any other procedure, trade off analysis of the various aspects involved in the design. Real world constraints are often defining boundaries to all measures of performance and therefore demand approximations. Three main aspects are affected and influencing each other: computational efficiency, accuracy of the approximation and ease of implementation. While high computational efficiency is desirable to improve performance, the implementation may be overly complex and beyond the capabilities of the available hardware. High demands in terms of accuracy of the result in turn, have a negative impact on efficiency. The developer's task is to find the optimal balance.

2.3.1 Low Level Features Extraction

Feature extraction (or detection) is a common first step in computer vision algorithms. These features represent points or regions of interest on the observed scene, which the computer identifies and processes in order to extract objective properties, depending on the task at hand. Point and corner features are found in all types of scenes and are particularly abundant and well distributed when capturing unstructured natural terrains.

Shi and Tomasi (1994) were the first to describe the need for good features to track. A good feature should be, at least, robust to changes in brightness, scale and rotation. Together, these properties define the stability of a feature. To complicate things, detectors have to be fast, to keep up with real time systems operations. Many variants of extraction algorithms for different kind of features are documented in the literature. The simplest features – geometrically – are points and corners. The most recognized detectors for these are SIFT (Lowe, 2004) and Harris (Harris and Stephens, 1988). Both are very robust and repeatable. SIFT points are scale and rotation invariant due to the scale space analysis that makes up the extraction process and the use of a rotationally invariant operator. Harris corners are robust

to lighting changes but not scale invariant. Among the two, SIFT is considerably more computationally demanding.

The need for speed for real time operations and rapidly varying scenes such as planetary landing, puts more pressure for fast feature extraction algorithms. Despite the overall comparable quality and stability to previous methods, the most recent FAST algorithm (Rosten and Drummond, 2006) stands out for its high speed and simple implementation. FAST requires much less computation power than the competition and also outperforms SURF, another speed focused variant of SIFT. Figure 2.3 shows the features extracted with various algorithms. Note the abundance of points close to detailed regions and the absence over smooth featureless regions.

In order to improve robustness and assist in the search of correspondences – described below – most detectors enrich the features with a descriptor. Descriptors vary between methods, but typically include additional information, such as orientation and scale of a feature.

2.3.2 Features Tracking

Feature tracking, also known as *correspondence problem*, is the process of determining correspondences between features extracted from two or more images. If the images are of the same scene from different points of view, the lines joining a matched pair of features are motion vectors describing the transformation between one image frame and the other. A common distinction is done between direct – pixel based – methods, and indirect – feature based – methods. The two approaches are contended in Irani and Anandan (1999) and Torr and Zisserman (1999). The quality of a match, and therefore likelihood that it represents the correct correspondence, is commonly evaluated by minimizing an error metric, for example: sum of absolute differences (SAD) or sum of squared errors (SSE). The cited papers describe pixel based methods as easy to implement and enabling dense image matching, but highlight their cost as the error is evaluated m^2 times, where m is the side length of the search window. Feature based methods are much faster because the error is evaluated only once for each pair of feature kernel. Furthermore, as features have a wide range of photometric invariance, indirect methods are robust to severe viewing and photometric variations and are thus more robust for motion recovery problems.

The most common direct method for feature tracking is the block-matching algorithm (BMA), where a block of n×n pixels from one image is searched in the second image using one of the metrics mentioned above. If no a priori knowledge of the camera motion is known, this method can be extremely costly. It is also possible to improve sensitivity to brightness changes by applying normalized correlation instead. The normalization is obtained by subtracting the patch mean brightness and dividing by the standard deviation as

$$\frac{I - \mu}{\sigma} \tag{2.4}$$

The FLANN algorithm (Muja and Lowe, 2009) applies an approximate nearest neighbour search to improve the speed of feature correlation and is reportedly much faster than any previous ANN method. FLANN is a feature based method and operates only on feature descriptors. Due to its approximate nature it is more prone to errors, though simple outlier filters can easily make up for false matches.

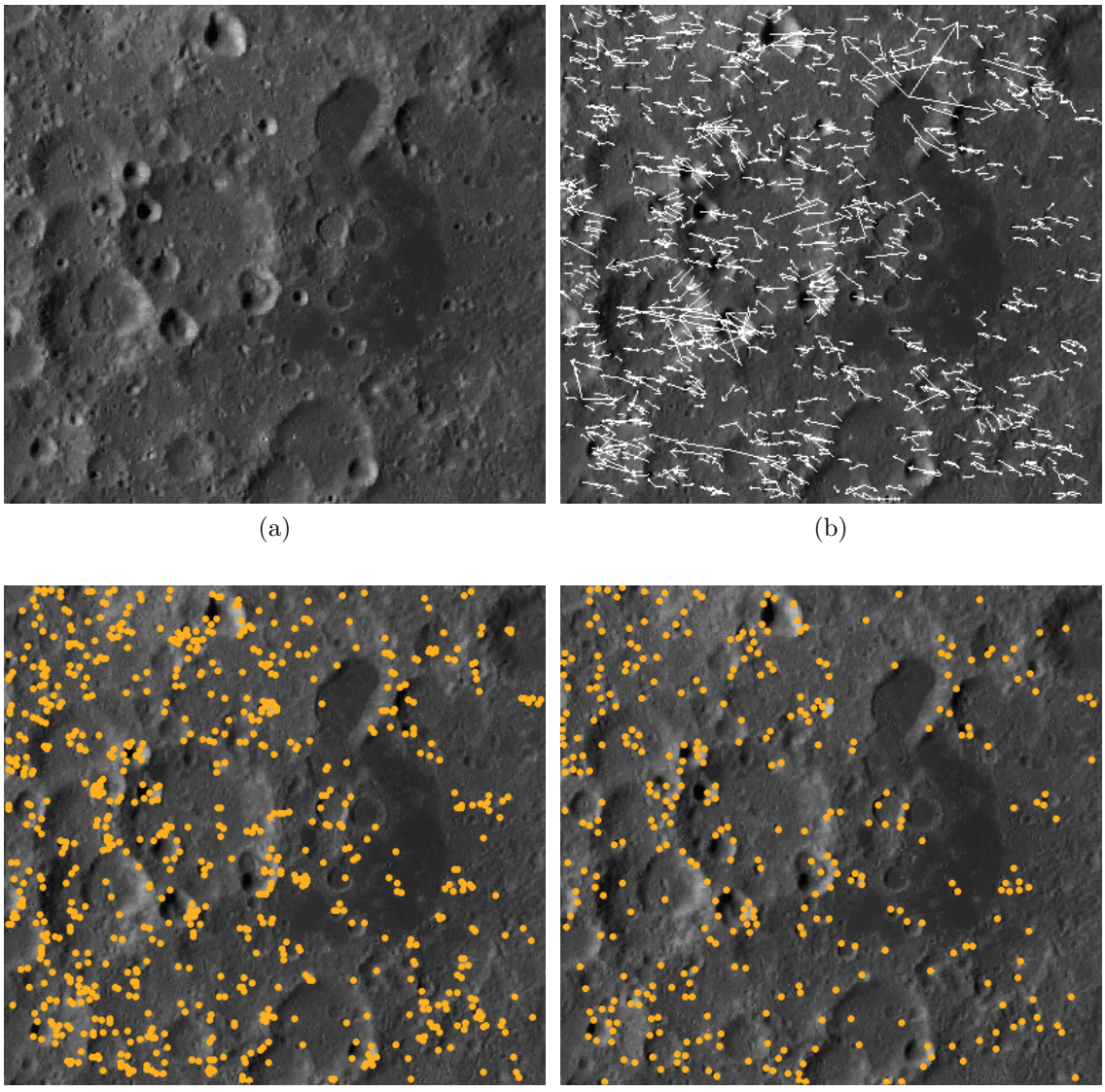

(a) (b)

(c) (d)

Figure 2.3: Demonstration of the result of applying some common features extraction algorithms. (a) Original Image. Location: Titius crater. (b) SIFT: each feature point is enriched by a scale and orientation descriptor. (c) FAST: with non-maxima suppression and threshold at 40. (d) Harris: limited at about 300 features.

CHAPTER 3

Case Study: Precision Planetary Landing

Developing safe, precise and autonomous planetary landing systems is a primary milestone for the exploration of the Solar System. This technology can haste and dramatically increase the reliability of manned or unmanned vessels landing on a remote planetary body. This chapter covers a study and proposed algorithms for the design of an optimal vision based sensor applied to this problem.

3.1 BACKGROUND

Precise planetary landing is considered by NASA and ESA among the key technologies to be developed in the near future, as outlined in the document *Solar System Exploration Roadmap*[1]. Many of the upcoming missions directed at other planets of the Solar System will benefit from sensors and control systems capable of driving the spacecraft safely within close range of pre-determined surface objectives, therefore minimizing risk and optimizing the operations time frame. Destinations include: Mars, Venus and Europa, to name a few. Our Moon has come again under the lens, as it offers safe ground for establishing forward bases for scientific experiments or harvesting exotic resources that are rare or unavailable on Earth. Before pushing forward with human exploration of space, there are still some activities to be performed to ensure sustainable exploration. Key is the understanding of long term effects of space travels on the human body and the provision of resources to guar-

[1] `http://solarsystem.nasa.gov/multimedia/downloads/SSE_RoadMap_2006_Report_FC-A_med.pdf`

antee survivability and effective transportation of cargo to these remote locations (Carpenter et al., 2010).

Performing entry, descent and landing (EDL) of unmanned vehicles on a planet distant millions of kilometres, makes human remote operation impossible and requires autonomous real-time on-board processing of the sensors' data, to accurately determine the spacecraft's attitude, pose and velocity relative to the planetary surface. Continuous developments of EDL technology at JPL (NASA) have resulted in the reduction of the landing error ellipse from hundreds of kilometres with Viking in 1976, to just a few kilometres on the 2012 Curiosity landing (Figure 3.1). This feat was made possible by integrating in the design a set of complementary sensors, working in synergy to provide a broader awareness of the environment.

The study documented in this chapter has focused on vision based sensors. These sensors have many advantages for the scope of spacecraft navigation: light weight, low power consumption, minimal number of mechanical parts and can be made fast end efficient with the use of appropriate algorithms. Laser rangers are usually seen as antagonists to cameras, for they can generate precise high resolution point clouds from range measurements, even from high altitude. On the downside, they are bulky and delicate instruments, with higher power consumption and generally limited field of view. As precision landing requires high responsiveness and continuity in determining the spacecraft's pose, position and velocity, these instruments can be supported by inertial sensors. Inertial measurement units (IMU) have been traditionally used standalone for lunar landers since the Apollo Program (based on mechanical gyroscopes). Fusion of modern IMUs with cameras, augments the vision processed pose information with an independent and more direct measurement. One of the major benefits is a correct estimate even when ambiguous solutions occur, e.g. due to the aperture problem. Section 3.1.2 discusses some of the methods that can be employed to enable terrain relative navigation.

Identification of hazards to the safety of the vehicle is another major area of interest for navigation and particularly so in the brisk time-constrained scenario of planetary landing. A hazard can be any object or surface feature which may cause direct damage to the spacecraft body by impact (in the case of large rocks) or by preventing nominal operation after landing. The latter case may occur if the vehicle lands on a high slope, causing excessive tilt, or falls into cliffs, craters or basins which prevent proper alignment of the instrumentation for communication, operation and energy supply (in the case of solar panels). Hazard detection and avoidance is therefore a necessary element for increasing safety and improving landing site characterization. Section 3.4 reports further considerations and proposed algorithms for performing rapid and reliable hazard detection. Avoidance is a matter for the control systems and is thus not covered here.

A lunar lander scenario was considered as reference case study and is the target of the following analysis. Realistic sensor parameters and architecture are discussed

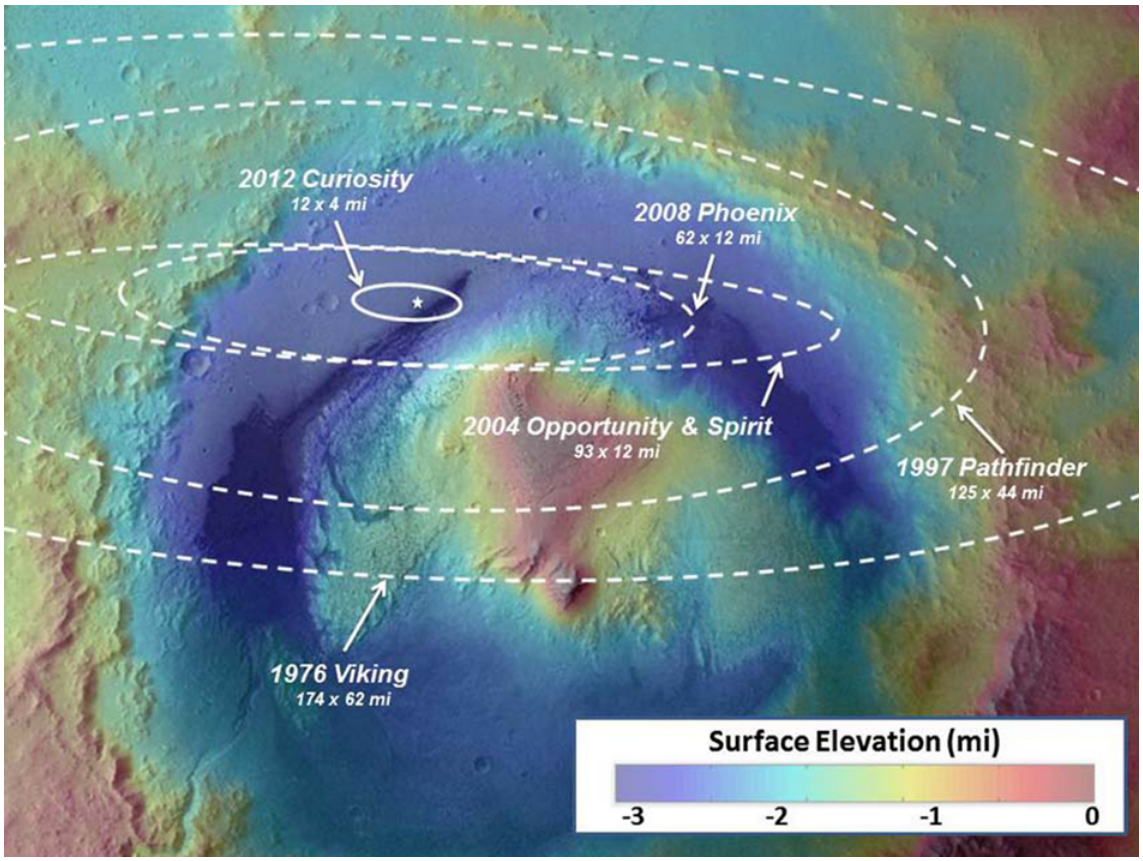

Figure 3.1: Historical perspective over NASA spacecrafts' landing accuracy on Mars. Image credit: NASA/JPL-Caltech/ESA

in Section 3.6 as conclusion of this study and as recommendations for a feasible solution to the problem.

3.1.1 Literature Review

An overview of terrain relative navigation approaches for lunar landing was published in Johnson and Montgomery (2008). The authors identify three Terrain Relative Navigation (TRN) functions: global position estimation, local position estimation and velocity estimation. All three can be achieved with active or passive sensors. The first begins during the coasting phase, while the spacecraft is flying at high altitude and initiating descent. At this point, only large scale surface features can be distinguished, therefore global positioning is possible by correlating with pre-acquired maps. I have noticed that this function is sometimes called absolute navigation. Later on, as the vehicle approaches the surface, the scene scale is such that no previous knowledge of the local terrain is available, thus the spacecraft can only

navigate relative to the extracted features until landing. Some publications refer to this function as relative navigation. The last function, velocity estimation, is critical for responding to the rapidly changing terrain. During the landing of the MERs in 2003, terrain relative velocity was the only information provided by the vision navigation system (Mourikis et al., 2009).

Methods for planetary landing generally start by looking for particular features on the surface that can be reliably identified and robustly tracked during motion. A common approach for pinpoint localization makes use of craters as landmarks. The abundance of craters of various scales and distribution over the Solar System bodies, makes them ideal for the purpose. A basic approach is found in Cheng and Ansar (2005), where craters are detected and matched in real time to a stored database for state estimation. Detection is based on edge detection and ellipse fitting. Position estimation is performed integrating prior knowledge of the global craters coordinates and is reportedly accurate to within 100 m. Other methods for crater detection apply different segmentation and classification methods (Maass et al., 2011) or are supported by machine learning approaches (Urbach and Stepinski, 2009), though present limited experimental results and are difficult to compare against each other.

Other approaches (Mourikis et al., 2007, 2009) favour smaller image features like points or corners. The authors show how cameras and IMU can be integrated with an extended Kalman filter in order to obtain precise and stable pose and position, as well as velocity within the strict requirements defined by future planetary missions. A ballistic rocket equipped with the instrumentation is used for experimental validation. The papers report errors at touchdown of 6.4 m in position and 0.16 m/s in velocity.

In Xiong et al. (2005) is described a method for computing depth maps from descent images using motion estimation and structure from motion techniques from the computer vision literature. The experimental results show that vision based sensors can also be used to map the landing region for future use. Additional work (Matthies et al., 2008, Johnson et al., 2008) confirms the potential of vision bases sensors for achieving safe, precise and autonomous planetary landing.

3.1.2 Terrain Relative Positioning

Precision landing entails reaching a predetermined destination within a smallest possible radius. This is achieved if the spacecraft is aware of its global position and can propagate this information during descent. To reach this goal, we essentially aim at enabling the vehicle to autonomously determine its position and velocity with respect to the terrain in real time.

Unlike atmospheric EDL, where the descent sequence is essentially vertical (parachute and rocket assisted), a lunar landing vehicle follows a ballistic trajectory, as illustrated in Figure 3.2. The sequence can be separated in two main phases: coast-

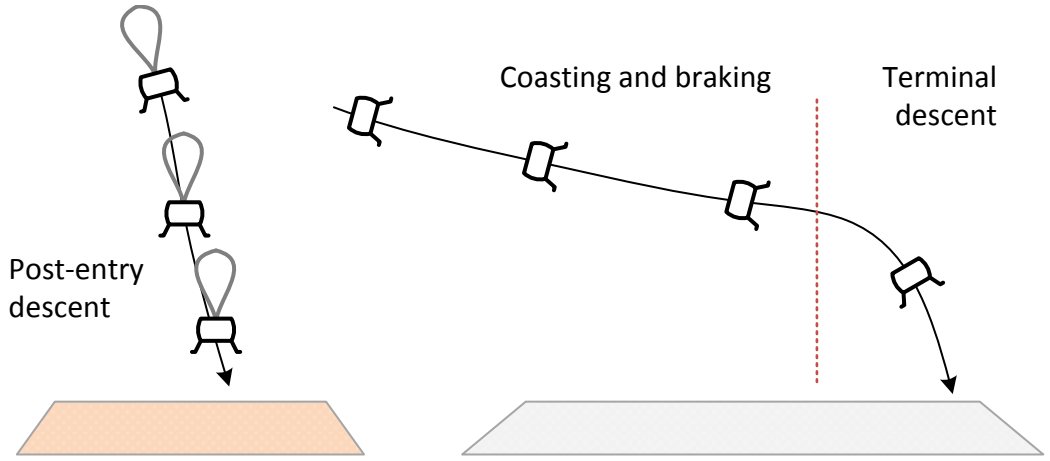

Figure 3.2: The landing trajectories are considerably different between a planet that has atmosphere (e.g. Mars) and one that does not, like the Moon.

ing and braking (CB), and terminal descent (TD). Due to powered braking and alignment manoeuvres, the initial state given by the orbital elements will lose precision soon after coasting begins. At this point, there are two pieces of information that the navigation system needs: its location and its velocity relative to ground. An algorithm for horizontal velocity estimation is described in Section 3.5. The localization problem will only be discussed theoretically.

Camera motion estimate using vision sensors is an ill-posed problem when targeting planar surfaces (and generally any co-planar features set), as a planetary terrain appears from the distance. This manifests as an ambiguity between the translation and rotation degrees of freedom, causing unstable and unreliable solutions. This is also known as the aperture problem. Yet, the integration of attitude determination sensors in the system can provide more constraints and ensure a correct solution, because it provides direct information about the camera rotations. Essentially two options are available: IMU and star cameras. Star cameras provide absolute measurements with arcsecond range accuracy and are ideal during all operations due to the lack of lunar atmosphere, as long as they are pointed away from the surface. IMUs provide relative but continuous measurements. Both sensors can be used individually or in conjunction for improved response. The advantage of a combined solution will be a much wider measurement bandwidth and robustness to "extreme" cases such as camera blinding, etc. An integrated system of the likes described herewith has been presented in Bjarnø (2010) and developed at DTU Space. Either solution can provide attitude information – typically in the form of a quaternion – so the data can be directly integrated in the process of motion estimation.

Global localization during descent can be solved by extracting recognizable ter-

rain features or landmarks and correlating them with pre-generated maps. Typical approaches in the literature identify craters in the scene and correlate them to orbital visual images or elevation maps. Nonetheless the Moon shows wide crater-less regions where such methods would fail. Therefore a more generalized approach based on edges or point features should be favoured.

3.2 CONSTRAINTS

Aimed specifically at optical sensors, this section examines the constraints affecting the system relevant to a landing scenario. As seen from the sensor's point of view, looking out to the world, a simple classification of the external constraints can be the following:

- Optical
- Spatial
- Morphological

While this approach is clearer in drawing attention to the sources, the boundaries between the three classes are, in fact, not as sharp. The classes are interconnected, for example morphological and spatial constraints can influence the visibility of certain features, just like the illumination source can show or hide the morphology of the terrain. In order to maintain a structured discussion, the classification will be maintained, though the commonalities will be treated together.

Optical constraints arise from the nature of the sensor of collecting and measuring light. Features visibility is dependant on two factors: the amount of light shining on them and the surface reflectance properties. In turn, the scene lighting depends on the sources of illumination and on the temporal state of operation. The primary light source is the Sun, therefore its local orientation relative to the observed surface and the observer, has predominant effects on changes in the scene's appearance. Orbital dynamics of the celestial body and the spacecraft itself also influence features visibility while transitioning between the day and night sides. In addition, a combination of terrain morphology and atmospheric effects (dust storms or total lack of atmosphere, depending on the scenario) produce changes in shadows projection and contrast dynamics. On a lunar surface, the sharp contrast between the lit regions and shadowed basins effectively renders invisible portions of the terrain. This effect can be actively used as information source, as described in Section 3.4. The study of light is part of the science called photometry, discussed further in Section 3.3.

The choice of a target landing and operation region normally takes into account the terrain morphology and the spacecraft's dimensions. Accurate planning is required in order to identify a location with sufficient margins for a safe landing,

accounting for the precision of the landing system and the availability of fuel for eventual repositioning. On a larger scale, the region is defined by the beginning of the descent phase and is projected on the surface drawing an elliptic area. Depending on the mission objective, equatorial or polar regions may be of interest. The many geological differences between these regions and furthermore between the near and far side of the Moon, bring additional constraints to the available safe zones.

The high orbital speeds and changing dynamics during descend and landing require systems that are not only precise, but highly responsive. Time is another major constraint of navigation stressing the sensor's internal architecture. Just like energy, processing power is also limited in availability and the algorithms have to be light weight in order to keep up with the rapidly changing scene.

Finally, there are several other sensor intrinsic parameters that constrain the performance of the system. Field of view, depth of field, sensitivity and exposure are some of the parameters to tune, in order to optimize the instrument's capability of extrapolating usable information from the scene. Section 3.6 outlines in more detail the selection of such parameters. In particular the sensor's response time, measured from the start of integration to the completion of the image data processing, defines the instrument's ability to timely react to the changing scene and operate as close as possible to real time.

3.3 SCENE ANALYSIS

A foregoing study of the optical and morphological properties of the observed landscape grants better insight for the sensor optimization, towards improved performance and robustness. The risk of unforeseen effects is also greatly diminished. This section is dedicated to the analysis of the scene surrounding the spacecraft during a Moon landing.

3.3.1 Landscape

A rich collection of lunar surface images has been acquired along the years by various orbiters, since the American and Soviet lunar programs of the 1960s. The more recent Clementine (1994) spacecraft was equipped with visual and NIR band imagers and has long been used as reference for studying the lunar morphology and reflectance properties. Lately though, spacecrafts like JAXA's Kaguya (SELENE, 2007) and NASA's LRO (Lunar Reconnaissance Orbiter, 2009) have expanded upon it and provided global scale high resolution shots. Some suggestive forward-pointing shots taken by Kaguya are shown in Figure 3.3. The pictures were taken from 100 km altitude and about 20 degrees downward pitch. It is clear from the images how, despite a predominantly cratered landscape, the surface also exhibits vast flat regions (the maria) and other mountainous complexes of different scales. Further-

more, the uniform gray texture is, at times, spotted with bright patches or darker regions. Figure 3.4 combines different LRO close-ups of the many surface features distributed along the lunar landscape. Craters manifest in all sorts of regular and irregular shapes, clustered or overlapping. Volcanic eruptions have also scarred the lunar surface in the past and have left extensive ridges, faults and rilles. On a smaller scale, the almost constant presence of scattered rocks and boulders, has been observed in all the past surface missions, of the likes we can see in the Apollo 17 shot of Figure 3.5.

Plescia (2008) provides a summary about the currently known and unknown properties of the Lunar surface, based on data from Ranger, Surveyor, Lunar Orbiter, Apollo, Luna and Lunokhod. The highlands have a reported rougher topology, as compared to the maria, because of numerous large craters and are therefore considered more hazardous for landing and surface operations. In general, fresh craters are known to be the deepest, thus their edges will be steeper and pose higher landing risks and traversability constraints. Rock distribution and abundance are regulated by fresh impact craters. Data from the relatively flat and smooth visited sites show a distribution of large rocks ($\geq$ 30 cm) up to 10–30 units per 100 m^2. Boulders were not observed in the available sources and have not been categorized. This statistic is based upon limited observations and should not be considered as representative of the whole scene. A focused analysis is required during mission planning, after the target region has been defined.

3.3.2 Radiometric Study

The dominating - and in fact the only active one at this scale - illumination source within the Solar System is the Sun. The electromagnetic radiation emitted by it, covers much of the spectrum, though its distribution is not uniform. Through observations and models, scientists have revealed that this distribution can be approximated by Planck's law, which in general describes the temperature dependent black body radiation. A formulation of this law, describing spectral radiance traveling at a point in terms of the wavelength λ, is shown in Formula 3.1 (where k_B is the Boltzmann constant, h is the Planck constant, and c is the speed of light).

$$B_\lambda(T) = \frac{2hc^2}{\lambda^5} \frac{1}{e^{\frac{hc}{\lambda k_B T}} - 1} \tag{3.1}$$

Figure 3.6 illustrates the relation between the measured and the approximated solar spectral irradiance at a distance of 1 AU from the Sun and a surface temperature of 5778 K. This quantity is a measure of power arriving at a surface per unit of wavelength. The total irradiance can be calculated by integrating this function over the whole spectrum. In Earth's proximity, this results in about 1361 W/m^2 (varying with the location in orbit). For the Moon, we can assume that the irradiance will

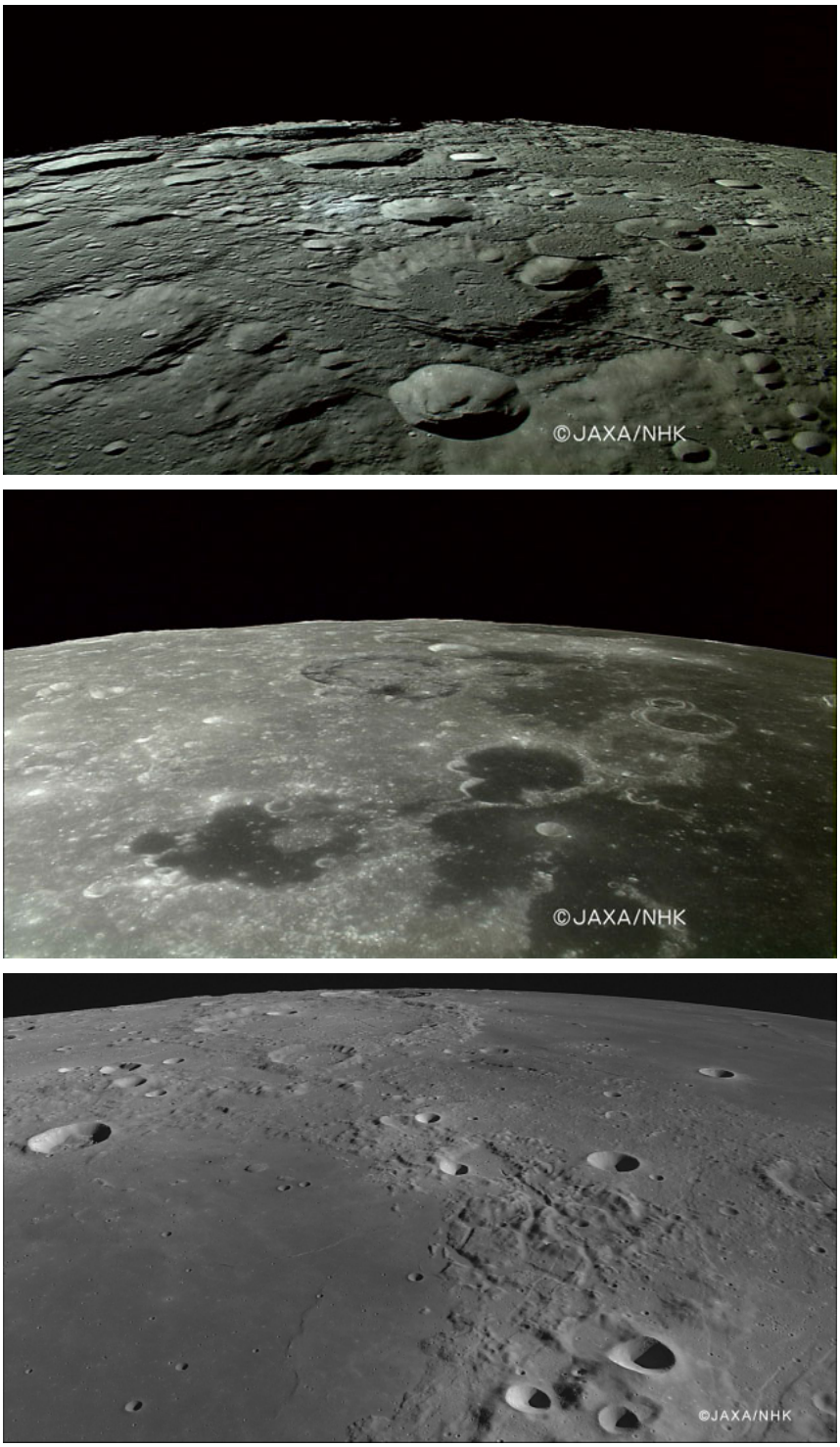

Figure 3.3: Orbital shots of Earth's Moon. Picture Source: Kaguya (Selene) spacecraft, HDTV images, JAXA.

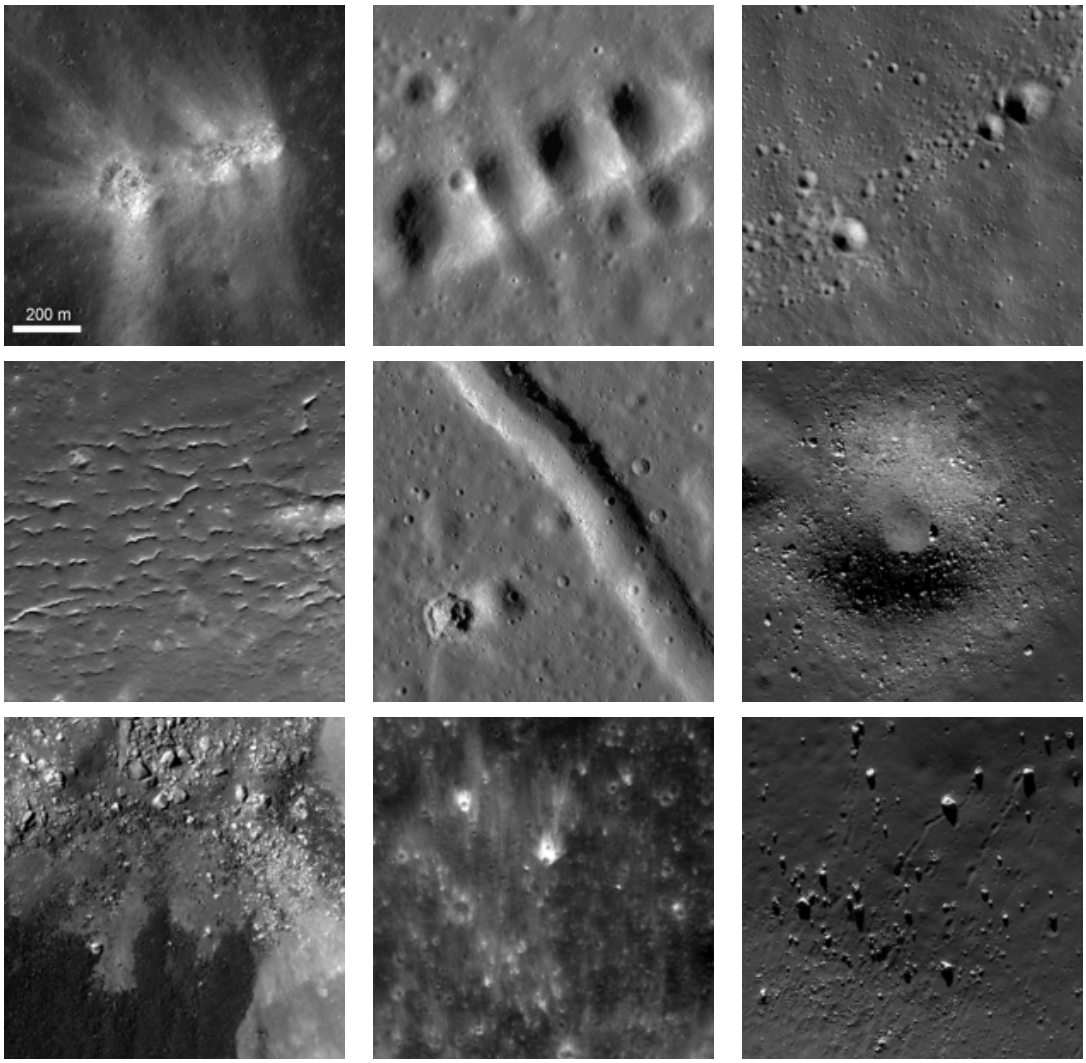

Figure 3.4: Orbital shots of Earth's Moon. Picture Source: LRO spacecraft, LROC instrument, NASA.

average along orbit to about the same value. In our case we will be interested only in the bandwidth to which the camera system is sensitive to, which is affected by both optics filters and image sensor.

As described in Section 2.1, knowledge of the surface reflectance properties is required in order to acquire an estimate of the scene radiance, which then enables the derivation of the irradiance on the image sensor. Various studies have covered the modelling of the lunar surface reflectance, in the attempt to determine an accurate BRDF. Minnaert (1941) proposed a model that approximates reasonably well the lunar surface as a function of $cos\theta_i/cos\theta_e$ and adjusted it to obey Helmholtz's

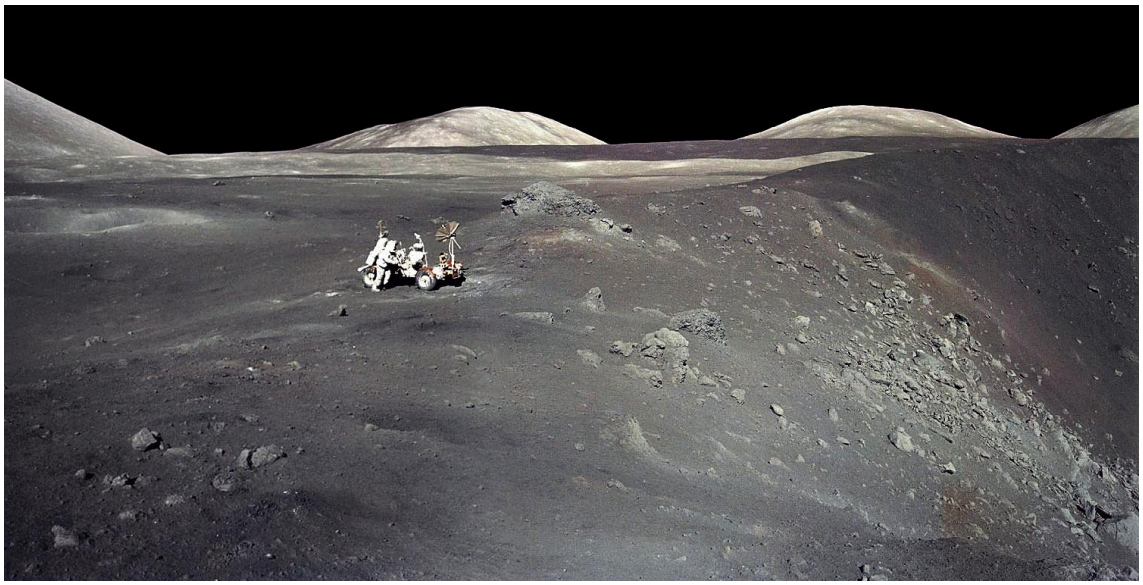

Figure 3.5: Lunar surface sightseeing. Picture Source: Apollo 17, NASA.

reciprocity principle[1]. The lunar-Lambert function is another model commonly applied to various planetary surfaces studies and also good for modelling the Moon. More extensive models have been derived both analytically end empirically. McEwen (1991) published a study where the Minnaert and lunar-Lambert functions are fit to the empirically constructed Hapke equations. Both show consisting results when applied to the photoclinometry[2] problem. Hapke equations are reported to be "more easily related to physical properties of planetary surface materials", though have many parameters and result heavier to compute. The paper reveals that the simpler photometric functions have "insignificant deviations" from the more complex Hapke and are therefore recommended, particularly when computation efficiency is desired. Given the considerations above, this photometric study uses the Minnaert function in the following representation.

$$L_r = E_0 \frac{k+1}{2\pi} cos^{k-1}\theta_e \, cos^k\theta_i \tag{3.2}$$

The formula is valid provided that $-\pi/2 \leq \theta_i \leq \pi/2$ and for $k < 1$. Knowing the incoming irradiance E_0, one can estimate the lunar radiance for varying angles of incidence θ_i and observation θ_e.

[1]The principle states that reflectance does not change if the incident and emitted angles are interchanged.

[2]The measurement of topography from photometric shading, also known as *shape from shading* in computer vision.

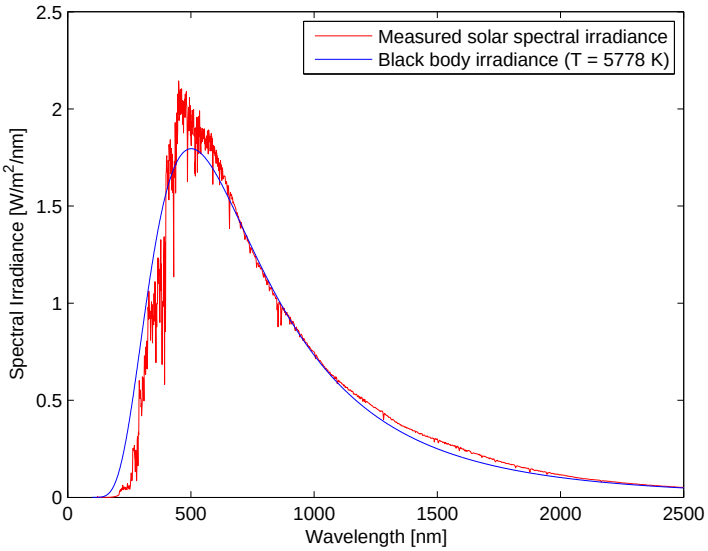

Figure 3.6: The solar spectral irradiance can be closely approximated by Planck's law. Irradiance data source: rredc.nrel.gov/solar/spectra/am0/.

Next, it is possible to apply the thin lens aperture equation (Forsyth and Ponce, 2003) to calculate the irradiance E_p on an image sensor patch.

$$E_p = L_r \frac{\pi}{4} \left(\frac{d}{f}\right)^2 cos^4\alpha \tag{3.3}$$

where d and f are the lens aperture and focal length and α the incoming ray angle w.r.t. the lens boresight. Photons, as we know from quantum physics, transport quantized amounts of energy. The energy of a photon is given by $E_{ph} = hc/\lambda$ and is a function of the wavelength. Since the incoming power per unit area is now known, the photon flux Φ can be calculated by dividing the irradiance by E_{ph}.

$$\Phi = \frac{E_p}{E_{ph}} \tag{3.4}$$

This quantity is measured in $[s^{-1}m^{-2}]$. The number of electrons released on the image sensor by the photoelectric effect, depends on the photon flux reaching the sensor and is directly proportional to the quantum efficiency q of the chip and the integration (or exposure) time t. An additional factor, the cell surface area A, is added for quantifying the result at each individual image cell (or pixel).

$$N_{e^-} = \Phi\, A\, t\, q \tag{3.5}$$

Finally, the resulting pixel value can be calculated by relating N_{e^-} to the sensor's full well capacity. For a gray scale image sensor, this assumes integrating indiscriminately over the whole optics bandpass spectrum.

The model is not complete without the inclusion of the noise effects occurring during the image formation process. Following the account of Section 2.2, the sensor noise model thereby defined can be applied to this case. This can be combined with the signal previously calculated and used to give a quantitative figure of the measurement quality. Recalling Equation 2.3, the resulting SNR is defined as

$$SNR = \frac{N_{e^-}}{\sqrt{N_{e^-} + Dt + N_r^2}} \tag{3.6}$$

Where all factors at the denominator represent electrons released by noise sources. Due to the absence of atmosphere, there are no effects of scattering or absorption occurring on the Moon. If necessary, the model can be expanded with the inclusion of quantization error and other effects that have been neglected. While longer integration time results in higher SNR, the temporal and dynamic constraints of the case fix an upper limit to which the design should aim at.

The model described here has been personally developed to assist in the design of the vision sensor and the optimization of its many parameters. Section 3.6 applies the outcome of this study to the landing case, and provides an example using realistic scene and instrumentation parameters.

3.3.3 Considerations

Static and dynamic illumination conditions on all planetary surfaces are determined by orbital mechanics. Although the scope of this investigation does not cover mission planning, the understanding of such effects is still very relevant. Scene brightness depends on surface properties, as we have seen in the previous section, as well as on lighting geometry. Intuitively no light falls on the dark side of a body, thus the scene brightness is insufficient for a non-augmented sensor. On the opposite side, variations in the angle of incidence of light may change considerably the aspect of terrain features, as shown in Figure 3.7. This will introduce ambiguities and may require more generalized algorithms for large scale feature detection. In general it can also be concluded that for small phase angles, the reliability of optical hazard detection would degrade considerably, as features of all sizes would blend in with the surface. Further considerations are made in Section 3.4.

The Moon synodic period is about 29.5 days, compared to the about 27 days orbital period. The lunar rotation period is the same as its orbital period. The daytime duration is long enough so that lighting variations during landing are negligible. Nonetheless, the polar regions represent a boundary case as their location exposes them to consistent low elevation lighting, resulting in a predominantly shad-

owed landscape. High scientific interest in these locations makes them for a likely destination and might therefore have to be studied more carefully.

Calculating the orbital velocity can be useful to estimate the image optical flow and thus determine the optimal integration time. This velocity marks the upper limit, as the spacecraft will gradually slow down during coasting and braking. The state of equilibrium maintained by an object in orbit can be described by the balance of centrifugal and gravitational forces.

$$m\frac{v^2}{r} = G\frac{m\,M}{r^2} \tag{3.7}$$

Solving for the tangential velocity v gives

$$v = \sqrt{\frac{G\,M}{R+h}} \tag{3.8}$$

where M and R are the largest body mass and radius respectively and h the spacecraft altitude. For a Moon orbit at 100 km of altitude, the tangential orbital velocity will be $v_o \approx 1630$ m/s. The horizontal velocity relative to ground is given by

$$v_g = v_o\,\frac{R_M}{R_M + h} = 1541 m/s \tag{3.9}$$

The image plane velocity is highest when the camera points towards nadir. Knowing the focal length f and using a basic pinhole projection model, the worst case image plane velocity v_i is found as

$$v_i = v_g\,\frac{f}{h} \tag{3.10}$$

This analysis continues in Section 3.6, where case sensor parameters are discussed.

3.4 HAZARD DETECTION

In the final stage of landing – known as terminal descent (TD) – somewhere between one hundred meters of altitude[1] and touchdown, many of the finer morphological properties of the terrain become detectable: rocks, boulders, cliffs and cracks. The combined effect of direct lighting and absence of scattered light can facilitate the detection of hazards as any projected shadow is evidence of abrupt elevation changes in the vicinity. The scene analysis suggests that a shadow detecting algorithm, supported by appropriate expedients, would make it for a simple and effective method

[1]Estimate acquired by analysing the recording and voiced telemetry of the Apollo 11 landing.

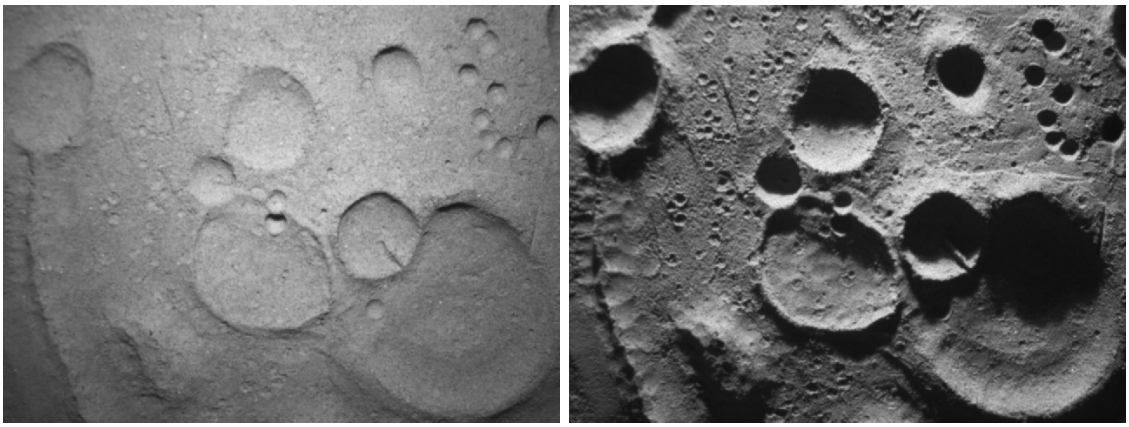

Figure 3.7: The same scene appears considerably different with changing light incidence angles. (left) Sun at 80° elevation. (right) Sun at 20° elevation. Simulated lunar terrain.

for indirect detection of hazards given favourable lighting conditions. These conditions include Sun elevation angles within a certain range, with a lower boundary defined by visibility requirements and a higher boundary set by the need for projected shadows. The ideal range is to be investigated further, possibly by laboratory tests. Nonetheless, it is advisable to schedule the descent in this interval.

This section introduces the Monocular Safe Region Detection algorithm (MOSARD) to address the hazard detection problem during TD by means of a single camera sensor. Shadowed areas are deemed unsafe a priori, given the impossibility to determine surface properties. Conversely, uniform texture areas of the observed surface are considered free from hazards. The algorithm includes computer vision techniques of segmentation and morphology in order to identify these regions while at the same time determining size and density of hazards in the field of view. The process is outlined in Figure 3.8. The regions are classified as: safe region (SR) or hazard region (HR).

Noise and finer details of the scene are filtered out in the first step. In order to preserve edges, a lean median filter is preferred to the standard Gaussian filter. A small stencil size can be used to prevent loss of detail and maintain good performance.

Double thresholding is applied to isolate two HR of interest: shadows and highlights. The latter are included in the process because they have been observed at locations of high slopes, often around craters edges. A fixed threshold is not advised for live operations, as the expected temporal variations in scene brightness (due to noise or adaptive gain control) make it hard to define a universal boundary. Two alternative methods have been investigated for a more robust determination of the threshold: adaptive and Otsu's thresholding. Otsu's method is based on his-

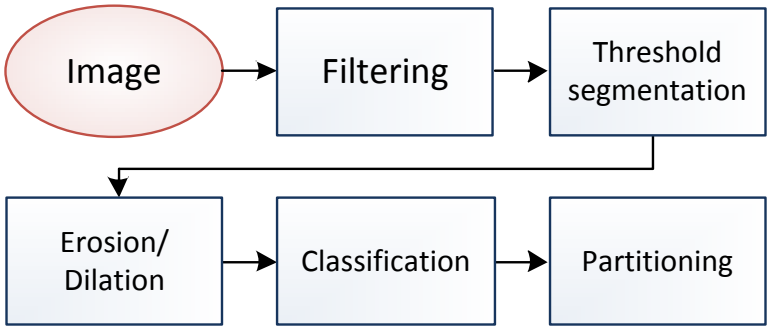

Figure 3.8: MOSARD algorithm process.

togram analysis and works best for images with bi-modal histograms. The adaptive method finds a local threshold based on a statistical analysis of the intensity values of the local neighbourhood of each pixel. This threshold can be calculated in various ways (e.g. median or mean pixel value) and is different for each pixel. The adaptive method is not parameter free as it requires the definition of two parameters on which it will base the local threshold (window size and threshold offset), but is robust to changes in image brightness and shading. An example of the application of these methods is shown in Figure 3.9. We will concentrating on the result of the standard against the adaptive method, which clearly give the best results. At a threshold value $t = 50$, the first appears much too sensitive to darker shades on the right side of the image, while missing the rock clusters on the left side altogether. The adaptive method (box size $b = 101$, offset $C = 45$) instead has a more consistent hit rate and does not respond to smoothly varying shades.

Segmentation between safe and hazardous regions is enhanced by multiple erosion and dilation morphology operations. Erosion is used to suppress the smallest and negligible areas, while dilation is applied to restore the original size of the objects. Another reason to dilate is to include the actual shadow projecting object in the HR. The object (a rock or a cliff) will be well lit and harder to discern from the rest of the terrain, but located in the direct surrounding of the shadowed region.

Estimating the size of each hazard region and their distribution would provide more quantitative information to the GNC system, helping to reduce propellant consumption before reaching the safest region. The HR are classified as a function of their size and closeness to additional hazard regions. A three levels metric is hereby proposed for classification, with total risk growing on a scale from HR1 to HR3, as defined in Table 3.1. The classification is performed by segmenting the image in rectangular areas and assigning an HRx rating to each one according to its content. This partitioning process can be implemented as a uniform spacing grid

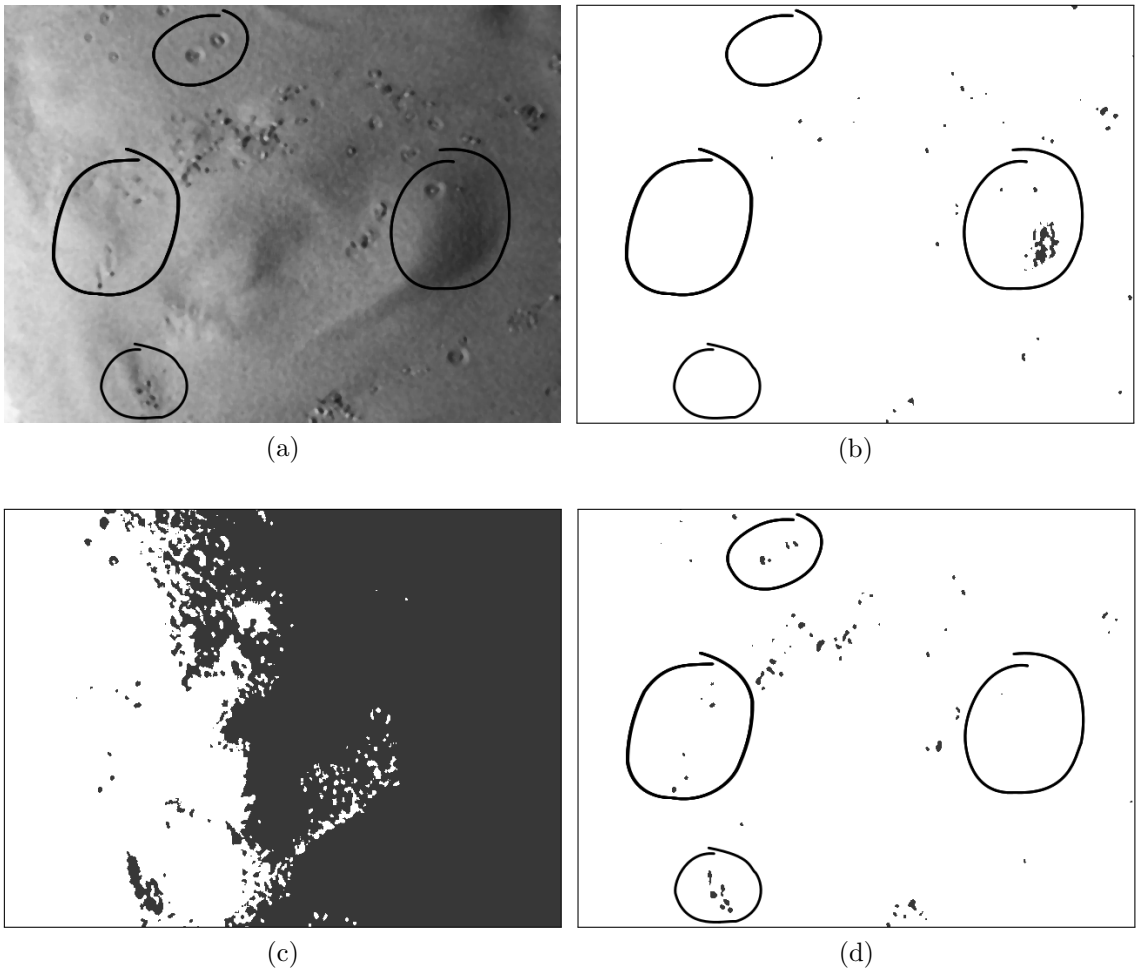

Figure 3.9: Comparison of different thresholding methods applied on a lunar analogue terrain scene. (a) Original filtered image. (b) Standard thresholding, $t = 50$. (c) Otsu's method. (d) Adaptive thresholding.

or as a k-d tree. The trade-off is between the faster uniform spacing and the more accurate k-d tree.

Classifying a region by size has a physical meaning only if the algorithm has access to real time altimeter data, otherwise the classification is only made in pixel dimensions. If altitude information is known, an estimate of the size on ground can be calculated using the well known perspective projection relation below.

$$\frac{w_{im}}{f} = \frac{w}{h} \tag{3.11}$$

With w_{im} the region width on the image plane, f the focal length, w the region

	Classification	Definition
SR	Smooth region	Safe landing zone
HR1	Small highlight region	Potential slope
HR2	Medium highlight region	Potential wide slope
	Small shadowed region	Presence of small hazard around a non illuminated region
HR3	Medium to large shadowed region	Extensive high risk region
	Large highlight region	Extensive high risk region

Table 3.1: Hazard region risk classification scale.

physical width and h the spacecraft altitude. The result is an approximation, since the camera off-nadir angle has not been corrected for and the observed surface may not be parallel to the image plane.

3.4.1 Experimental Implementation

MOSARD has been implemented in C/C++ code in Visual Studio environment and complemented by algorithms from the open source OpenCV library for filtering, segmentation and morphology. The tool at work is shown in Figure 3.10.

Integration of the calibration and validation laboratory described in Chapter 6 has been completed alongside this work. Various sequences of images from a camera flying over simulated lunar terrains (discussed in Section 6.6) were acquired in the laboratory, covering separate phases of planetary landing. Multiple terminal descent (TD) sequences were used to test MOSARD, with a terrain scale 1:100 and an equivalent initial altitude of 80 m. Figures 3.11 and 3.12 present static results with different parameters for filtering and thresholding. It can be noted how a growing median filter stencil causes progressive loss of detail in the image and reduced response to hazards. For a fixed filter size and a 100 px box size, the algorithm response to image features is increased when the threshold offset (C) is reduced. Figure 3.12c is an example of a balanced choice of parameters. Finally, Figure 3.17 shows the effect of applying a region partitioning grid. The grid segments the field of view and assigns an HRx rating to each region according to its content. The result shown in this figure has been created manually for display as the partitioning is not implemented.

Two TD sequences were recorded in the laboratory: a pure downwards motion and a sidewards sweep. MOSARD was run continuously (offline) on each image for both sequences. In Figures 3.13 and 3.15 are shown the final capture of each sequence and a histogram distribution of the detected shadow hazards areas. Figures 3.14 and 3.16 outline the hazard statistics tracked along the sequence: number of

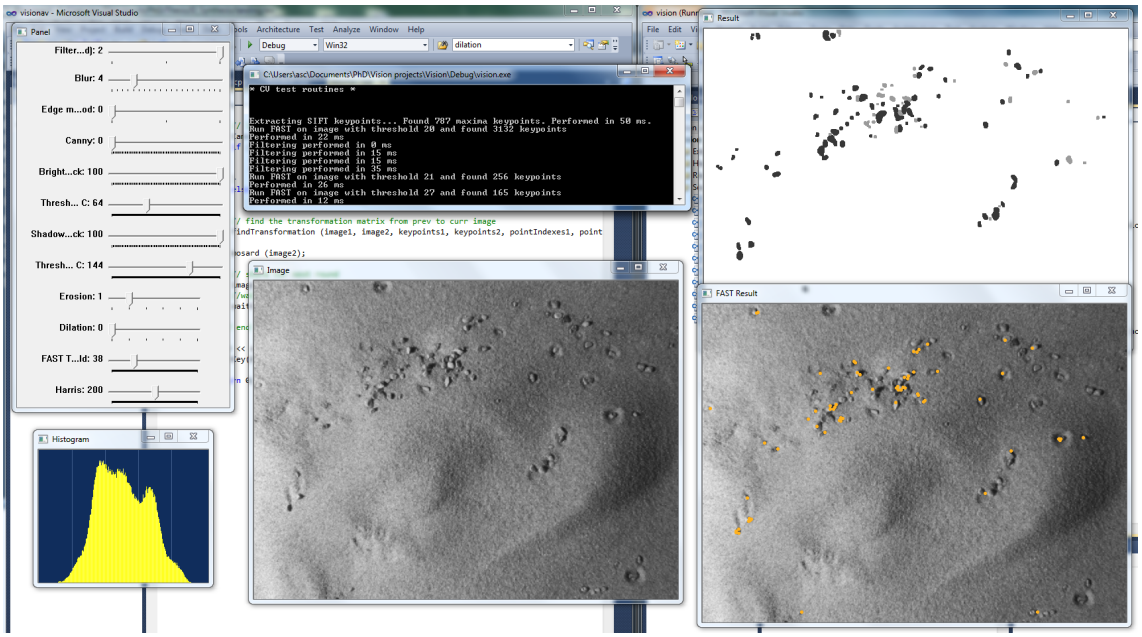

Figure 3.10: Algorithms testing setup with live tweaking of parameters.

hazards detected, mean area and largest area. The statistics were determined by using standard image analysis segmentation techniques. As expected, the area of the detected hazards increases as we approach the surface (Figure 3.14), as well as their number. This last result is important, as it shows how the algorithm is able to constantly reveal new hazards as they become more evident. In the sidewards sequence, the camera horizontal motion covers a constantly changing terrain. Although the mean area increases slightly towards the end (Figure 3.16), we can observe a general decrease in hazards detected, suggesting a safer region for landing.

3.4.2 Considerations

The responsiveness of the algorithm to slopes (e.g. around smooth hills) should be investigated further, unless the targeted region is known in advance to be relative flat. More advanced methods for shape recovery, such as shape from shading, might improve the accuracy of hazard detection, however those approaches are much more demanding in terms of computation resources thus not suitable for real time.

Automatic handling of the operating parameters at each step should also be implemented, in order to have a fully autonomous algorithm capable of adapting to real world changing conditions. Testing under different lighting conditions would also be useful to this end.

Hazards information acquired by the sensor is required by the navigation system

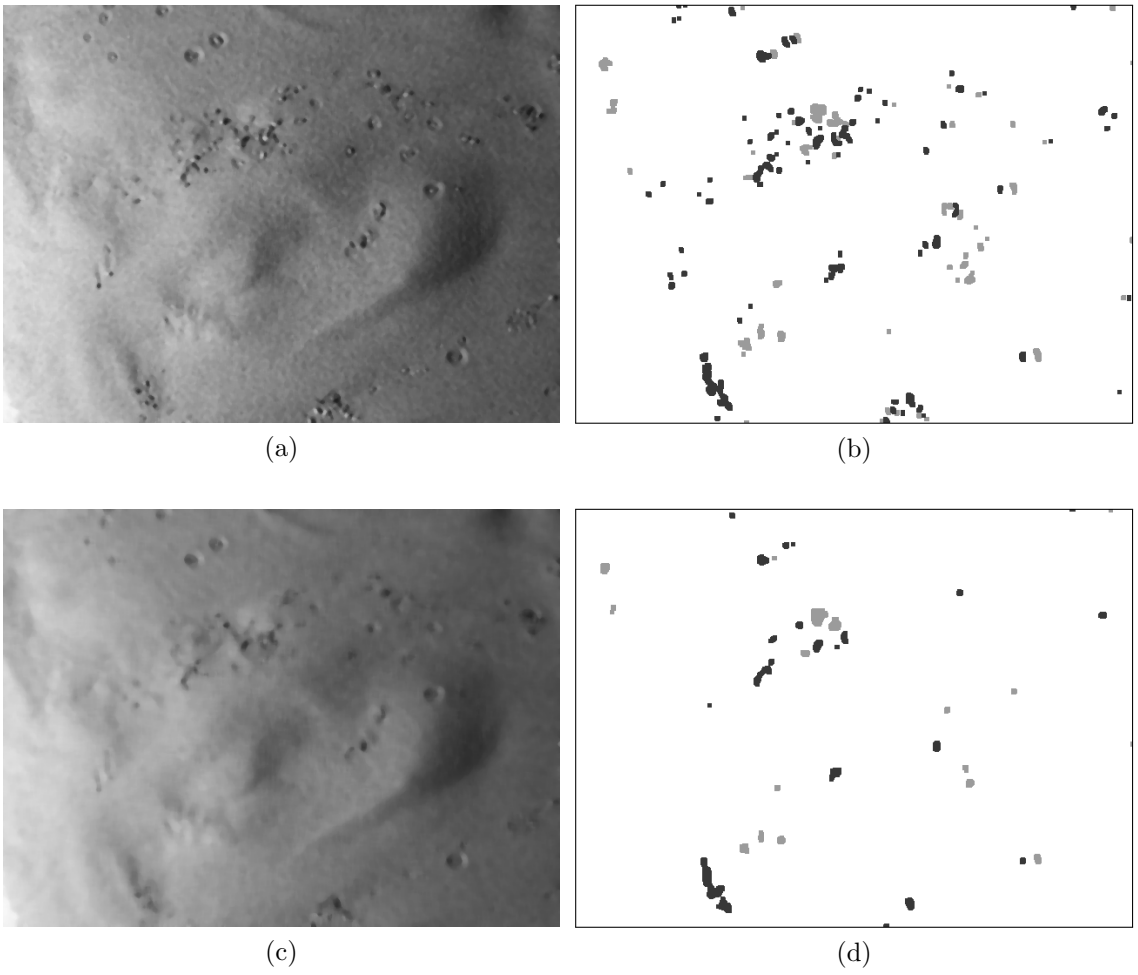

(a) (b)

(c) (d)

Figure 3.11: MOSARD results for growing median filter stencil size. (a) Filter size: 5. (b) Result for filter size 5. (c) Filter size: 9. (d) Result for filter size 9.

in order to calculate the appropriate alignment manoeuvres in preparation for landing. To this purpose, simple target size information is not sufficient. Line of sight for each partitioning tile can be calculated with simple trigonometry and translated to RA/DEC or quaternion. Furthermore, altimeter and inertial data can be integrated to account for the off-nadir angle and distance from ground to determine the relative location of each safe region w.r.t. the camera.

3.5 VELOCITY ESTIMATION

Determining the spacecraft velocity in real time during the powered descent provides vital information to the spacecraft control system. Any necessary correction

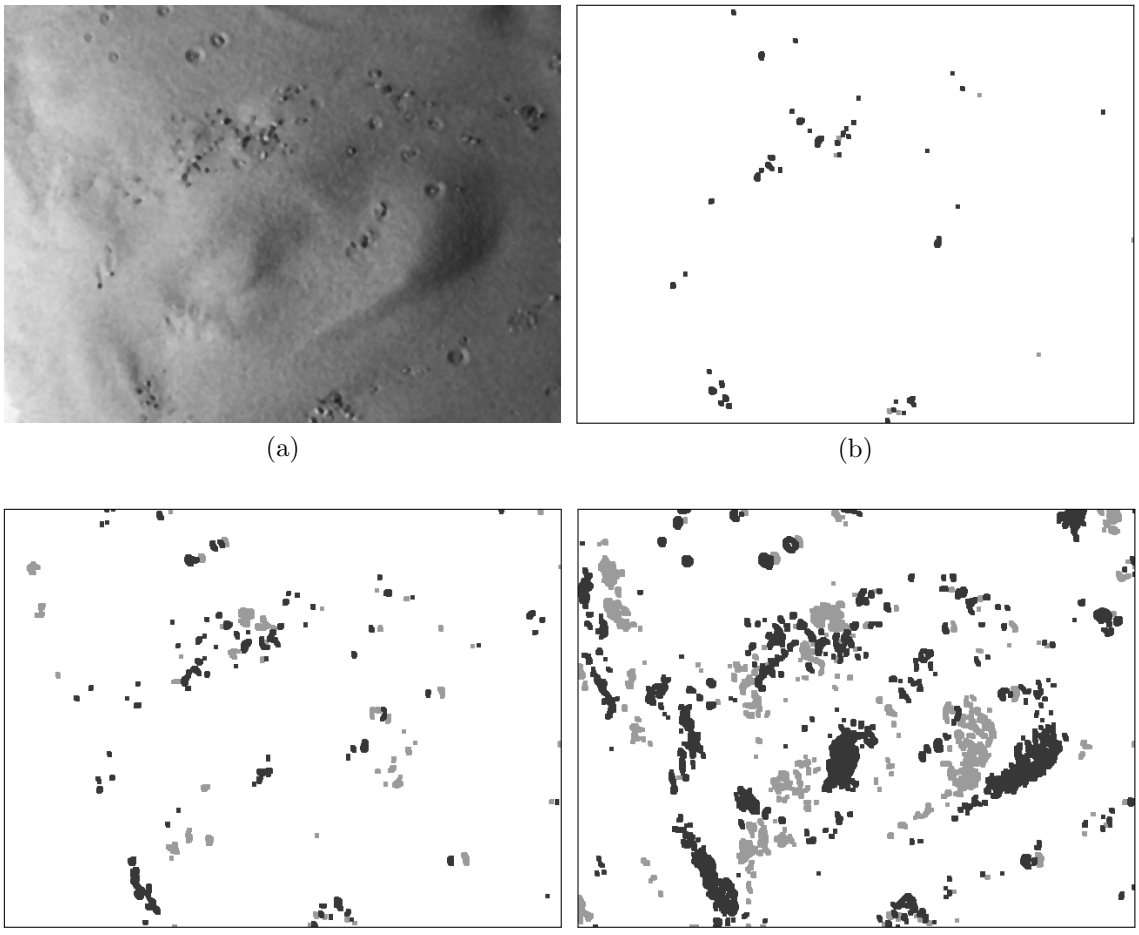

(a) (b)

(c) (d)

Figure 3.12: MOSARD results for different thresholding parameters and fixed window size. (a) Original image. (b) C offsets: 40 (highlights), 50 (shadows). (c) C offsets: 23 (highlights), 33 (shadows). (d) C offsets: 15 (highlights), 15 (shadows).

to the thrusters output should be applied if the parameters are not within the specifications. The velocity can also be integrated in the relative navigation system as input to the propagator. The terrain-relative velocity vector can be broken in two components: vertical and horizontal. While the vertical component can be easily determined by differentiating successive altimeter readings, the horizontal component requires more processing and a more detailed sample of the surroundings. An imaging sensor directed at the surface can provide enough information to calculate this parameter. This section discusses the problem and proposes a simple solution dubbed Monocular Horizontal Velocity Estimation (MOHVE). The procedure de-

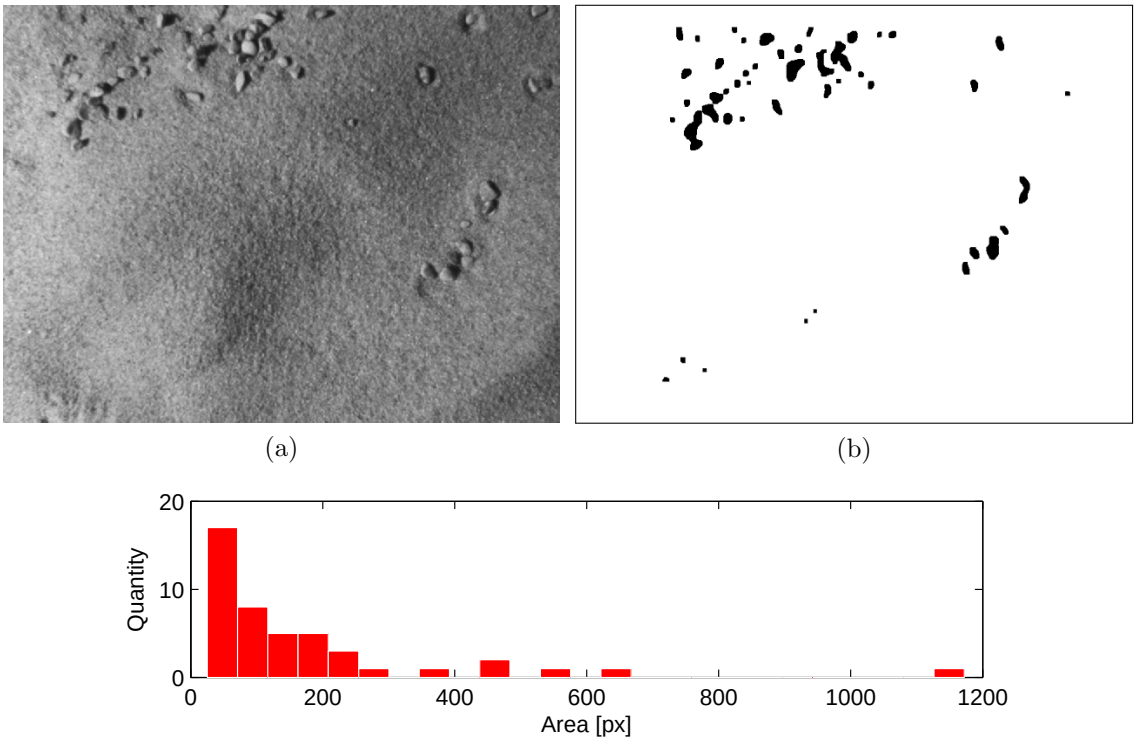

Figure 3.13: Final snapshot of the downwards TD sequence and distribution of the detected hazards in terms of image area.

scribed below assumes that the correspondence problem has already been solved and that acquisition and tracking of feature points are performed before they vanish from sight.

The absence of atmospheric effects and the limited fuel available, define specific boundary conditions to the lander's degrees of freedom. Forward motion and vertical descent are the only notable translations occurring as effect of the ballistic trajectory. Rotations are limited to pitching corrections to compensate for the combined effect of the gravity and velocity vectors. The method is based on tracking multiple feature points between the previous and the current image and estimating the horizontal velocity based on the observed displacement.

The large scale difference between the spacecraft altitude and local terrain elevation changes during most of the powered braking sequence allows us to consider the observed surface approximately planar.

Differential attitude from IMU or star camera can be integrated to correct each feature point for the relative rotations between the successive images. Also, as the camera pointing may differ from the nadir direction, appropriate angle corrections must be included in the distances calculations, based on attitude data. Finally, the

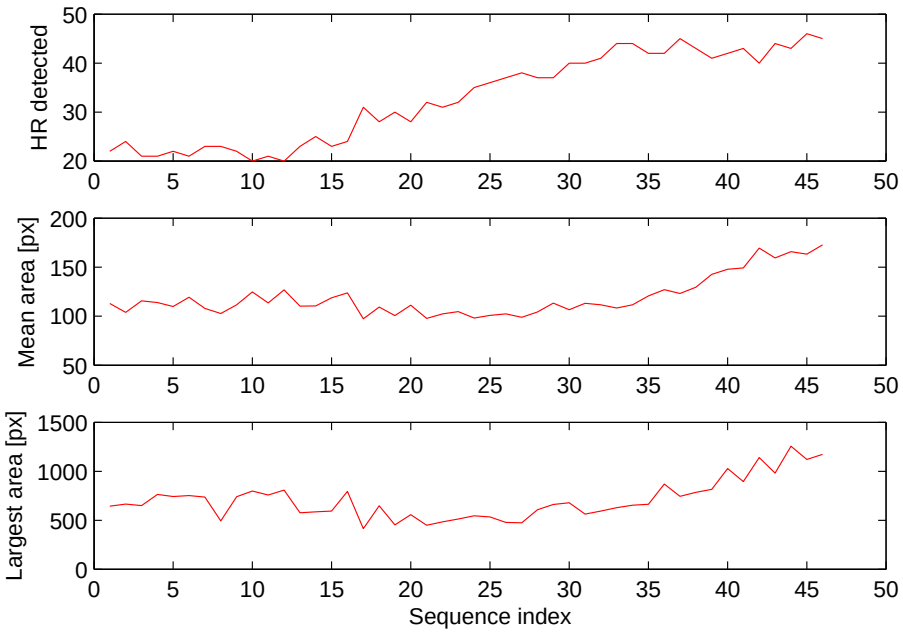

Figure 3.14: Statistics of the downwards TD sequence.

problem can be tackled focusing exclusively on translations.

Altitude data from any type of altimeter comes in handy in the determination of the correct scale of translation, which would otherwise be ambiguous if only image plane information was available. The drawing in Figure 3.18 represents the lander motion reduced to a planar translation. The spacecraft observes a point at time t_0 and t_1 while advancing a distance d and descending from altitude h_0 to h_1. According to this geometry and with the assumptions discussed above, the horizontal velocity can be found as

$$v = \frac{d}{t} = \frac{l_0 - l_1}{t} \tag{3.12}$$

where

$$\begin{aligned} l_i &= h_i \, tan(\alpha_i) \\ \alpha_i &= \gamma_i + atan\left(\tfrac{y_i}{f}\right) \end{aligned} \tag{3.13}$$

with γ the measured off-nadir pitch angle, f the focal length, y_i the rotation-corrected point coordinate on the sensor plane (in the direction of motion).

The error induced by assuming a planar terrain can be reduced by averaging the results from multiple features distributed uniformly over the overlapping image

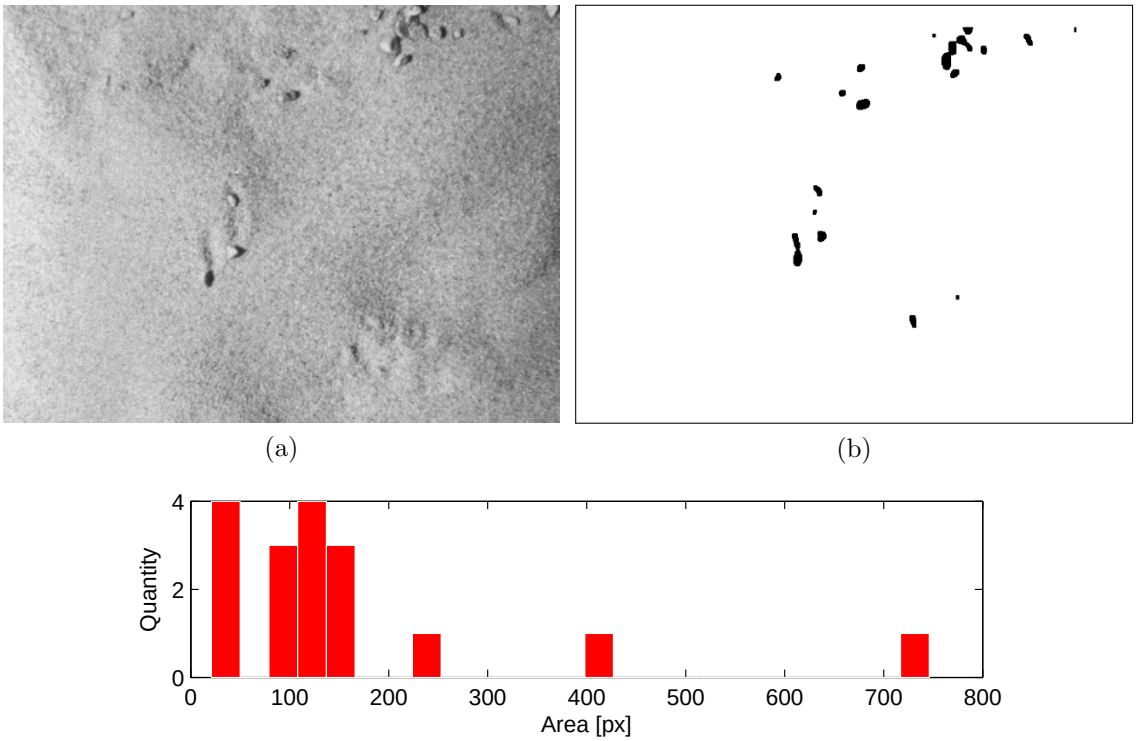

Figure 3.15: Final snapshot of the sidewards TD sequence and distribution of the detected hazards in terms of image area.

region. On the other hand, the effects of wrong matches can only be reduced either by picking the median value or, more robustly, with a RANSAC filtering method.

3.5.1 Experimental Implementation

MOHVE has been implemented in C/C++ code in Visual Studio environment and complemented by algorithms from the open source OpenCV library for feature extraction and tracking. The method was tested on the recorded large scale terrain sequences described in Section 6.6. The sequences (tagged SEQ-*xx*, where *xx* is the progressive number) were run at constant horizontal velocity, fixed altitude and nadir pointing. The test parameters are listed in Table 3.2.

For conciseness, only results from sequence SEQ-06 will be reported here. Since SEQ-06 was recorded at 1.2 fps, MOHVE was run at 5 s intervals (6 image step) in order to have a reasonable track length, while limiting the risk of features loss. The travelled distance, given this interval and the fixed velocity, is then 25×10^{-3} m.

Results from experimental tests for the sequence SEQ-06 are collected in Figures 3.19 and 3.20. At the top are shown a sample of tracking lines along the sequence

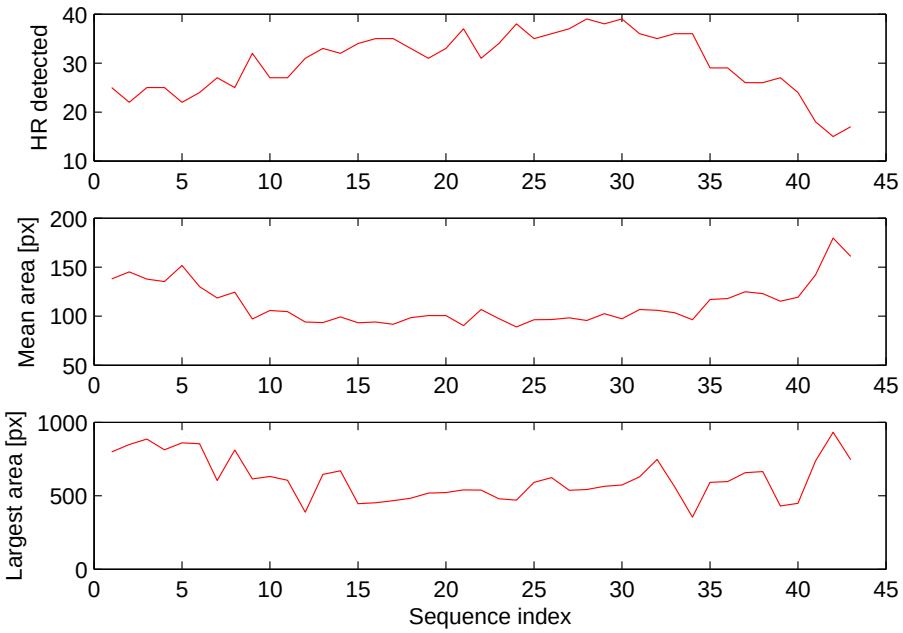

Figure 3.16: Statistics of the sidewards TD sequence.

Altitude [m]	0.8
Velocity [m/s]	5×10^{-3}
Pitch [deg]	-90 (nadir)
Capture rate [fps]	1.2

Table 3.2: Test parameters for the large scale sequences.

and the relative travel distance estimate distribution. The plots below show median and mean values closely following the true value (blue dashed line). Peaks in the mean standard deviation can be occasionally observed. Analysis of the output data shows that these are caused by sporadic outliers in the tracked features. The plotted error is referred to the mean estimate against the true value. Along the sequence and with varying parameters, the mean error is measured at 0.1×10^{-3} m, or 4 % of the true distance. The current implementation runs at 1–3 fps on a Centrino Duo CPU, depending on the amount of features being tracked.

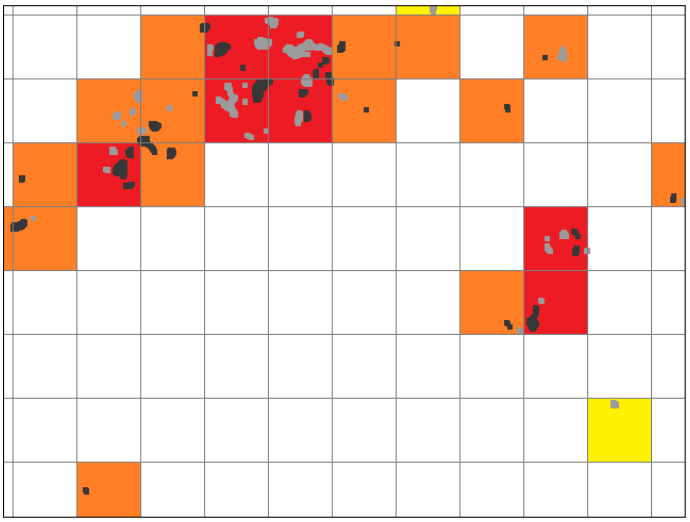

Figure 3.17: Simulation of the expected results after applying a uniform partitioning grid. The HRx rating is color coded on each tile progressively in white, yellow, orange, red.

3.5.2 Considerations

It has been shown how outliers can negatively affect the estimate quality. Overall it appears that the median estimate gives more stable results than the mean, especially when fewer features are being tracked (which is the most favourable case, performance wise). Matching of features is already subject to outlier filtering, by means of a simple match distance threshold. The FLANN method used here has been shown to produce 30 to 50 % false matches based on the initial set of FAST features. The observed correctness of filtered matches was constantly above 90 %.

MOHVE results are a step in the right direction. The reported mean error can theoretically be reduced by acquiring longer tracks, thereby minimizing the impact of matching noise. Sub pixel match correction might be useful in this regard. Additional tests are still needed for further verification. These include: changing camera roll and pitch and changing altitudes.

3.6 SENSOR SETUP

This section covers a discussion about the basic system architecture and parameters optimization that will provide a firm foundation to the navigation algorithms. Once unified, all components will make up the Vision Based Landing Sensor (VBLS).

As demonstrated in Sections 3.4 and 3.5, a monocular camera sensor can provide sufficient scene information to determine a sound solution to the problems of hazard detection and velocity estimation. The camera pointing direction must account for

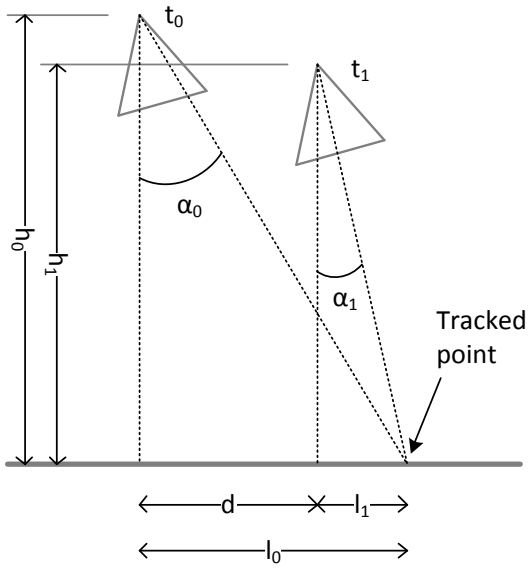

Figure 3.18: Sketch of the simplified motion geometry for horizontal velocity estimation.

the progressive downward pitching trajectory of the spacecraft during descent. It is then recommendable to direct the camera at a forward angle in order to constantly visualize the approaching terrain. An alternative stereo pair arrangement would not have any practical advantage, as the constrained baseline deployable on the spacecraft would be too small for detecting depth along most of the descent. Despite 3D scene reconstruction and motion recovery is possible with state of the art multiple view geometry algorithms, the complexity of such techniques is still prohibitive for the available processing power. Use of a grayscale sensor is sufficient based on the performed scene analysis that showed a substantially uniform spectral distribution in the visual bandwidth.

The remainder of the section is dedicated to parameters selection. In particular: FOV, DOF and integration time. All physical parameters are fixed, meaning that no moving mechanisms (e.g. focusing or aperture) are needed.

With a high horizontal velocity and rapidly changing scene in front of the spacecraft, a wide field of view is desired. A wide angle ensures a better terrain coverage, particularly during TD, thus reducing relocation time in the eventuality that a particularly hazardous area is approached. The expected ground coverage for different angles of view and altitudes was calculated and is listed in Table 3.3. Based on the considerations above, and the fact that very large angles of view result in more severe optical distortions, the choice falls arbitrarily on 50 degrees. For the given sensor size, this translates to a focal length of 6.9 mm. With these parameters, the

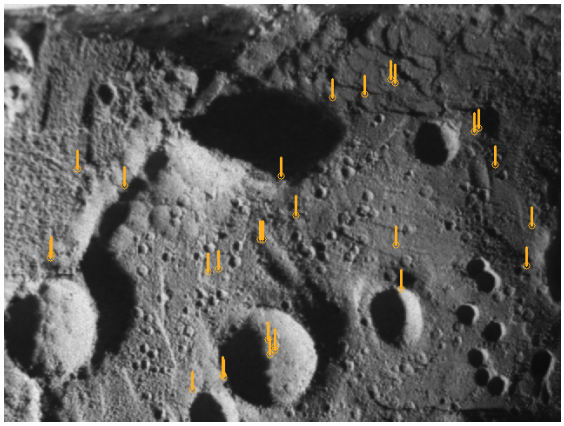

(a)

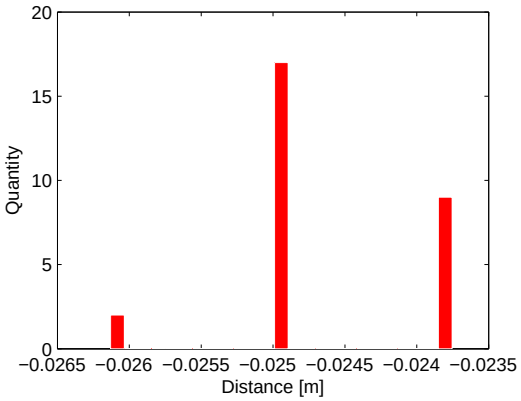

(b)

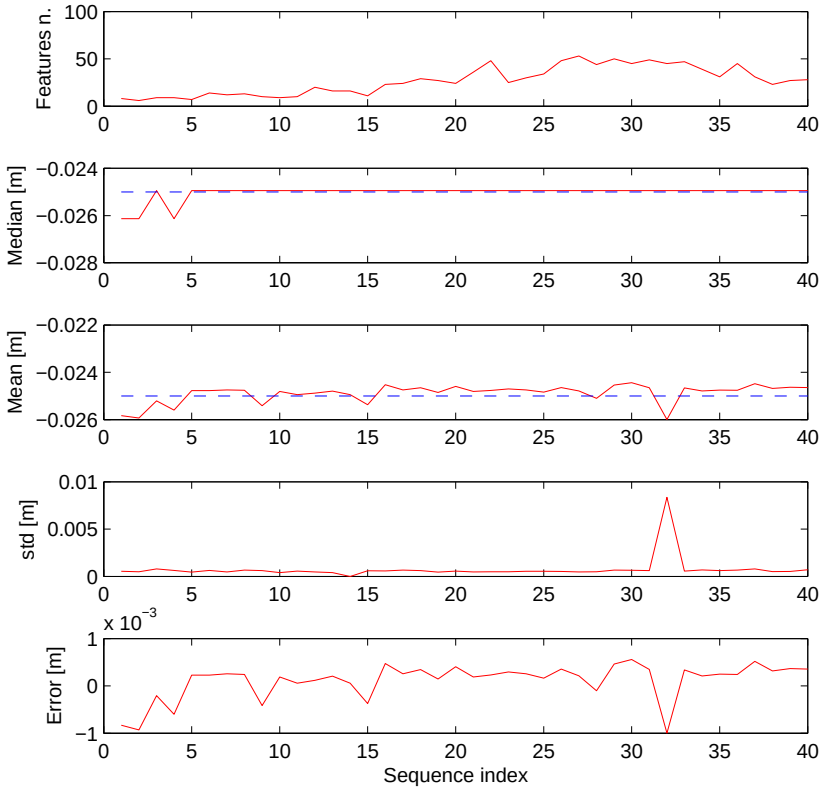

(c)

Figure 3.19: MOHVE results for sequence SEQ-06. FAST threshold: 30. (a) Overlay of the tracked features along the sequence. (b) Single image distribution of the travelled distance estimates for each feature. (c) Statistics of the velocity estimate along the sequence.

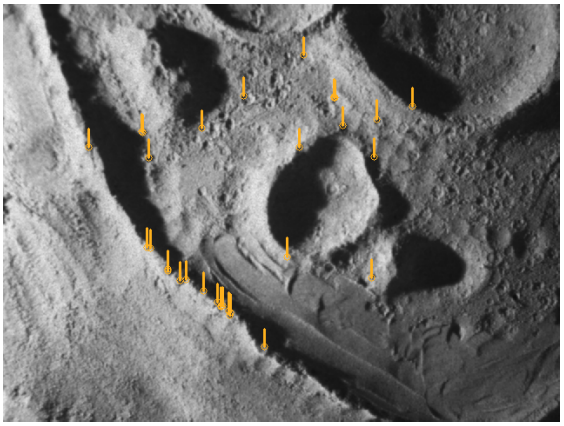

(a)

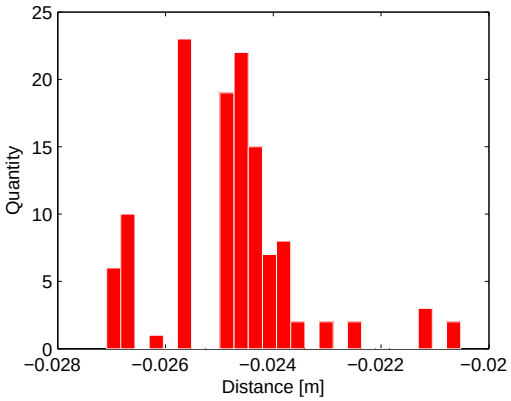

(b)

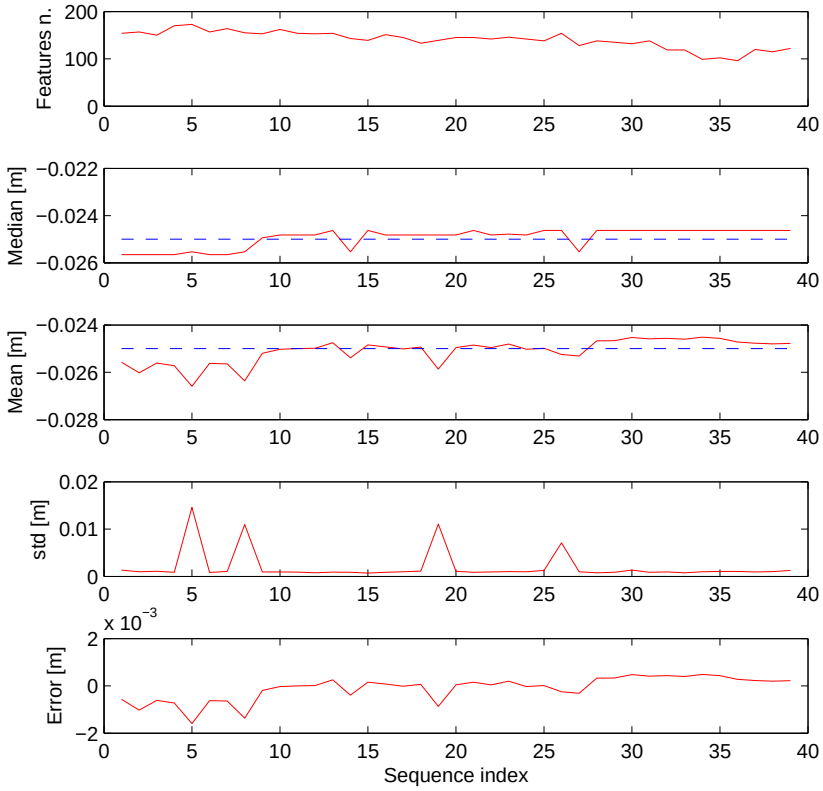

(c)

Figure 3.20: MOHVE results for sequence SEQ-06. 300 fixed starting features. (a) Overlay of the tracked features along the sequence. (b) Single image distribution of the travelled distance estimates for each feature. (c) Statistics of the velocity estimate along the sequence.

$h(m) \downarrow \phi(deg) \rightarrow$	20	30	40	50	60	70
100 k	35.2 k	53.6 k	72.8 k	93.3 k	115.5k	140.0 k
10 k	3.5 k	5.4 k	7.3 k	9.3 k	11.5 k	14.0 k
1 k	352.7	535.9	727.9	932.6	1.2 k	1.4 k
100	35.3	53.6	72.8	93.3	115.5	140.0
50	17.6	26.8	36.4	46.6	57.7	70.0
10	3.5	5.4	7.3	9.3	11.5	14.0

Table 3.3: Ground field of view estimate based on varying angle of view ϕ and altitude h. Unit is meter.

imaged ground resolution is calculated at about 120 m/px from 100 km, down to about 12 cm/px from 10 m. This last parameter ensures that even small hazards will be observable. The larger horizontal field of view can be exploited by rotating the sensor with its long axis in the direction of motion.

To ensure features persistence for robust matching, an image overlap greater or equal to 70 % is considered appropriate. The remaining 30 % will "slide" away at the corresponding projected ground velocity on the image plane. While the ground relative speed from orbit was calculated above ($v_g \approx 1541$ m/s), no detailed information is currently available regarding the velocity profile during descent. Nonetheless, the frame-to-frame time at our disposal at any altitude h is given by

$$t_h = \frac{0.3\, FOV_{lon@h}}{v_{g@h}} \tag{3.14}$$

where $FOV_{lon@h}$ is the longitudinal field of view. For a supposed horizontal velocity of 50 m/s at 1 km, the maximum time available for reacquisition is about 5.6 seconds. Since continuous velocity estimates might not be required by the system specs, the available computation time might be longer than this. Knowledge of ground relative velocity $v_{g@h}$ is also useful to define the upper limit of the integration time before image smearing occurs. For example, this value is found (using the 120 m/px resolution found above) as

$$t_{100\,km} = \frac{120\, m}{1541\, m/s} = 77.8\, ms \tag{3.15}$$

The threshold at 50 m/s and 1 km is 24.5 ms. Naturally these intervals will be longer for smaller pitch angles.

The iris aperture should be chosen to ensure a wide depth of field, covering the range from orbit to landing. The inverse relation between aperture and DOF complicates the situation because a narrow iris has the deterring effect of reducing

the incoming light on the sensor, thereby requiring longer integration times. The problem can be solved with a recursive approach, by choosing an aperture value and eventually adjust if the timing conditions cannot be met. The optical system has another degree of freedom: the focusing distance. This distance affects the close boundary of DOF (and the sharpness of the objects around it), therefore priority should be given at the hazard detection close range of 50 to 100 m. The near and far distances from camera that define the optimal depth of field can be estimated from the following

$$\begin{aligned} D_{near} &= \frac{d\,f^2}{f^2 + F\,d_{cc}\,(d-f)} \\ D_{far} &= \frac{d\,f^2}{f^2 - F\,d_{cc}\,(d-f)} \end{aligned} \tag{3.16}$$

where d is the focus distance, f the focal length and F the optical ratio (f/D, with D the iris aperture diameter). For a maximum tolerated circle of confusion d_{cc} = 10 μm, a focus distance d = 50 m, F = 1 and f = 6.9 mm, we obtain D_{near} = 4.348 m and $D_{far} = \infty$. This result shows a camera system with this configuration would be able to display sharp objects for the whole range.

Based on a plausible Moon landing scenario, mixed with hypothetical system parameters, the radiometric study discussed in Section 3.3.2 can be applied. The conditions are listed in Table 3.4. Localized surface albedo variations will be neglected. The full spectrum scene irradiance of 1361 W/m^2 is filtered by the optics to 612.5 W/m^2. Plugging it into equation 3.2, together with the declared incidence and emittance angles gives a lunar surface radiance of 123.0 W/m^2/sr. Irradiance and photon flux on the image sensor for the lens parameters defined above can now also be evaluated, bringing us to the final equation

$$I = 255\,\frac{N_{e^-}}{FWC} \tag{3.17}$$

where I is the image intensity value for an 8 bit range. The number of released electrons (including noise) is

$$N_{e^-} = \Phi\,A\,t\,q + \sqrt{\Phi\,A\,t\,q + D\,t + N_r^2} \tag{3.18}$$

An image is considered correctly exposed if its histogram peaks around the mid range (in this case 127). For a terrain patch oriented with its normal toward the camera, the camera will give a correct exposure after 12.5 μs. With an irradiance fall-off depending on the cosine of the off-angle, all other illuminated patch orientations will generate pixel values distributed around the mid range. This ideal exposure time falls below all smearing thresholds, further supporting the physical parameters choices discussed so far.

Initial altitude [km]	100
Horizontal Velocity [km/s]	1.63
Pitch from V-bar [deg]	-90 (nadir)
Sun elevation [deg]	45

(a)

Optical bandwidth [nm]	380–760
Sensor size [px]	752×580
Pixel size [μm]	8.6×8.3
Full well capacity	175000
Quantum efficiency	0.35

(b)

Table 3.4: Case study conditions and parameters. (a) External. (b) Internal.

3.7 VIRTUAL SCENE RENDERING FOR VERIFICATION

Physical scene simulations are generally favoured for verifying optical sensors and their algorithms (for example because they allow the use of cameras in the loop). Yet, there are cases where virtual scenes have an edge. Although synthetic photometric models are not as accurate, the 3D modelling tools offer great flexibility in defining scale, illumination and morphology of the generated scene, to name a few. This allows, for example, to render a whole landing sequence from orbit to landing, without interruption. Furthermore, with the available digital elevation models (DEM) from the recent orbiters[1], one can replicate the real world scene with very high fidelity. This provides a good database for testing image based global and local positioning algorithms. The resolutions of these DEMs range from 1 km/px to 50 m/px for various sites of interest. Figure 3.21 illustrates a DEM of the lunar southern hemisphere.

My intention here was to assess the feasibility of rendering a virtual lunar landing scene based on data provided by NASA. Data from LOLA is available on NASA's Planetary Data System (PDS – `http://pds.jpl.nasa.gov/citation/index.shtml`) in various formats from raw data to elevation maps: Experiment Data Record (EDR), Reduced Data Record (RDR) and Gridded Data Record (GDR). GDR contains calibrated and binned data and is therefore the set of interest. The process I have followed is described in the following steps:

1. Acquire data from PDS
2. Import, process and export data in bitmap format within MATLAB
3. Generate a 3D plane in the Blender modelling tool
4. Apply the bitmap DEM to the plane and define multiresolution and displacement mapping
5. Adjust texture and lighting
6. Render

[1]Equipped with laser altimeters such as: LOLA, MOLA, LALT

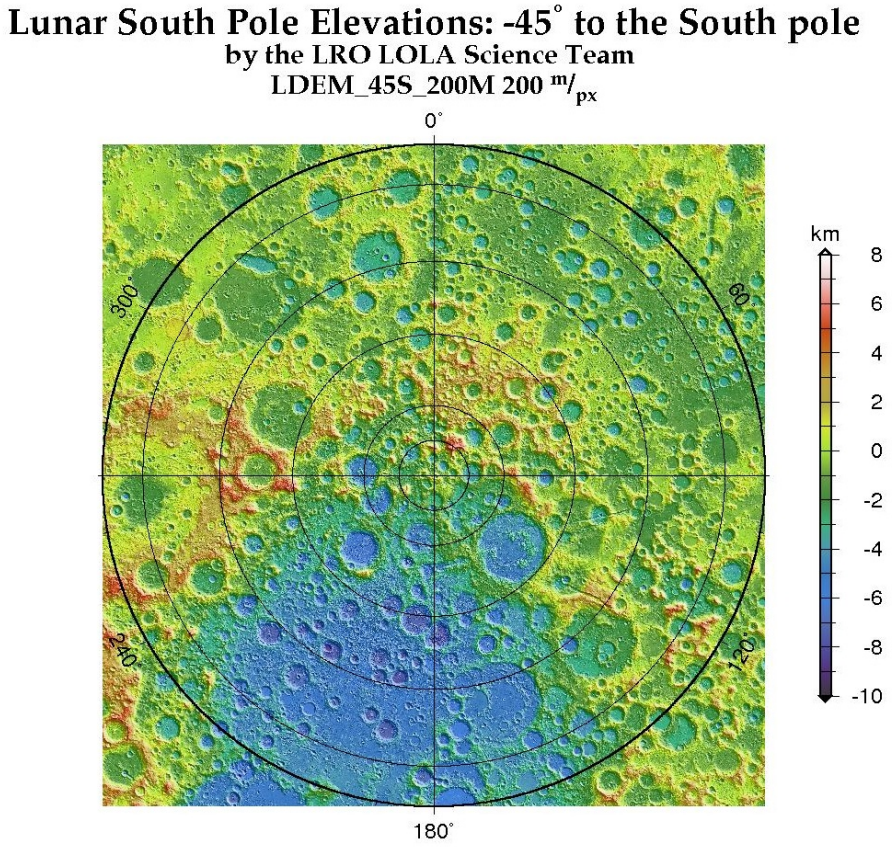

Figure 3.21: DEM of the lunar southern hemisphere from 45 degrees south at 200 m/px. Source: NASA PDS.

Without going too much into detail, the functions of multiresolution and displacement are used to divide the original plane in a matrix of squared poligons, which are then vertically displaced with an intensity defined by the corresponding DEM elevation value. An example of a scene rendered from a region within the lunar southern hemisphere is shown in Figure 3.22. Remaining work consists in the rendering of a continuous camera motion sequence simulating the landing scenario.

3.8 SUMMARY

This chapter has treated the case of precision planetary landing. It has covered a background study, review of relevant literature and analysis of the constraints and peculiarities of a lunar landing scenario.

The study resulted in the development of algorithms for vision based monocular determination of terrain relative horizontal velocity, and detection of hazards during

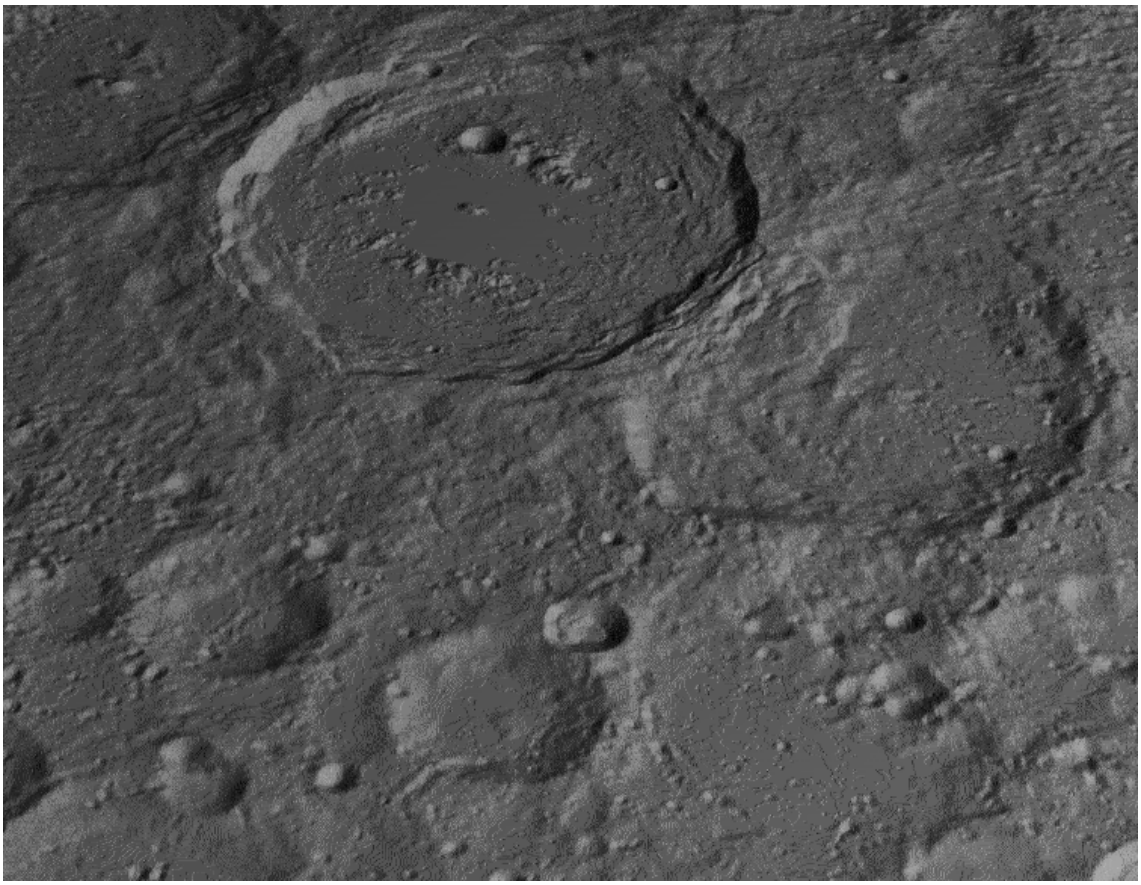

Figure 3.22: 3D rendered scene of a region on the lunar southern hemisphere.

the terminal descent. The techniques have been implemented on an experimental setup and have shown good precision, stability and potential for implementation on a space qualified processing unit for further verification. Testing of the algorithms was done in the laboratory with a camera sensor flying over a representative artificial terrain.

The discussion has also covered the optimization of key physical parameters of the optical system as recommendation for the design of a fully autonomous vision based landing sensor. More details about other internal and external elements will be needed to complete a full design. The photometric model discussed here should be further evaluated in the laboratory in order to verify its applicability.

It was shown how inertial data can be used to integrate additional information that the camera cannot perceive, therefore an inertial measuring unit (IMU) is a welcome addition to the setup. Further investigation in this direction is recommended.

CHAPTER 4

Methods for Optical Instrument Calibration

Calibration is of vital importance in achieving accurate measurements with any instrument. For new instruments though, it can be a challenge to find a comparable reference for calibration. This chapter addresses the subject and discusses some of the methods, procedures and algorithms developed during the project to calibrate the PRISMA vision based sensor.

Calibration is part of the process to ensure sensor's conformance to the measuring standard, so that the measurement error - at least the known bias caused by the instrument itself - is reduced to zero. This value only applies to the ideal case, as in reality it is dependant on the sensitivity of both the calibrating and calibrated instrument. A common threshold is often defined at the noise floor level, under which systematic measurement errors are undistinguishable from the rest.

The DTU Space camera head units (CHU) for the advanced stellar compass (ASC) have been in operation for more than a decade now, and follow a standard calibration procedure covering the internal camera model and the mapping of stars' point spread functions to achieve accuracy on the order of few arcseconds. Based on this instrument, the vision based sensor (VBS) has been developed by the Department to address the field of optical rendezvous and docking of spacecrafts. This is done by solving the 6-DOF problem of determining relative pose and position of a target spacecraft relative to the observer. The sensor implements novel optical metrology techniques, applied to the recognition of a target body pose and position relative to its internal coordinate frame. As the reference model is a collection of optical features, the calibration process requires non standard procedures.

For the most demanding missions, the required accuracy of the lateral position estimate lies at or under the millimetre scale. An example mission is ESA's PROBA-3 experiment to study the Sun's corona. In this scenario, an occulter spacecraft must be positioned at 150 m from a coronagraph spacecraft, equipped with the actual scientific instruments. To give an idea, the formation flight requirements[1] are set at: ± 3.4 mm for lateral positioning and ± 74.2 mm for longitudinal positioning at 150 m.

Discrepancies between the designed models and the physical models cannot be avoided, due to mounting tolerances and post-assembly deformations. Such changes in the target shape require a calibration of the target model that the sensor uses for attitude estimation, while changes on the sensor's assembly structure require calibration of the camera's reference frame. Furthermore, mechanical and thermal stresses induced on the spacecraft's body at launch and in orbit will introduce additional deformations, demanding for updated in flight calibrations for those applications where the highest accuracy is needed. This means dealing with different conditions than on ground: uncontrollable optical conditions and motions defined by the orbital dynamics add more spices to the task. Stray lights, glints and other effects will be detected as additional objects and have to be filtered out by the algorithm. Since these effects are absent in a laboratory environment, it is desirable to collect in flight data which can provide the means to study them and develop a suitable response.

For the sensor to perform as designed, new calibration methods have to be developed. This chapter documents the methods and algorithms that I have developed during the work on the PRISMA vision based sensor calibration and validation campaign.

4.1 COOPERATIVE TARGET CALIBRATION

In cooperative mode, the target spacecraft is outfitted with a set of beacon lights uniformly distributed over its outer shell. The purpose of these is to offer fiducial markers to assist its detection by an external sensor. With the varying and uncontrollable orbital lighting conditions, identifying and measuring the relative target's pose and position is made easier and more accurate. The fiducial markers will be henceforth referred to as *mires*.

In order to have full coverage and prevent ambiguity, the mires are distributed along different patterns on each face. Figure 4.2 shows a picture of the satellite mock-up (1:1 scale) used for the in-house tests. A sketch of the target model is illustrated in Figure 4.1. For the sake of calibration, it is reasonable to approximate the spacecraft to a rectangular cuboid. Each of the six faces is numbered progressively and oriented

[1]Source: PROBA 3 Payload Requirements and Definition Document, P3-EST-RS-7007

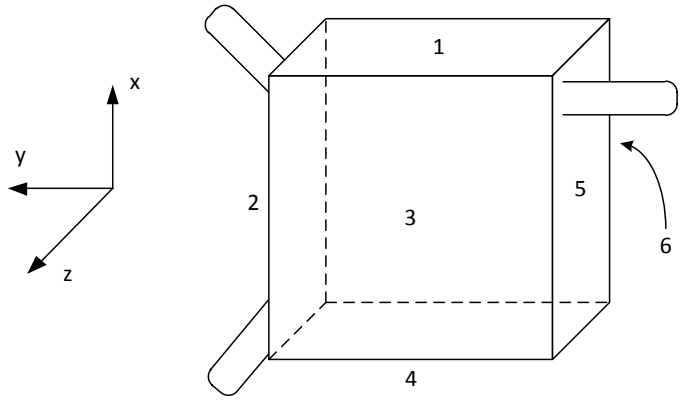

Figure 4.1: Target spacecraft's coordinate frame and panels numbering.

relative to the defined body coordinate frame as shown in the figure. The faces (or planes) can be referred to according to their reference number or to the plane normal axis (e.g. face 3 is also face $+z$).

The algorithms described in this section have been personally developed for the PRISMA target mock-up model at DTU and applied to the flight model (FM) at OHB Sweden (former SSC) prior to launch. With them, a complete calibration of all mires' coordinates has been performed.

4.1.1 First Order Calibration

The process begins with the calibration of each of the spacecraft's faces independently. This is referred to as *face-on* calibration. Each face is identifiable by a specific pattern of mires, which are assumed to lie on the same plane. This is known to be true, within mechanical mounting tolerances, for all patterns with the exception of the smaller docking pattern on face 5 ($-y$), which features an off plane mire. The setup is prepared by placing the spacecraft model at a certain distance from the camera sensor, maximizing the visual coverage. It is expected that the environment is maintained stable, in terms of temperature, absence of external forces and changes of lighting, during the whole data acquisition. The spacecraft model has to be free to rotate and be manoeuvred during testing.

The sensor used for calibration is the same camera system used by the VBS. This instrument is able to estimate attitudes of stars (and other point optical sources) with few arcseconds of accuracy, and its centroiding algorithms maintain the same performance level with the small mires light sources.

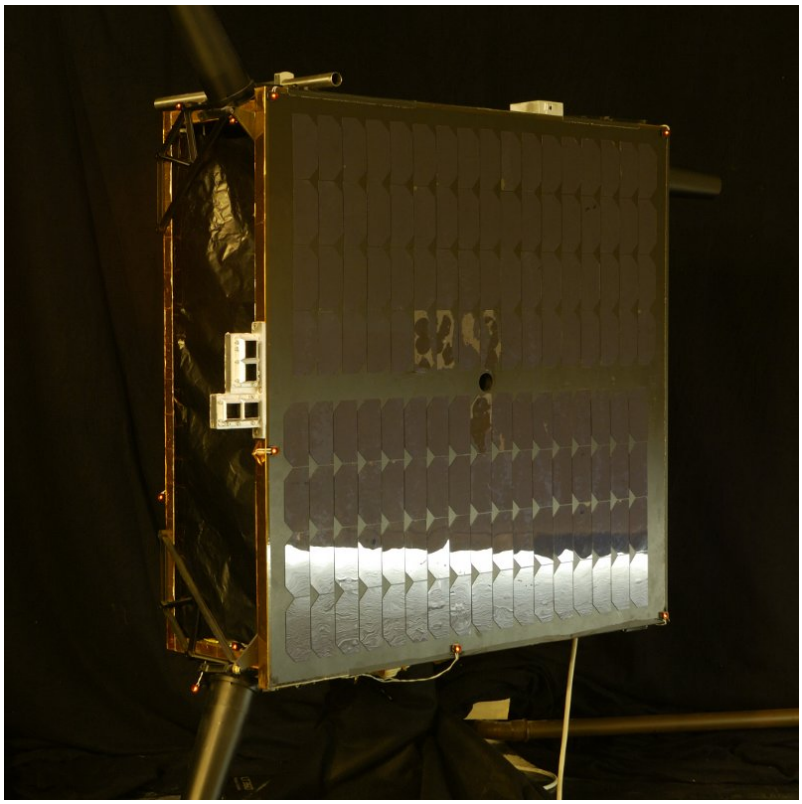

Figure 4.2: PRISMA target spacecraft mock-up model at the VBS calibration facility (DTU Space).

Planar Model

The initial coarse pattern model is based on the hand measured patterns, accurate down to about 1 mm, and provides the initial scale factor. A fine alignment of the panel's normal with the camera's boresight is then performed using a reflected laser technique, in order to suppress perspective distortion of the acquired data. The resulting worst case distortion for a laser point alignment uncertainty of 1 mm and acquisition at 9 m from target is estimated from the maximum tilt angle

$$\delta = atan\left(\frac{1 \times 10^{-3}\ m}{9\ m}\right) \tag{4.1}$$

The perspective foreshortening follows a cosine law, which for two mires distant $l = 1$ m from each other results in an error

$$\varepsilon_{for} = l - l \cdot cos(\delta) \tag{4.2}$$

The error is estimated at about 6.173 nm. This is well below the sensor noise floor and will thus not degrade the calibration.

After the alignment is complete, an extended data set is collected in the form of centroids[1] coordinates (Figure 4.3). Centroiding is performed by the VBS internal routines. The sets are then averaged to reduce noise effects. Lens distortion correction is applied at this stage, based on the Plumb Bob camera model (Brown (1966) and Bouguet[2]), which includes an intrinsic camera parameters calibration. Next, the actual panel calibration is run, with a *back-mapping* process. The imaged centroids' relative distances are evaluated and transformed from image plane to real world dimensions using the initial reference model and the camera parameters. The pattern set is then aligned with the reference and the mires' planar coordinates are extracted (Figure 4.4). A magnified view is also included in Figure 4.5 to show the back-mapping outcome. This procedure is repeated for all six faces and a collection of all the back-mapped panels can be found in Appendix A. The docking pattern on face 5 is a particular case, thus adequate calibration involves error minimization from off-normal acquired centroids.

Residual uncertainty remains about the scale and rotation of the patterns. The scale can be easily corrected by repeating the procedure above at different distances to evaluate a more accurate scale factor. The rotation can only be corrected by edge-on and fine optimization, as discussed below.

Connected Model

An additional calibration phase is necessary in order to evaluate the panels' offset relative to the reference frame and to each other. If these discrepancies are not solved, the model will introduce stress in the pose estimator, and result in unstable solutions. This is not acceptable for a robust rendezvous and docking sensor, thus as a result of this study the following *edge-on* calibration procedure is proposed.

The spacecraft's body coordinate frame origin is, by design, located on panel 6 ($-z$), which is also coincident to the xy plane. This allows to set all panel 6 mires' z coordinates to zero. As the planar coordinates have been extrapolated in the previous step, this face is now fully calibrated. The setup is rearranged with the spacecraft model facing one of the edges toward the sensor, so that two complete face patterns are visible. Combining the adjacent panels (1,2,4 and 5) viewed alongside panel 6 and incorporating the *face-on* calibrated coordinates, the method aims at extrapolating the panel's unknown third coordinate. Assuming inter-panel orthogonality, the algorithm iteratively evaluates the unknown panel's plane offset as the distance from the origin-crossing reference plane. This is done

[1] A centroid is calculated as the optical center of mass of each mire's projection on the image sensor

[2] `http://www.vision.caltech.edu/bouguetj/calib_doc/htmls/parameters.html`

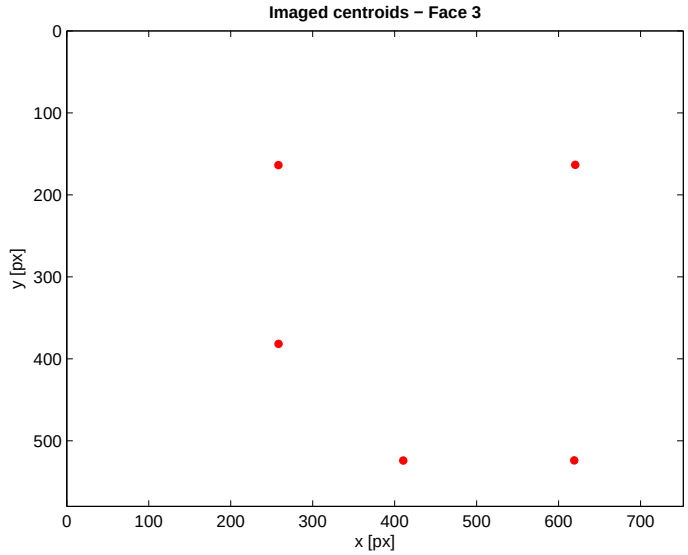

Figure 4.3: PRISMA target FM imaged face 3 ($+z$) centroids acquired for calibration.

by calculating each panel's pose and position individually - with panel 6 used as reference - and translating the second (adjacent) panel from the observed location until it intercepts the zero plane. The translation offset from the starting position to the zero plane is the missing coordinate. This step makes use of the P4P algorithm[1] implemented by Benn (2010) from Abidi and Chandra (1990) and used on the VBS for calculating the planes' pose and position. After the process is run through all edges, all mires coordinates ($[x\ y\ z]$) are calibrated.

Table A.1 lists the mires' coordinates before and after the flight model (FM) calibration campaign at SSC. Plots of all back-mapped panels are also included in the appendix.

The assumptions of planarity and orthogonality of the panels are sub optimal, as they disregard the residual uncertainty about the mires' offsets and the inter-panel tilt and rotation. A more thorough approach is proposed in the following section.

4.1.2 Fine Tuning Calibration

In an attempt to overcome the limits discussed above, alternative methods have been investigated, yet because of project's time constraints, a working implementation

[1]The P4P or "perspective from 4 points", is a technique for calculating a set of co-planar points' pose and position relative to the observer.

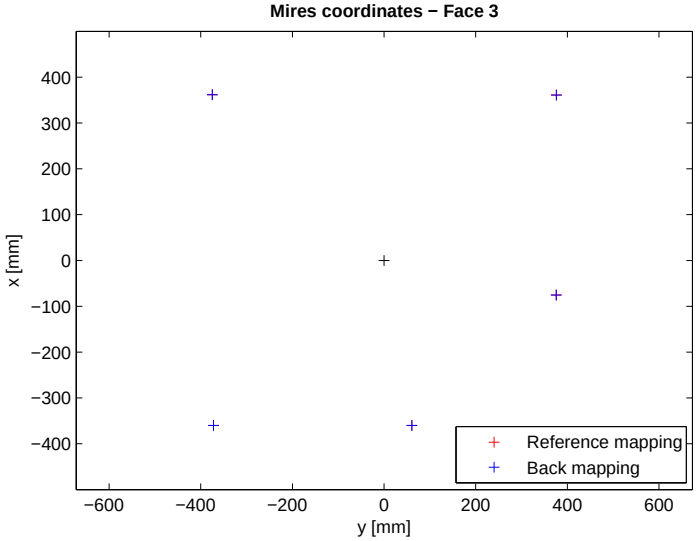

Figure 4.4: PRISMA target FM calibrated face 3 ($+z$) mires expressed in spacecraft frame coordinates.

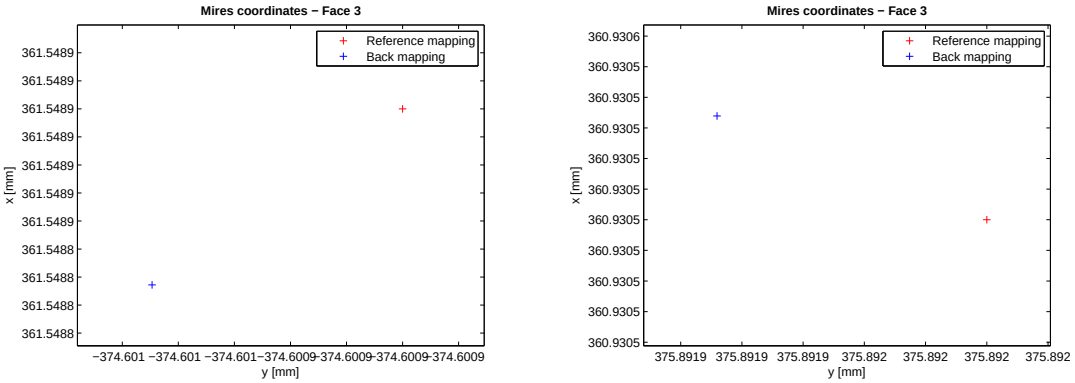

Figure 4.5: Magnified view of the top left and top right face 3 mires, highlighting the back-mapping outcome.

has been pushed further for future work. As mentioned before, due to the strict requirements of spacecraft navigation scenarios, such as formation flight, the sensors must be calibrated for the highest precision. This includes additional compensation for all the spacecraft's plastic geometry alterations induced at launch and the elastic effects during orbit (e.g. thermal deformation), thus requiring flight data processing. The intensity of these effects may require periodic re-calibration.

The proposed method makes use of the same P4P algorithm used by the VBS to compute a plane's relative pose and position. Instead of processing the estimated

Algorithm: Fine Cooperative Target Model Planar Calibration	
1	Acquire and load single face centroids (filtered of outliers)
2	Load reference target model
3	Run P4P to identify the observed face
4	Iterate P4P residual estimate with the mires' planar coordinates as variables of the target model fed to the P4P
5	Find the optimal values and update the model
6	Verify the new model with different data sets

Table 4.1: First phase in the fine tuning of the cooperative target model calibration. Planar model.

data, the problem is formulated as a minimization of a fitting residual. This parameter gives indirect information over the precision of the model, wherefore for an optimally calibrated model, the residual converges to zero. If the P4P estimator is included in an iterative coordinates optimization process, the residual output can be used to progressively minimize the error between the reference mires and the observed ones.

Planar Model

A first step would be to consider each face individually and optimizes the mires' relative planar coordinates. Unlike the previous method, no alignment is required before hand, though it is preferable to select measurements with the least foreshortening. With a single panel in view, the camera sees five mires and calculates their centroids. By using the first order calibrated model as a starting guess, the idea is to optimize the ten total planar coordinates of each pattern. An iterative process minimizes the estimate residual by manipulating these coordinates before feeding them to the P4P algorithm. A constraint has to be added to maintain the plane's scale (e.g. by maintaining the average inter-mire distance constant). Table 4.1 lists the proposed algorithm for calibration of the planar model.

Connected Model

Once again, the target model has to be corrected for the possible inter-panel deformations. If the mires' planar model is satisfactory, the function to minimize depends on the combined $n = 15f$ coordinates of the f number of visible faces. Face 6 is the reference panel, therefore it is used as reference for the initial edge-on calibration of adjacent panels. To ensure model consistency, the process is to be run with data sets of visible faces in all configurations: face (6), edge (12) and vertex (8) on.

One last correction will be required to further refine the model. The distortion is caused by the mires' quartz lens package, which result in the displacement of the

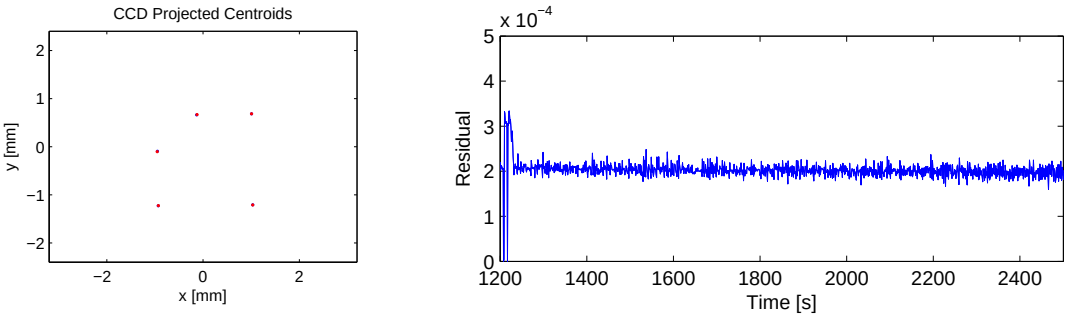

(a) (b)

Figure 4.6: VBS output centroids (a) and fit residual (b) for face 3 of the target mock-up *before* the first order calibration.

visible optical center from the physical location. Such a step could be applied after a first iteration, using an estimate of the face plane as input to the modelled lens centroid shifter.

4.1.3 Results Analysis

The results of the first order calibration are hereby shown and discussed.

Mock-up Model Calibration

The target mock-up (Figure 4.2) was used to develop and verify the calibration methods described thus far. A representative parameter that can help to qualitatively assess the VBS solution stability, as a reflection of the accuracy of the calibration, is the P4P fit residual. This parameter is provided by the system's debug line and was collected during calibration. Fit residuals of a face-on configuration before and after calibration are plotted in Figures 4.6 and 4.7. The post calibration results show a two orders of magnitude residual reduction on the observed face. Similar results were observed on the other panels.

Flight Model Ground Test Campaign

As part of the ground test campaign of the satellites, a session of calibration and testing was carried out, with the aim of evaluating the performance of the system. Figure 4.8 shows the centroids acquired during a full rotation test about the spacecraft's z axis. In the figure are shown in succession the mires visible during the faces transitions: $+y$ to $+x$ to $-y$ to $-x$. The data covers a time span of little under 1200 s. Output from the VBS pose and position estimate is drawn in Figure 4.9.

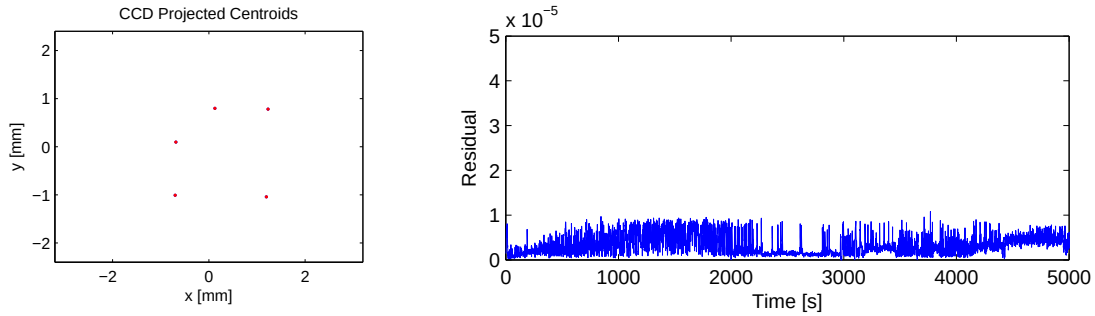

(a) (b)

Figure 4.7: VBS output centroids (a) and fit residual (b) for face 3 of the target mock-up *after* the first order calibration.

This format is now preferred to the residual as it gives a quantitative measure of the calibration's effect.

In the time frame 1–200 s, the evaluated edge-on position of panel 2 ($+y$) and panel 1 ($+x$), expressed in terms of mean μ and standard deviation σ of the coordinates trio $[x\ y\ z]$, is the following.

$$\begin{aligned} \mu_{pos} &= [-51.219 \quad -152.8 \quad 5362.1]\ mm \\ \sigma_{pos} &= [0.078367 \quad 0.13172 \quad 0.52309]\ mm \end{aligned} \tag{4.3}$$

This shows a low and coherent noise on the x and y coordinates and a slightly higher - as expected - deviation on z. In the time frame 650–900 s the evaluated position stability, with panel 5 ($-y$) visible, is the following:

$$\begin{aligned} \mu_{pos} &= [-99.397 \quad -155.95 \quad 5415]\ mm \\ \sigma_{pos} &= [0.92463 \quad 1.5039 \quad 10.64]\ mm \end{aligned} \tag{4.4}$$

As it is clear from the plots and the calculated standard deviation, the solution is less stable than previously observed. This is a sign of stress in the estimator - thought to be worsened by the docking pattern - which can only be reduced by further improving the model. The erratic position manifested during panels transition from $+y$ to $+x$ (between 300 and 600 s) is disregarded, as the manual re-positioning of the spacecraft was all but stable.

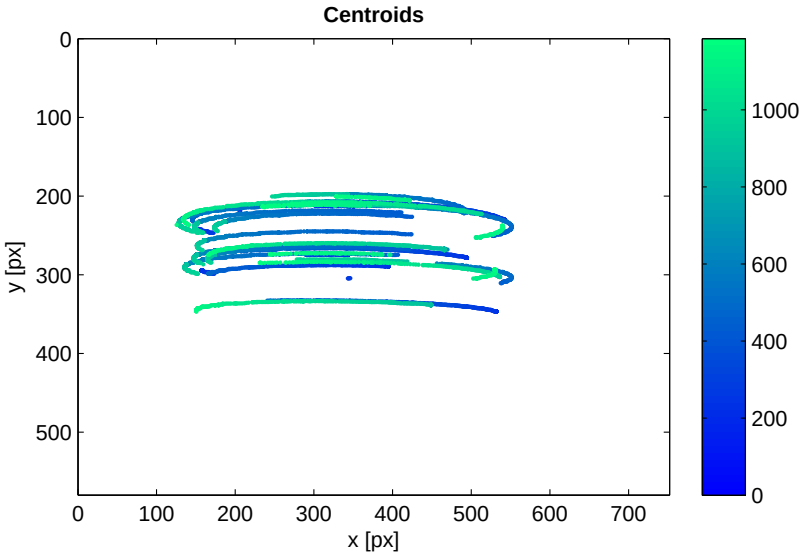

Figure 4.8: Visible target centroids during a PRISMA FM ground rotation test.

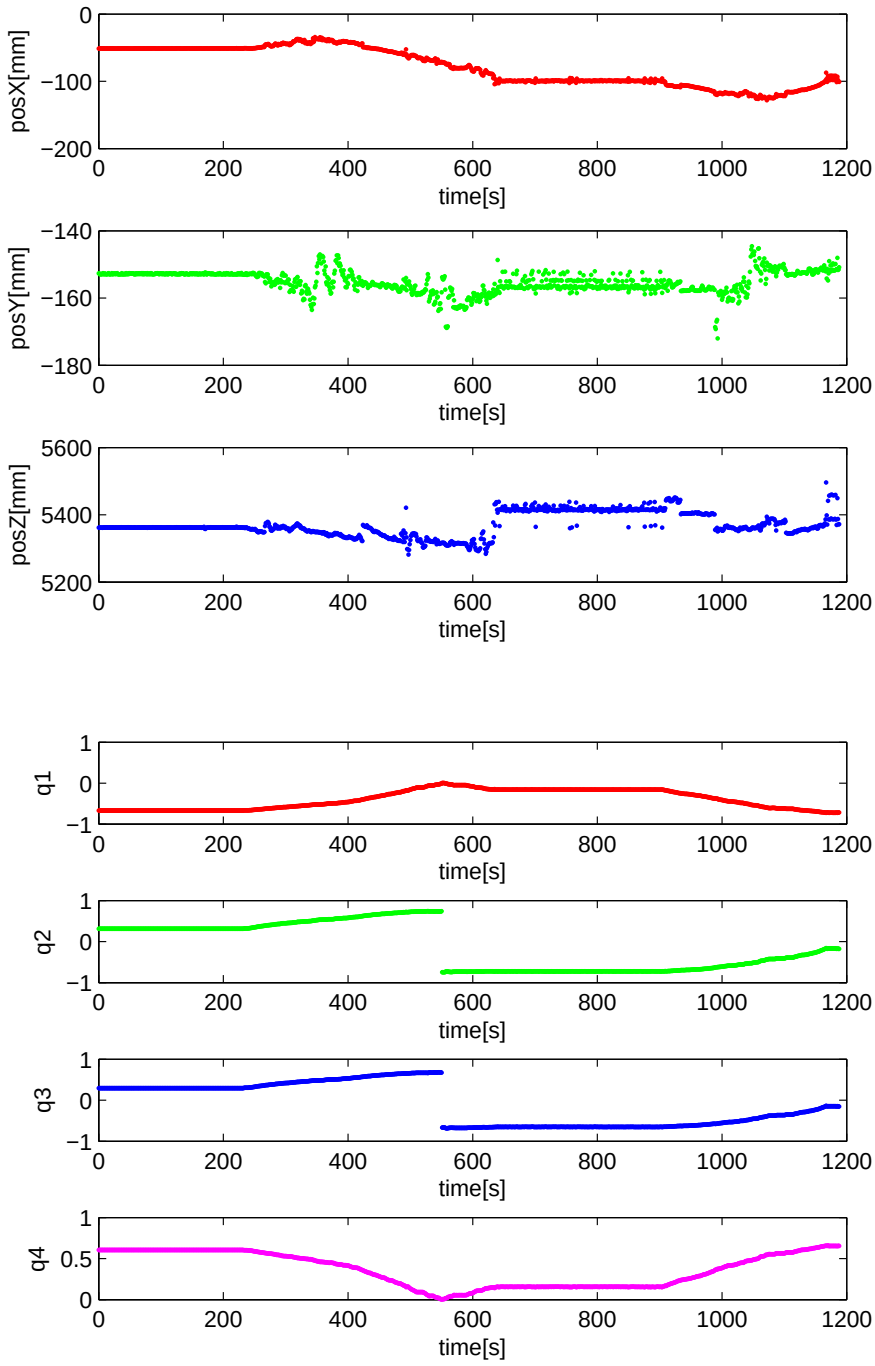

Figure 4.9: VBS estimated target position and pose during a PRISMA FM rotation test.

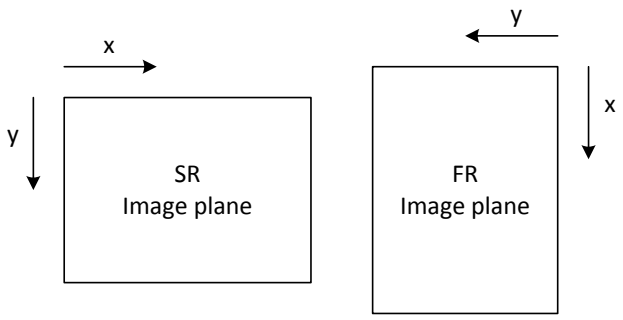

Figure 4.10: VBS cameras planes relative orientation.

4.2 CAMERAS INTER-CALIBRATION

The sensors used for rendezvous operations have to cover long ranges of distances, from far range sighting until close range approach. Due to that, more than one sensor should be employed and optimized for each range, so as to improve the detection and tracking performance. PRISMA has been equipped with a dual head vision based sensor (integrated with two additional star cameras), with the two heads covering both short (SR) and far (FR) range. The cameras are not mounted on an optical bench, and are therefore more susceptible to the post launch effects described above. Furthermore, the image planes are rotated from each other of about 90 degrees about the boresight (see Figure 4.10). To ensure minimum bias during mode transition, and thus improve stability, the transformation between the cameras has to be calibrated. This section describes the algorithm I have developed to do that.

The algorithm is described in Table 4.2. The process begins with the selection of an appropriate data set, extracted from available PRISMA Early Harvest in-flight data. The criteria for selection are: far distance target (>1 km), non-cooperative mode (LEDs off), target in both cameras' FOV. A transformation between two coordinate frames can be represented by a rotation matrix $\mathbf{R}$ and a translation vector $\mathbf{t}$. These are combined with the following formula, which transforms a point $\mathbf{p} = [x_P \; y_P \; z_P]^T$ from the FR camera frame to the SR camera frame.

$$\mathbf{p}_{SR} = \mathbf{R} \cdot \mathbf{p}_{FR} + \mathbf{t} \tag{4.5}$$

Due to the points' long distance from camera, the translational offset is negligible ($\mathbf{t} \approx [0 \; 0 \; 0]^T$), therefore the transformation is only made of rotations. The method described here applies the 3-2-3 rotation sequence of body axes to compose the rotation matrix. The angles are known as Euler angles and will be defined $[\varphi \; \vartheta \; \psi]$, following the common notation (Shuster, 1993). Lens distortion correction, based on

Algorithm: VBS cameras inter-calibration	
1	Load data sets (n centroids)
2	Synchronize data sets
3	Load cameras parameters
4	Perform lens distortion correction
5	Project the FR centroids to world reference frame
6	for i = 1 to n
7	Re-project i-th point from world to SR camera image plane
8	Evaluate error
9	Minimize error as function of the transformation parameters
10	end for
11	Evaluate optimal values
12	Evaluate resulting error

Table 4.2: The inter-calibration algorithm for transforming the target attitude from far to short range camera.

the Plumb Bob model (Brown (1966) and Bouguet[1]), is also included for improved precision.

The optimization process is based on minimizing the transformation error, evaluated as the euclidean distance between the measured SR centroids and the transformed (FR to SR) centroids. A direct search method is used, because of the few parameters involved and no constraints on the time available. Figure 4.11 shows a selected sequence of the tracked target centroids on both cameras. These sets cover the center and one edge of the image planes. The region between snapshots 3600 and 4100 is not considered, as the target was out of the SR FOV. In Figure 4.11b the y coordinate of the FR camera is inverted to better show the correlation between the cameras' alternated axes. The centroids, as projected on the image plane of each sensor, are displayed in Figure 4.12a and 4.12b.

4.2.1 Results Analysis

The evaluated optimal Euler angles (3-2-3) are the following:

$$\begin{bmatrix} \varphi \\ \vartheta \\ \psi \end{bmatrix} = \begin{bmatrix} -1.576898 \\ 0.000028 \\ 0.000087 \end{bmatrix} rad \tag{4.6}$$

This allows to compile the rotation quaternion from the FR camera to the SR. In the following, the real part is the fourth element.

[1] `http://www.vision.caltech.edu/bouguetj/calib_doc/htmls/parameters.html`

$$q_{FR \to SR} = \begin{bmatrix} 9.9301 \times 10^{-6} \\ -9.8688 \times 10^{-6} \\ 7.0923 \times 10^{-1} \\ 7.0498 \times 10^{-1} \end{bmatrix} \tag{4.7}$$

These are in accordance with the expectations of about -90 degrees roll and present, but minor, effects over the remaining rotations. With these in hand, the far range centroids can be transformed, by means of perspective projection and Equation 4.5, to the short range image plane and compared against the actual measures. The calibrated set of parameters includes the SR camera principal point coordinates, which is estimated at:

$$\begin{pmatrix} C_x \\ C_y \end{pmatrix} = \begin{pmatrix} 377.42 \\ 289.60 \end{pmatrix} px \tag{4.8}$$

Figures 4.13 and 4.14 illustrate the outcome of the optimization process. From the two plots we can see a closer match in the first data set than in the second. At the same time is apparent how each set "pulls" in opposite directions. The difference is clearer in Figure 4.15. Here the pre-calibration and post-calibration error vectors are plotted alongside each other. This shows a significant improvement for the first data set (up to snapshot 1150), whether it tends to degrade in the second. Combining the two sets, the error vector has a mean listed below.

$$\mu_{error} = 0.69\ px \approx 122" \tag{4.9}$$

Closer observation of the data (Figure 4.16) reveals discrepancies in the continuity of the two sets. There are two possible causes generating this and affecting the quality of the calibration. First, the data sets have been acquired during spacecraft activities, therefore vibrations were surely present on the cameras' mechanical interfaces, as can be seen by the noisy central data set. Second, the two camera optics are designed for different depths, and may produce differing target image representation and cause the system (e.g. the centroiding process) to generate discording solutions. Finally, the same considerations are valid for the camera's principal point calibration, as this is more accurately achieved on ground with a calibrated pattern, offering a wealth of geometrically arranged feature points.

4.3 SUMMARY

As discussed in this chapter, the calibration process is vital to achieve a precise estimate of the target spacecraft as seen by the vision based sensor. The methods described for cooperative target calibration can greatly improve the fidelity of the estimate. A properly calibrated model can make the difference between a safe

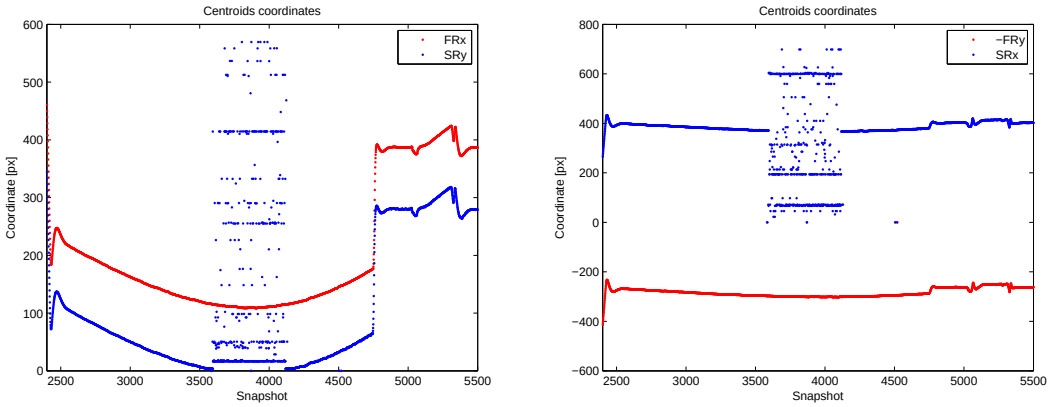

(a) (b)

Figure 4.11: Target centroids coordinates of the selected data sets for both SR and FR camera. The plots show a correlation between the alternated axes. FRx with SRy and vice versa.

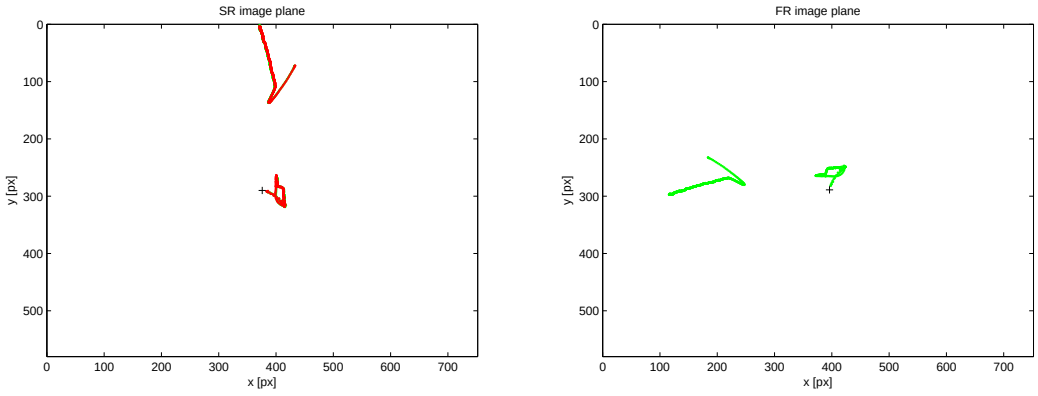

(a) (b)

Figure 4.12: Detected target centroids on the SR (a) and FR (b) image planes.

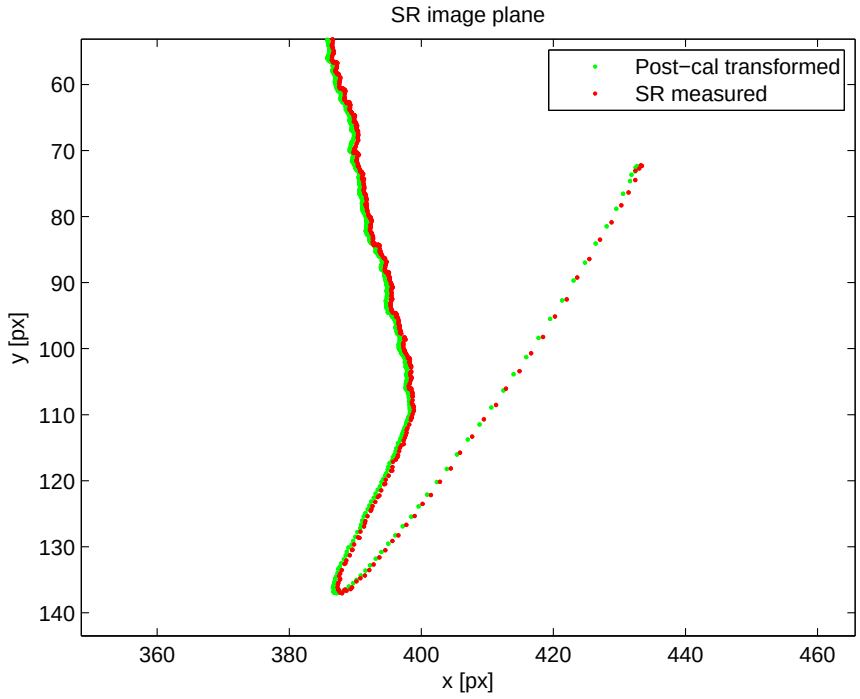

Figure 4.13: Top edge data set shown as the original SR measured centroids (red) and the post-calibration transformed centroids (green).

rendezvous and a potential accident, as the navigation filters, once tuned for the highest performance, become very sensitive to noise and unstable measurements.

The implemented calibration technique has delivered a good first order model, with sub-millimetre precise planar coordinates. For missions that require micrometre scale, especially during panel transitions, more advanced techniques are needed. The laboratory described in Chapter 6 offers precise and controllable tools for the development of new calibration methods at DTU Space.

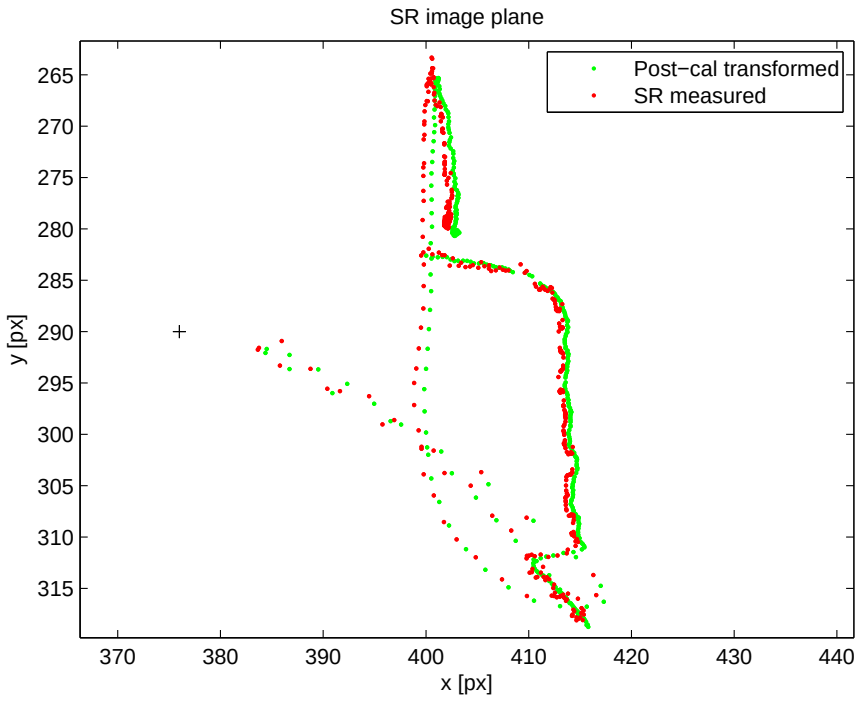

Figure 4.14: Central data set shown as the original SR measured centroids (red) and the post-calibration transformed centroids (green).

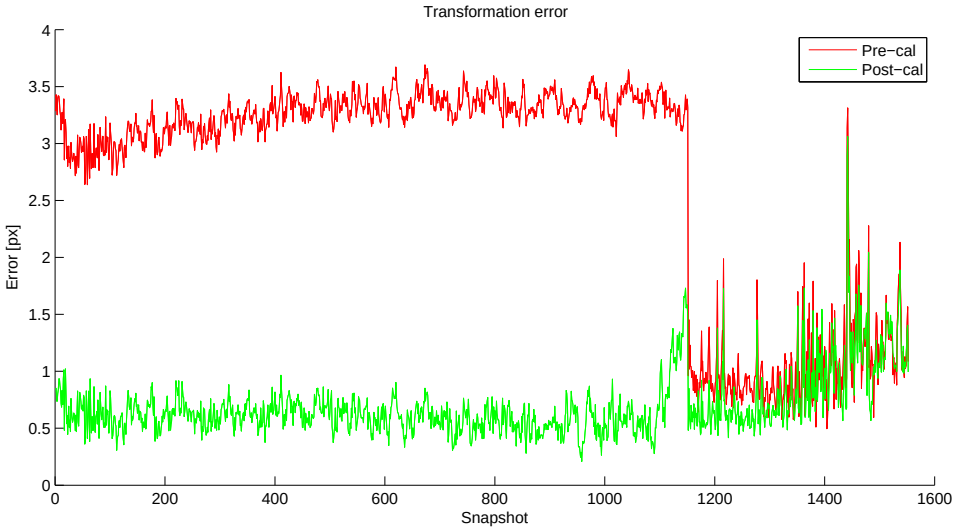

Figure 4.15: Plotted error between the measured and transformed centroids on the SR image plane.

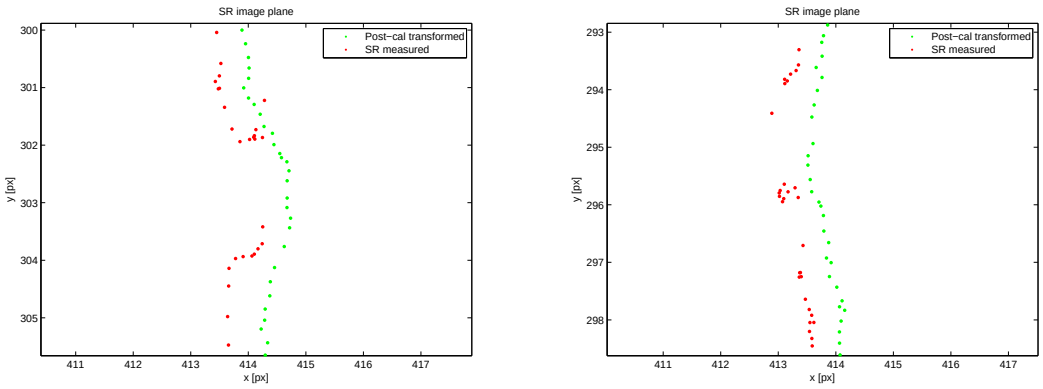

Figure 4.16: Magnified central data set segments of the original SR measured centroids (red) and the post-calibration transformed centroids (green).

CHAPTER 5

Pharos OGSE

Verification of certain aspects of a space-borne sensor often requires the development of specific tools and methods, as the target operating environment is not at hand. The tools are meant to emulate, with sufficient realism, the conditions under which the sensor will work, so that compliance to the specifications can be verified.

The far range (FR) mode of PRISMA, as designed by DTU Space and described in Benn (2010), is active when the target spacecraft is located at a considerable distance from the sensor, at a range varying from 500 m to 1000 km. When this is the case, the spacecraft's body features cannot be distinguished and Sun reflections dominate over the fiducial points, installed on it for cooperative navigation. Optically, the target will appear as a small light source, undistinguishable from the firmament in the background. If the chaser and target spacecrafts are in approximately the same orbit, as is the case for a typical rendezvous scenario, their relative motion leads to the target moving with a predictable angular velocity relative to the stars. This information is used as input to the FR target detection filters. After the target is locked, its attitude relative to the camera (RA and DEC) is estimated and rendezvous procedures can be initiated.

As part of the campaign for the verification of the VBS functionality, various test setups have been built with the objective of testing each of the system's operating modes. The specific requirements for FR and IR (intermediate range) mode verification set by the system can be synthesized as follows:

- Provide a fixed reference constellation,

- Provide a controllable point light source within the mission defined angular velocity range. E.g. For a LEO scenario, this can be set around 150–300 ”/s.

In order to achieve the highest realism, Benn (2010) performed an outdoor test on real sky where the VBS camera head unit (CHU) was facing up towards the stars and a linear guide was used to drive a LED along the field of view. The setup is shown in Figure 5.1. This setup is able to verify the FR navigation filters functionality, but has some limitations. Beside the practical issues arising by the fact that the instrumentation has to be brought outdoor during the night and with clear skies, therefore making it infeasible to operate on flight systems, the slider structure is sizeable and very wind sensitive. In view of these considerations, a more compact and portable device is desirable. Pharos is the module - classified as optical ground support equipment (OGSE) - resulting from the contribution that this project has given to the VBS verification campaign.

5.1 FIRST GENERATION

5.1.1 Concept and Design

The Pharos has been designed to satisfy the requirements for algorithms verification for the detection of a distant target during orbital chase. The module concept is based upon DTU Space's star field stimulator (SFS), an OGSE tool used for verifying the microASC basic operations. Pharos is designed to combine with the SFS without interfering with its standard functionality and is assembled on the inside of the 120 mm SFS circular plate. The SFS is a well established tool for testing the department's highly accurate CHUs, and it is therefore considered a reliable platform.

The optimal choice for the target light source - i.e. the simulated optical representation of the target spacecraft - is a LED combined with an optical collimator. This small device offers a well defined light beam with a uniform spectrum and its magnitude can be adjusted as desired along a range from -1 to 10 Mv. The beam is about 50 μm in diameter. A standard SFS collimator has been modified in order to provide a single point source in addition to the constellation collimators.

As the SFS design gives limited room to move around, all components should be confined within a safe region. This region (marked by a green point-dashed boundary line in Figure 5.2) ensures that there will be no obstructions to the surrounding constellations light beams. Various designs have been investigated for steering the target towards the camera. For example, an inverted pendulum structure is considered to provide the most effective dynamics for the case, but a practical design has not been implemented.

A first prototype implementation, sketched in Figure 5.2, is based on light deflection induced by refraction through a glass window. If a wedge glass window is tilted,

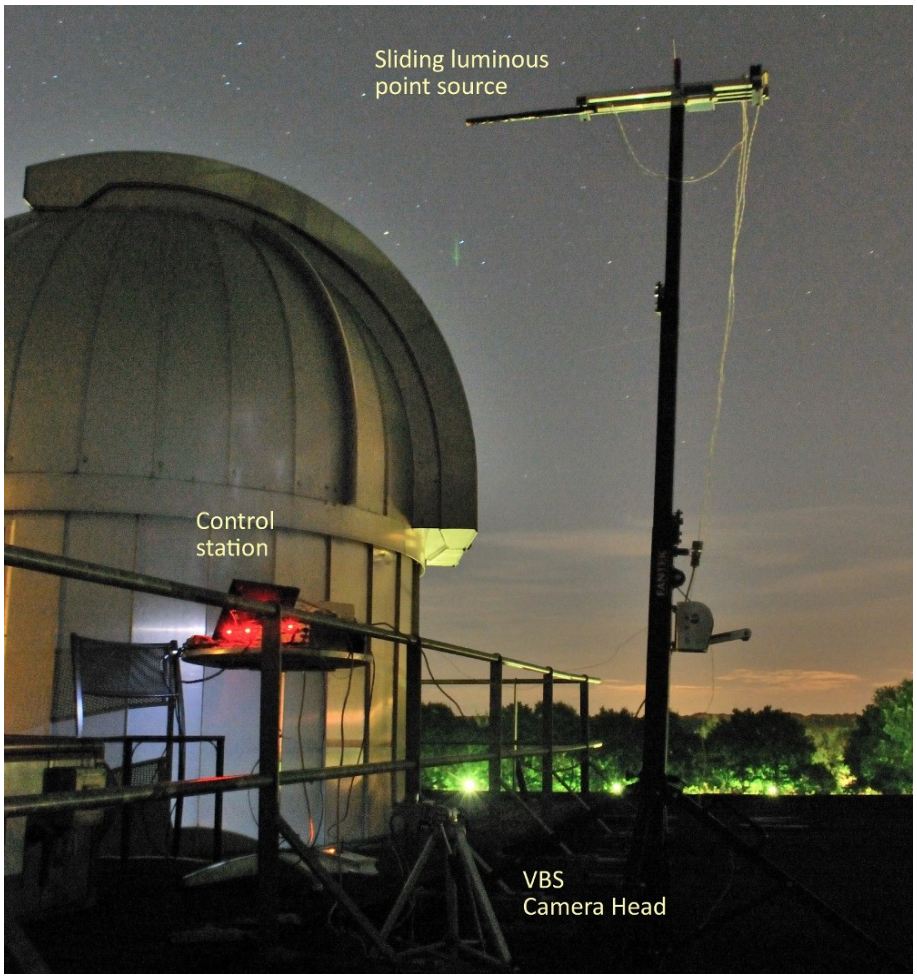

Figure 5.1: Real sky test setup for far range VBS verification. The CHU is at the bottom with its boresight aiming towards open sky. Above it, a slider moves a LED along the camera's field of view simulating a distant object.

for example by means of a rotating lifter, this deflection can be easily achieved. In this case, the lifter is mounted on a motor's shaft as in the figure. A wedge window is a glass element whose entrance and exit faces are slanted of a small angle relative to each other. Table 5.1 lists the optical properties of the N-BK7 circular wedge window manufactured by Qioptiq (formerly Linos) used in Pharos. All features yield to a desirable component allowing a clear light beam with an accurate and easy to estimate deflection.

The continuous beam deflection is obtained by the combined effect of a rotating lifter element and a flat phosphor-bronze sheet. The sheet acts as a spring to maintain the window's location fixed, allowing only rotations around its pivot point.

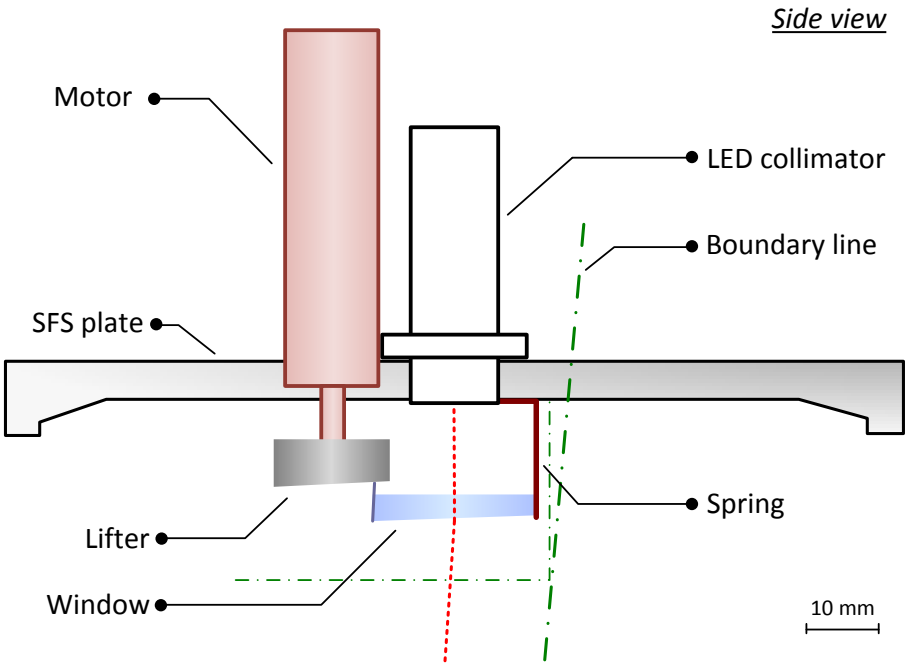

Figure 5.2: Pharos module v1 design. Optical refraction is used to steer a light beam towards the camera sensor.

Material	BK7
Refraction index	1.5157
Diameter [mm]	22.4
Reflectivity [%]	0.5
Flatness	$\lambda/4$
Wedge angle [deg]	3.867
Deflection angle [deg]	2

Table 5.1: Qioptiq N-BK7 wedge window specifications. The indicated deflection angle is the nominal value for a beam entering the window with zero incidence.

Phosphor-bronze is considered a good material for this purpose because of its fine elastic properties and ease of use. In the calculations below it is assumed that the pivot point is fixed, even though the spring deformation will cause it to move slightly. This is taken into account when verifying the actual module swath. The top face of the lifter element - on which the window is pushed at all times - is slanted, therefore rotating the lifter around its vertical axis (normal to the SFS plate) induces a repeating oscillatory motion of the window. A picture of the assembled module is

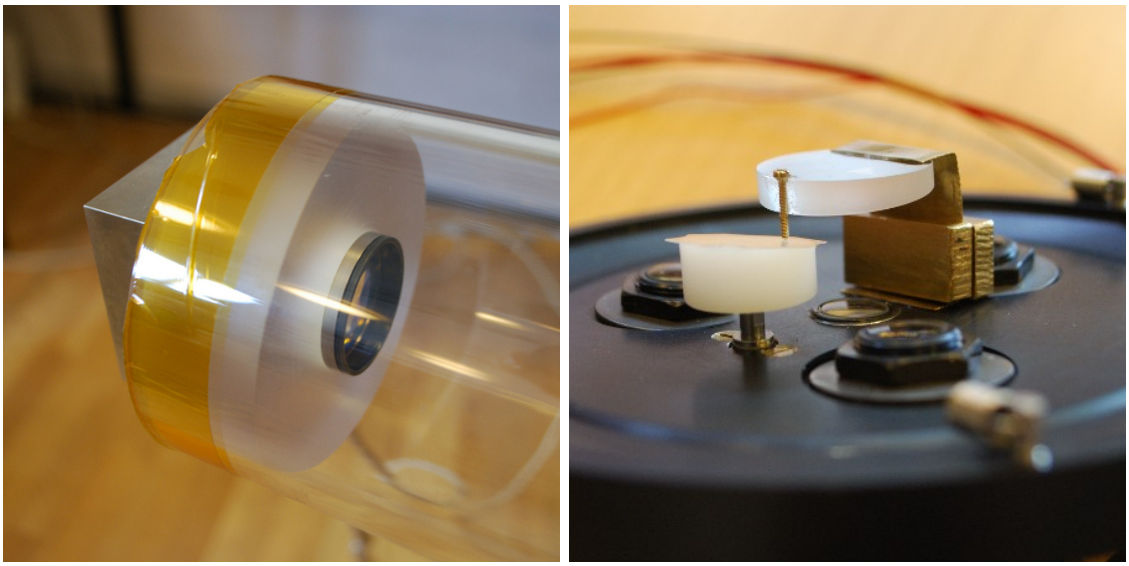

Figure 5.3: Pharos module v1 assembly pictures. (left) CHU mounted on the far end of the assembly tube before obscuration. (right) Interiors of the assembled module, with the window pressed against the lifter.

Type	DC brushed
Diameter [mm]	13
Power [W]	1.2 @ 12 V
Gearing ratio	1119:1
Nominal speed [rpm]	5970

Table 5.2: Maxon RE-max DC motor specifications.

shown in Figure 5.3 right, whereas on the left we can see the CHU attached to the other end of a support cylinder before obscuration.

The motor requirements - small size, constant torque and slow operating speed - can be satisfied by using a standard DC motor with an appropriate gearing attached. The gearing allows to run the motor at nominal speed, thus providing optimal torque. A very high reduction is required for a motion that would represent a slow moving target. Less play and better torque are obtained with the use of metal gears and ball bearings. Table 5.2 lists the specifics of the Maxon RE-max motor selected for the module. The beam oscillation period can be regulated varying the voltage on the motor and will be on the order of a few rounds per minute with the selected gearing.

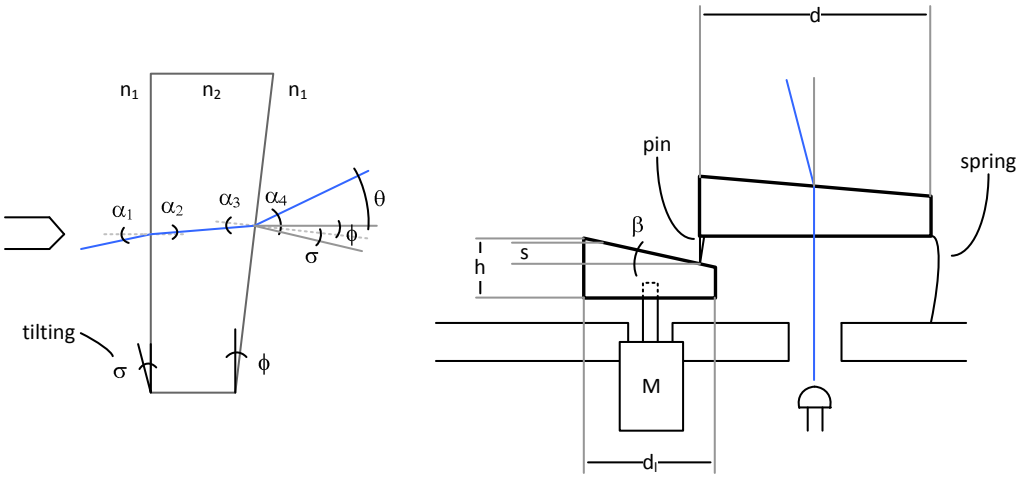

Figure 5.4: Pharos module v1 geometry. (left) The change in refraction indices (n_1 and n_2) will cause a light beam entering the window to be refracted twice before exiting. By design, a beam entering with incidence $\alpha_1 = 0$ will have an exit angle $\theta = 2°$. (right) The motor M rotates the lifter on which the wedge window sits. The tilting amplitude can be easily calculated by knowing the window diameter d and the vertical displacement s.

5.1.2 Geometrical Model

A geometrical model of the beam refraction has also been studied. The problem can be divided in two parts as in Figure 5.4:

- Evaluate the path of the refracted optical beam through the window (left drawing).
- Quantify the effect of window tilting by evaluating the geometry of the window/lifter interaction (right drawing).

Snell's law comes in aid for solving the first problem. Being α_1 the incident angle of the entering beam, n_1 and n_2 the refraction indices of the air and glass (BK7) and ϕ the wedge window slant, the other angles are calculated as:

$$\alpha_2 = asin\left(\frac{n_1}{n_2} sin(\alpha_1)\right) \tag{5.1}$$

$$\alpha_3 = \phi + \alpha_2 \tag{5.2}$$

$$\alpha_4 = asin\left(\frac{n_2}{n_1} sin(\alpha_3)\right) \tag{5.3}$$

$$\theta = \alpha_4 - \phi - \alpha_1 \tag{5.4}$$

If formulas 5.1 to 5.4 are merged, the exit angle can be represented as a function of the incident angle. Since this angle in fact corresponds to the window's tilt σ, we have

$$\theta(\sigma) = asin\left(\frac{n_2}{n_1} sin\left(\phi + asin\left(\frac{n_1}{n_2} sin(\sigma)\right)\right)\right) - \phi - \sigma \tag{5.5}$$

The second problem is simpler to solve. This time we want to calculate the maximum tilt induced by the lifter to the window. If we consider the position of Figure 5.4 (right) as the starting position with $\sigma = 0$, then the final position σ_{max} is

$$\sigma_{max} = \frac{1}{2} asin\left(\frac{s}{d}\right) \tag{5.6}$$

where $s \approx 1.5$ mm is the actual measured lifter's slant vertical fall and $d = 22.4$ mm the selected window's diameter. Finally the full beam swath can be quantified by differentiating the extrema values.

$$swath = \theta(\sigma_{max}) - \theta(\sigma_0 = 0) \approx 27" \tag{5.7}$$

5.1.3 Verification

Verification of the module is performed by assembling Pharos and the camera head unit on either side of an obscured tube (Figure 5.3 (left) and Figure B.3). Protection against external lighting is a critical requirement for the functionality of the system. The module is oriented so as to reduce the effects of gravity on the moving parts. In this configuration, the setup is ready for VBS verification.

After various design optimizations aimed at the spring and lifter elements, the results of the camera tests can be analysed. Figure 5.5 groups the temporal traces of the target centroid as observed by the camera during a continuous swing test. On plots *(a)* and *(b)* we can see the centroid motion with a color scaling from blue to green to help making out the temporal evolution. The left image is focused on the image plane. The right image outlines the temporal evolution along a third dimension. Two main effects can be observed: a marked hysteresis and a motion along both axes. As the module was aligned so as to perform a swing along the vertical axis on the image plane, the secondary motion that we observe here must come from another source. Both effects can be attributed to spring torsion deriving from the pin/lifter interaction. This behaviour became well known during the various tests, but was never fully suppressed. Trials involved reducing the pin/lifter contact friction by changing the lifter's surface material and grinding the pin tip. The optimal surface, used in the test described here, is glass. On the opposite side, a clamping of the spring body was added but has resulted in limited improvement.

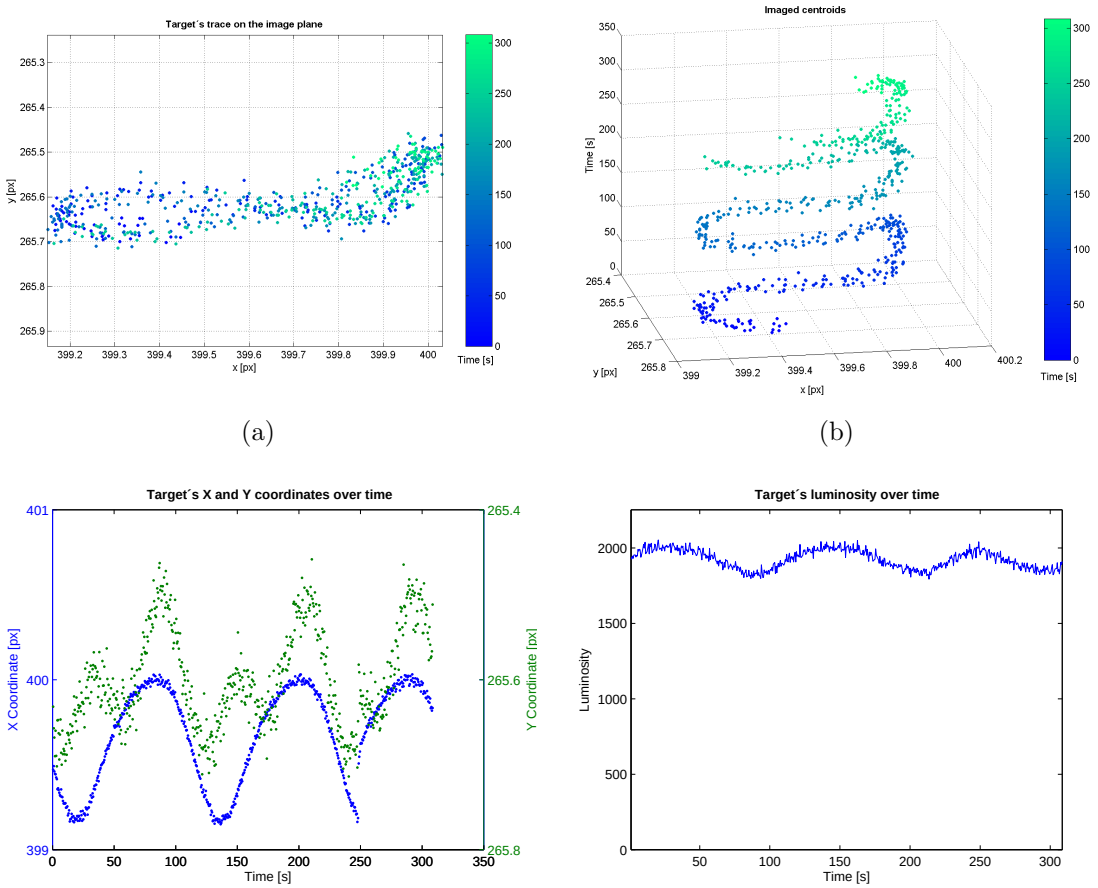

Figure 5.5: Pharos module v1 test results. Despite a smooth oscillation, the plots show how the moving target suffers from several drawbacks. Top left shows a marked hysteresis with target moving on an *8* pattern. Bottom left highlights that this is due to a non rectilinear motion along the y axis. Furthermore, bottom right shows luminosity oscillation during motion. A positive remark is instead the high repeatability that can be observed on both top plots.

The module's functionality is not hampered, though the resulting motion will be too errant to be acceptable for the VBS verification. If only the vertical motion is taken into account, an amplitude of about 0.25 pixels or 21" is measured (for a module-to-camera distance of about 270 mm and 8.6 μm pixel height). The theoretical swath (Equation 5.7) is confirmed, after accounting for the mechanical uncertainties and approximations. The mean angular velocity is found to be 2.646"/s. Plots *(c)* and *(d)* show the centroid's coordinates independently and its luminosity along three cycles. We can notice another undesired effect in *(c)*, where the y coordinate is

periodically "jumping" to another location. Again this is assumed to be caused by spring stress release. The luminosity decrease of about 10% from its peak value during each cycle does not affect the VBS verification. This is because in the real world scenario, the target may be in free spinning and/or under varying illumination conditions.

Summing up, thorough testing of this first prototype device has shown some main drawbacks: limited target controllability, hysteresis and other secondary effects. More importantly, the module does not satisfy the second requirement for VBS verification as the target swath is narrow and its angular velocity is well below the theoretical range expected from a low Earth orbit scenario which the module is meant to simulate. Because of the non optimal performance, ideas for a new and improved design have been put together and the outcome is described in the following section.

5.2 SECOND GENERATION

Pharos revision v2 has been designed with some new goals in mind, derived by the observations and experience of the previous tests:

- Provide a better user interface,
- Improve beam controllability and repeatability,
- Improve stability and possibly reduce hysteresis,
- Cover the expected angular velocity range — around a few hundred seconds of arc — and a wider travel range, to enable extended VBS verification.

5.2.1 Concept and Design

The new design employs mirrors and highly accurate linear actuators. With the combined intermission of a fixed and a tilting mirror, the beam can be dynamically steered towards the camera. Figure 5.6a shows the components layout and the light path entering from below and directed towards the camera. The actuators are sitting under the front edge of the left mirror. As the image sensor will only receive light passing through the optical head, the circular base of the beam's conical swath will be defined by the iris. This constrains the area of the image on which the target will be visible.

First face mirrors are the most suitable for the task as they avoid internal light absorption and multiple internal reflections. Two triangular prism mirrors with reflectivity $> 96\%$ (for $\lambda = 500$–2000 nm) have been selected for the purpose.

The motor's selection has required a thorough investigation of the possibilities available on the market. An approximate value for the required travel distance can be estimated. For a swath amplitude $\alpha = 2$ degrees, a chosen mirror side length

of about 12 mm and assuming for simplicity that the mirror will rotate about its right angled vertex, the travel distance d is found inverting the equation below. The actual design locates the motors' axes below the mirror, slightly further from the edge, therefore the arm length is taken as 11 mm.

$$\frac{\alpha}{2} = atan\left(\frac{d}{11mm}\right) \tag{5.8}$$

This gives a maximum required travel distance of about 200 μm. The motor requirements can be synthesized as: micrometer resolution, continuous linear motion, small size. The required angular velocity is very small, therefore the motor should be able to run at low speed. This limits the selection to piezoelectric motors and stacks. Another option involving the use of electromagnetic actuation has also been considered. This solution would offer considerable benefits because of the frictionless actuation, but has been discarded due to the less controllable non linear nature of the magnetic force. Piezoelectric actuators have seen a dramatic development lately and manufacturers offer different solutions to generate motion. One type uses rows of microscopic legs of piezoelectric material which are in contact with a free moving rod serving as the actuating axis. Another possibility is the use of stacks of piezoelectric materials used for direct actuation. These two offer the same order of resolution, though piezo stacks have very low dynamics compared to their size. Piezo stacks are generally more favorable for applications with high loads. Finally one more technique uses the principle of a nut and bolt. A nut shaped piezo material is stimulated to produce "wiggling" oscillations. A screw with rounded ends is inserted in the nut and can be pushed along the cavity's axis in both directions.

The survey has resulted in the identification of two candidate devices: one based on piezo legs and one on piezo nut. Their specifications are listed in Table 5.3. PI offers a device with an extraordinary low resolution and sturdy design. For this purpose though, the travel range is well beyond the requirements and so are its size and load rating. There is limited room for components on the Pharos plate and the spring load will not be more than a few grams. The New Scale Squiggle, on the other hand, satisfies all the requirements with its very compact dimensions, load rating and resolution.

5.2.2 Detailed Design

The module's architecture can be seen in Figure 5.8, with all Pharos components enclosed in the same box. The system is made of two sections: electro-mechanic at the bottom and optical at the top. Accordingly, the continuous arrows indicate physical interaction, whereas the dashed arrows represent optical transmissions. A control board, which interprets the commands and generates the modulating signals for driving the motors and a sensory setup for closed loop operation, is located on

Model	Technology	Resolution [nm]	Travel [mm]	Max load [N]	Size [mm]	Cost [Euro]
PI NEXLINE N-310	Piezo legs	1	125	10	25×25×12	3000+
New Scale Squiggle 1.8	Piezo nut	500	6	0.50	2.8×2.8×6	550

Table 5.3: Specs list of candidate motors for Pharos v2. The indicated cost includes controller.

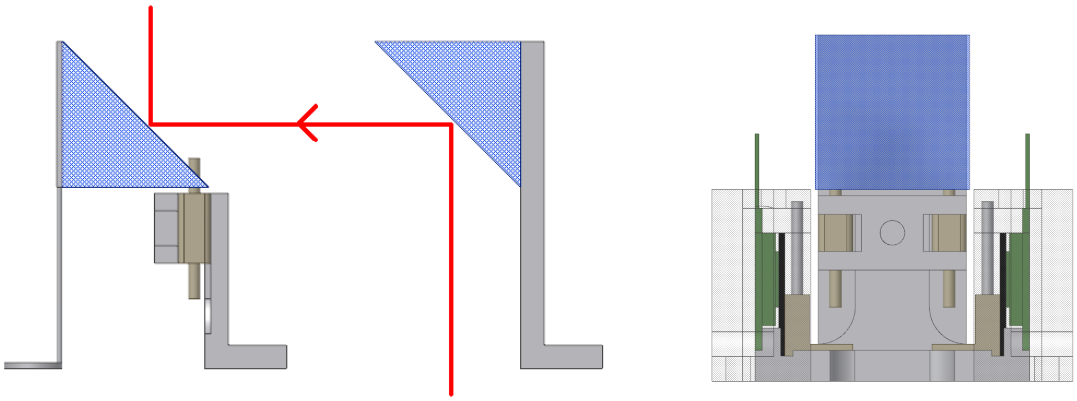

(a) (b)

Figure 5.6: Pharos module v2 operating principle. The light beam (red line) is reflected by both mirrors towards the camera head. The first mirror is rigidly fixed to the structure, whereas the second mirror is only fixed with an elastic rod on one side. Two linear motors (brown in the figure) allow differential steering of the mirror. The drive feedback structure can be seen on the right drawing (partially hidden) with the magnets (black) constrained along two rails and facing the sensors (green).

the outer face of the plate. A PC USB connection is required for operating the motors.

Figure 5.9 shows the integration of the module's components on the internal plate of the stimulator. The three yellow rods are star collimators (note that that third is covered in the figure), arranged on a circle at 120 degrees from each other and are again the only parts belonging to the original SFS design. They each compose a three "stars" constellation of different patterns projected onto the camera. The light source is a LED whose emission is collimated to a well defined thin parallel beam, thus satisfying the first requirement. All the additional Pharos parts are enclosed within the boundary defined by the star collimators. A critical part of the design

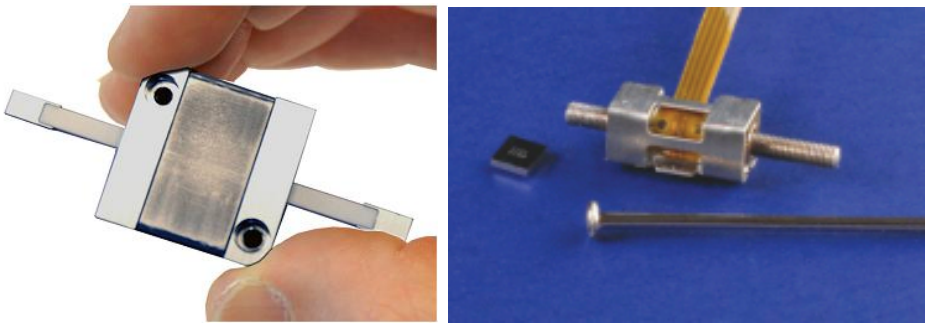

Figure 5.7: Two candidates have been found and evaluated for actuating the mirror. (left) PI N-310. (right) New Scale Squiggle 1.8. The pictures are taken from the relative catalogues.

has been to ensure that none of the moving parts would interfere with these fixed references by obstructing the light paths.

The target simulating light source is again generated using a single point collimated LED entering the chamber orthogonally to the plate. A moving point source is obtained by deflecting the incoming beam's incident angle on the camera. Any variation of this angle will translate directly to a planar displacement on the image sensor. The two mirrors are located in front of the entrance beam and on the support plate. Mirror 1 is fixed on a rigid support so as to redirect the beam towards mirror 2, whose task is to steer the beam through the differential action of two linear piezo-motors acting on its lower face. Mirror 2 is held in place by a wire spring, which constrains its motion and ensures continuous load on the motors. The motors' positioning and the spring shape give mirror 2 one or two degrees of freedom, depending on whether the motors are actuated synchronously or asynchronously. This allows manoeuvring the light beam within a conical area, whose boundaries are defined by the motor's axis length. The effective boundaries are defined optically by the receiving camera lens (aperture and distance from the module).

As the motors by themselves cannot achieve high positioning accuracy, an extended design has implemented a magnetic sensor feedback loop with circuits provided by the motor's supplier. A mechanical structure supporting the sensors against a dual rail system has been built around the two motors. Figure 5.6b shows a rear view drawing where the components of the feedback loop can be seen on their symmetric layout. Each rail drives a magnet running alongside the sensing chip. Care was taken to ensure the highest magnetic field strength on the sensors by accurately spacing the components. This parameter can be verified within the Pathway motor control software (Figure B.5). The closed loop design results in improved controllability and sub-micrometre positioning accuracy. Technical drawings of the designed supporting elements can be found in Appendix B.

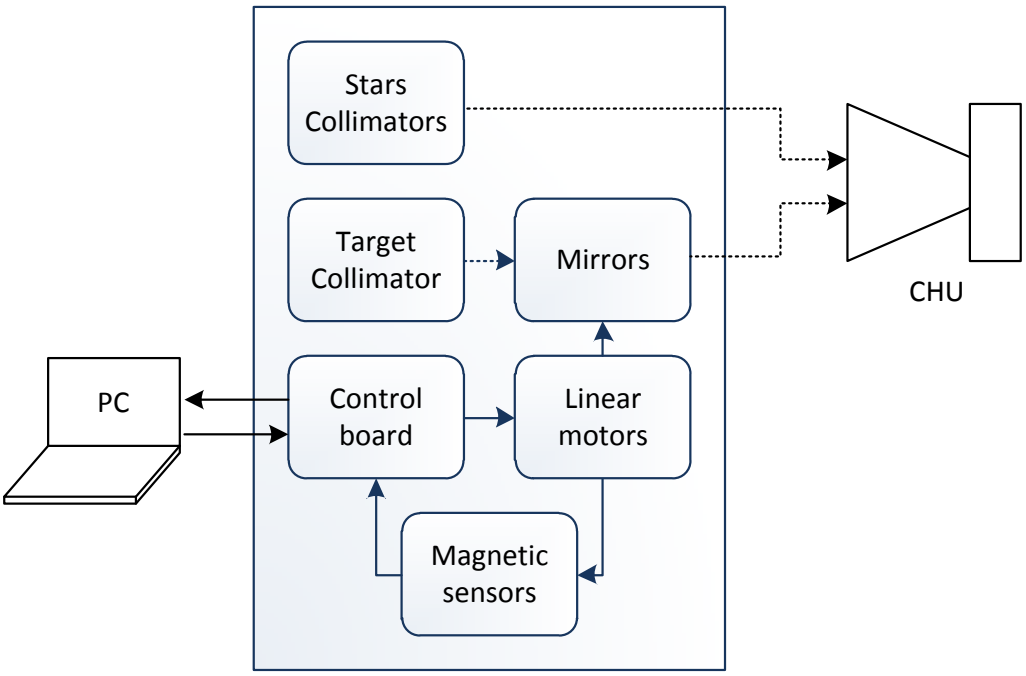

Figure 5.8: Pharos module v2 architecture. The module is interfaced with a PC and optically stimulating a camera head unit. The dashed lines represent optical transmission.

5.2.3 Module Verification and Validation

The process is divided in two phases: first a preliminary verification with standard μASC and then a validation against the VBS algorithms. The test setup is essentially the same as the first generation, though this time the system requires a connection between the controller board and a PC. Figure 5.11 represents a snapshot of the camera view in the initial state, when the target beam is aimed at the camera center. This color inverted view shows all the regions of interest captured by the sensor. Beside the central target centroid, the three constellations are also clearly visible.

PHASE 1: Basic functionality

In order to achieve a simulated target satellite velocity of a few hundreds arcseconds per second, the motors are driven close to the lowest speed allowable by the controller: 5 μm/s and continuous steps in alternate directions. The speed value is constrained by internal frictions and the applied load. The travel distance, derived

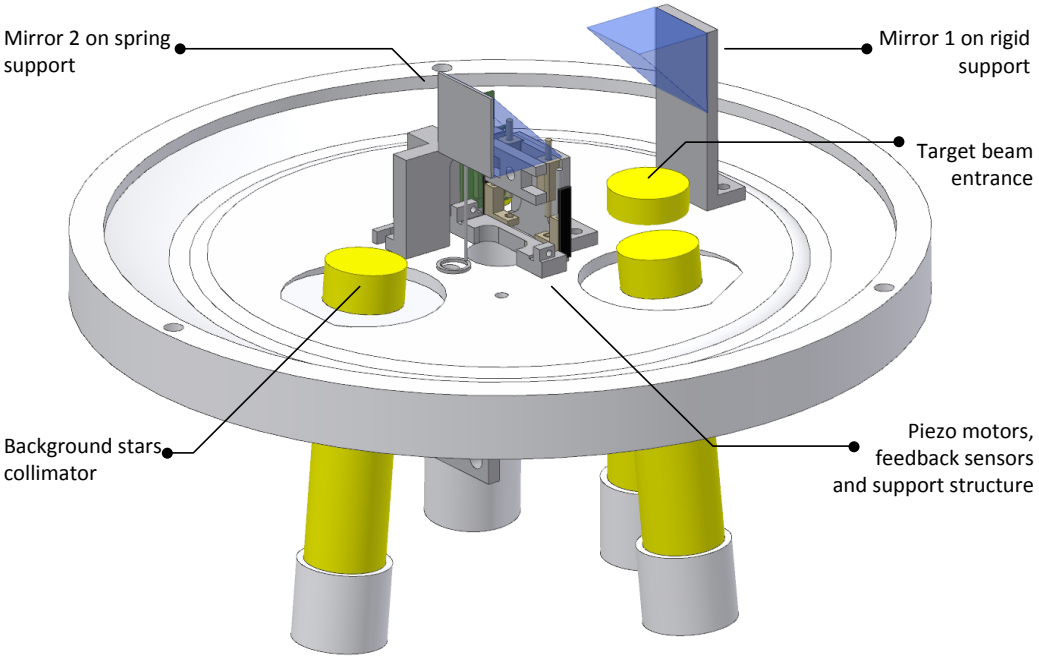

Figure 5.9: Pharos module v2 internal layout. The close side of the support structure is hidden to allow vision of the internal arrangement.

above for a 2 degrees swath, is fixed at 200 μm. Equation 5.8 can be evaluated inserting velocities instead of distances in order to calculate the theoretical beam angular velocity. Again, a rotation about the mirror's right corner is assumed.

$$\dot{\alpha} = 2 \cdot atan\left(\frac{5\mu m/s}{11mm}\right) = 187.513"/s \tag{5.9}$$

Pharos is now operated with the Pathway PC software provided by New Scale. The application handles communication, parameters settings and direct control and supervision of the motors. This can be used for example to switch between open and closed loop operation, and to observe the motors' position, error and status in real time (snapshots of the application have been included in Appendix B). Motor motion can also be programmed with dedicated scripts.

The initial tests documented here have verified the basic functionality of the module: actuators operability, proper stars and target centroiding and acceptable lighting. The tests are identified by the code P2tFnn, standing for: *Pharos 2 test - Feedback* followed by a progressive number *nn*. Figure 5.12 reports the visible centroids as they are collected by the star camera during test P2tF01. The motors

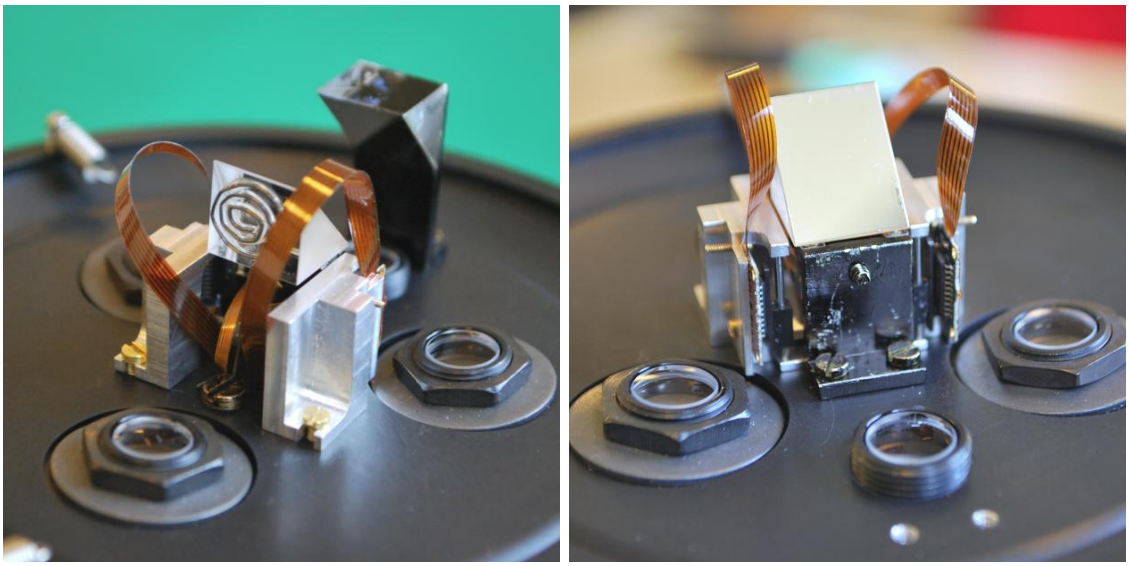

Figure 5.10: Pharos module interior. (left) The whole structure is assembled as by Figure 5.9. (right) The rigid mirror support has been removed to show the dual rail arrangement for closed loop control. The symmetrical structure enables the magnets to slide in concert with the motors. For scale reference, the mirror side length is 12.5 mm.

were moved synchronously for short steps each time. As in Figure 5.11 the expected ten centroids are continuously visualized. In addition, the target is moving on a quasi-rectilinear path along the y direction. Uniform luminosity of the target beam is reported in Figure 5.13.

Since Pharos v1 was found to be sensitive to gravity effects on the spring, some specific tests have been arranged to assess the response of v2. In this instance the module generated a forward and reverse motion with 2 degrees of amplitude (about 90 px). In the test P2tF02, the mirrors have been aligned vertically in two different configurations:

a P2tF02a: Motors above spring
b P2tF02b: Motors below spring

A horizontal mirrors configuration is expected to give uneven loads on the motors and is therefore not considered. A vertical boresight configuration has been tested but it is not documented here, as the final VBS verification is expected to be performed with a horizontal camera boresight.

For test P2tF02 travel range and speed were again 200 μm and 5 μm/s respectively. Figures 5.14a and 5.14b show the target centroid region of interest. The temporal evolution is represented in color scale from blue to green. In the forward

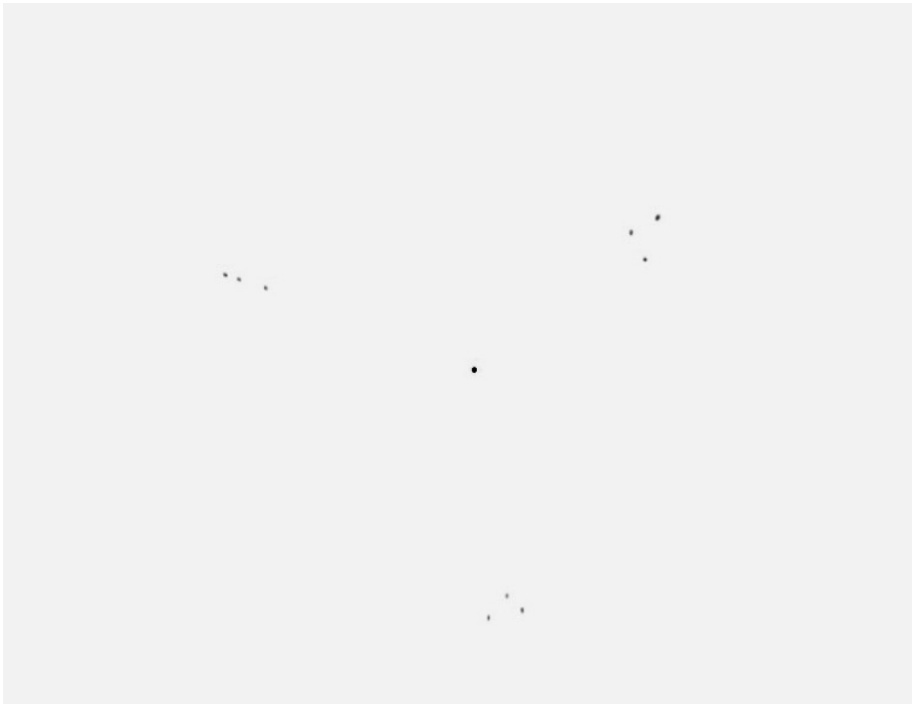

Figure 5.11: ROI image of the projected firmament and target source from Pharos to the CHU. The three constellations are visible and correctly represented with the target point lying at the center of the image. Colors are inverted for clarity.

motion (prevalently blue) the motors push the mirror away, while in the reverse motion (towards green) they simply resist to the spring push. The motors were commanded to return to the starting point. Orientation *a* seems to provide a more repeatable motion as the target returns to the starting point, though hysteresis is present. Orientation *b* resulted in a deranged forward motion despite the high precision drive. Nonetheless, both configurations have consistently shown a rectilinear reverse motion, thus making it the most favourable for the following tests regardless of the orientation.

PHASE 2: VBS verification and module validation

A dedicated session has been run with the star camera's VBS functionality activated. The same hardware setup is used with motors above mirrors in reverse motion. The following parameters have been set on the system.

A custom star catalogue is commanded to the ASC prior to any Pharos test, in order for the VBS to classify the Pharos star constellations as stellar objects. The system will then provide "true" attitude data as in flight. The dedicated test P2tF03, resulted in successful verification of the velocity filters and validation of the module's features. Figures 5.15 and 5.16 document the achievement. The target

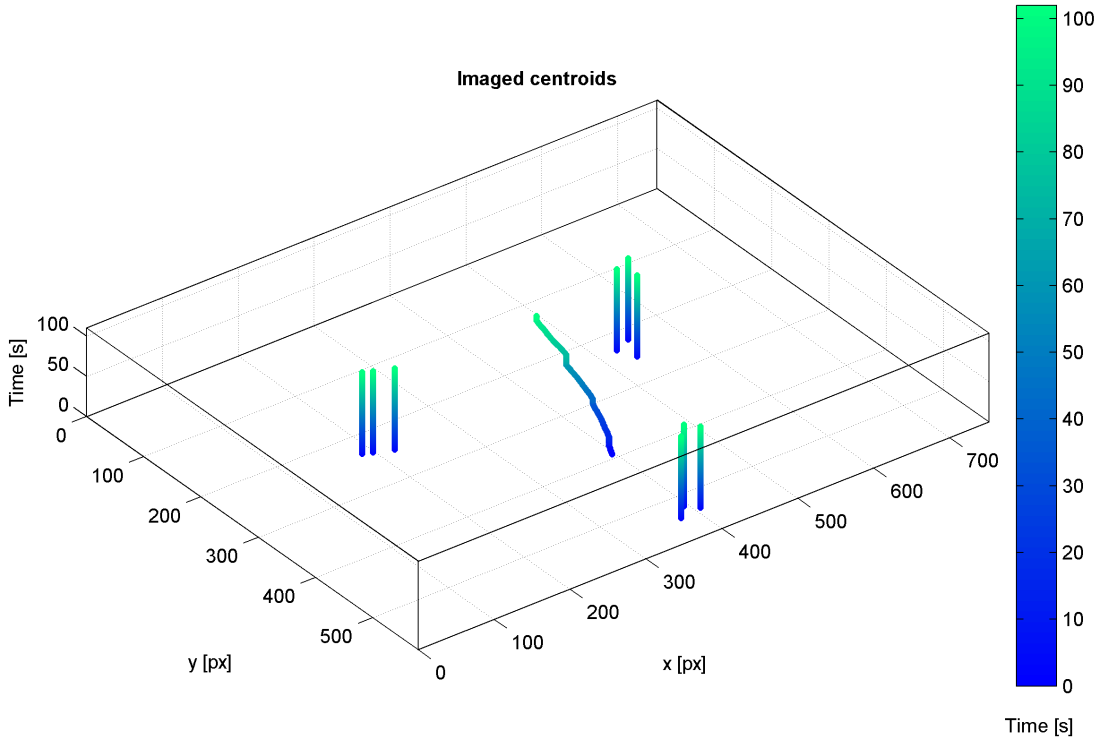

Figure 5.12: Temporal evolution of the visible centroids. The target can be seen moving within the field of view, whereas the constellations remain fixed.

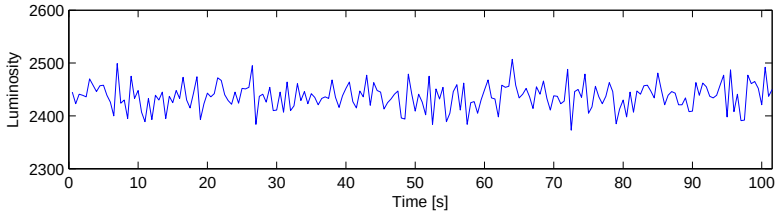

Figure 5.13: Target centroid's luminous intensity along motion.

centroid is plotted along motion together with an overlapped red marker indicating a positive VBS target lock at each acquisition. Figure 5.16 provides further information by plotting both the target lock flag and the estimated target angular velocity. By design, the VBS starts locking on the target after a few iterations and continuously maintains it along motion, until the velocity drops below the filter minimum threshold. Sparse events with vanishing centroid can be seen, but they have no influence on the tracking. It is worth noting the close match between the estimated target mean angular velocity 190.888 ”/s and the theoretical one 187.513 ”/s (from

Update period (ASC and VBS) [s]	0.5
VBS velocity filters range [”/s]	100–300
Motors travel range [μm]	200
Motors speed [μm/s]	5

Table 5.4: Configuration parameters for Pharos VBS verification.

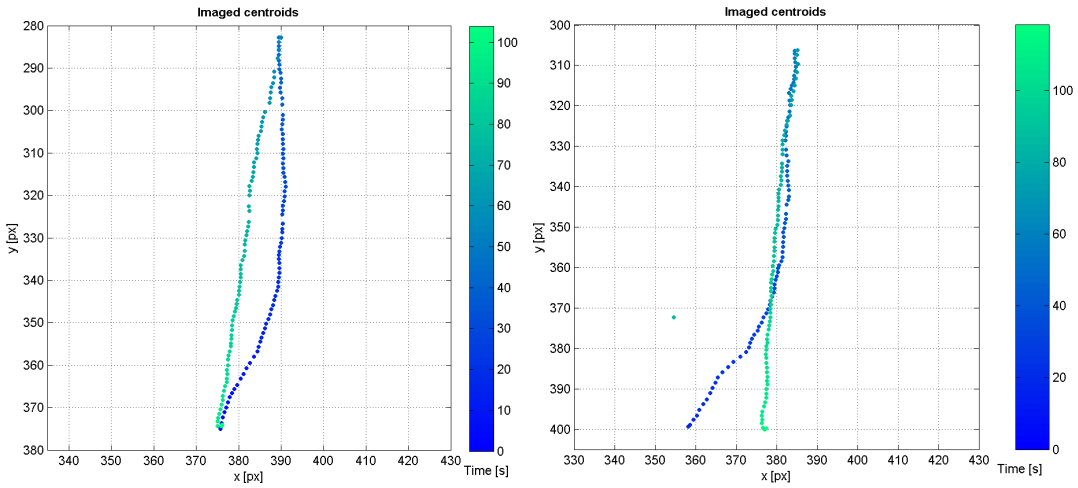

(a) (b)

Figure 5.14: Imaged target centroid for test P2tF02. (a) P2tF02a: motors above spring. Histheresis present, target returns to starting point. (b) P2tF02b: motors below spring. The target is considerably shifted during the forward motion when the motors are pushing.

Equation 5.9). The VBS reported FR mode along the whole test, as expected.

5.2.4 PRISMA VBS Verification

The verification of the VBS rendezvous algorithms has seen Pharos directly employed in the FAR (flight acceptance review) campaign of tests performed on the PRISMA satellites. These tests have taken place at the OHB Sweden (at the time SSC) clean room facility in Solna (SE). At that time, Pharos had been developed up to a preliminary v2 where the actuators' feedback had not been implemented yet. All the verification efforts are included in the official report (Massaro et al., 2009). This section will document the procedures and results specifically related to Pharos, aimed at verifying the following: FR mode, IR mode, FR-IR/IR-FR mode switching.

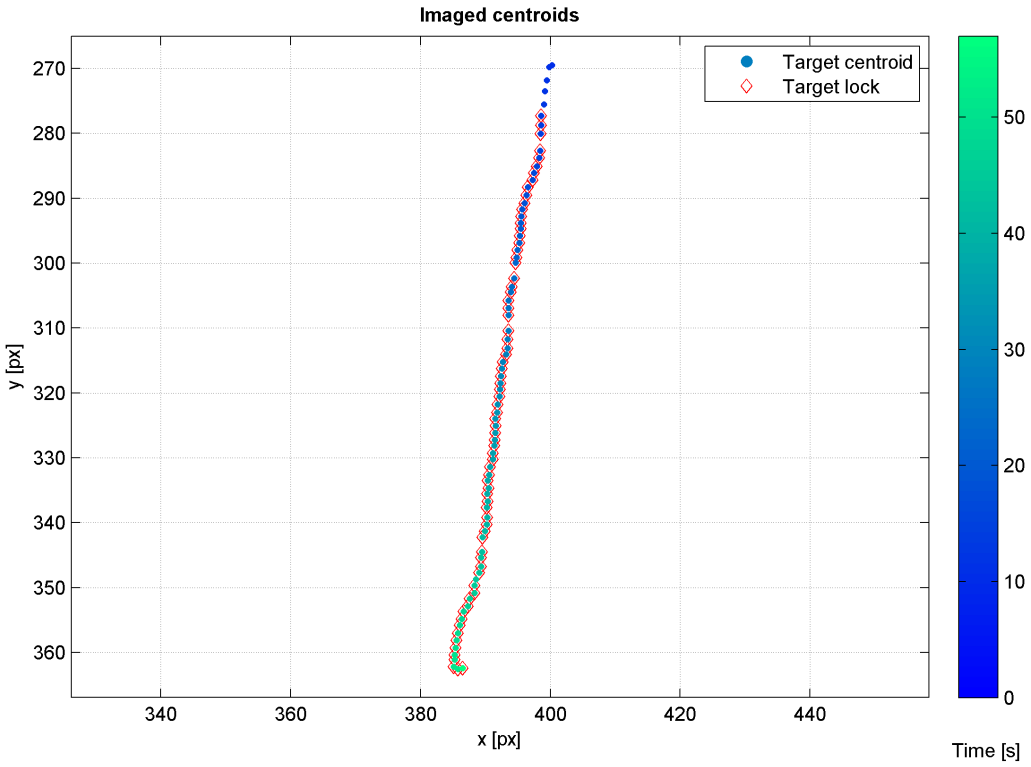

Figure 5.15: VBS FR tracking verification results P2tF03. The target centroid is tracked continuously for moving within the velocity filters. A positive lock is highlighted by a red marker.

The data has been extracted from telemetry files acquired from the SSC data center.

The module needs to be physically interfaced with the flight systems, therefore a customized interface plate is used to attach it to the camera baffle (Figure 5.17). The procedure involves ensuring proper alignment, connecting all power supply and communication cables and verifying on EGSE that the nine stars and target are visible to the ASC. A picture of the assembly is shown in Figure 5.18.

PHASE 1: Far range target lock

The software initialization procedure begins as usual with a star catalogue update and the definition of the velocity filters. Target speed was set at an equivalent of about 800 ”/s and the filters between 600 and 1000 ”/s. Erratic motion of the target, caused by the open loop motor drive, resulted in sporadic target lock between the time intervals 4900–4950 s and 5010–5050 s. During the central period, the target was out of the FOV, thus no data was retrieved. VBS mode classification is reported

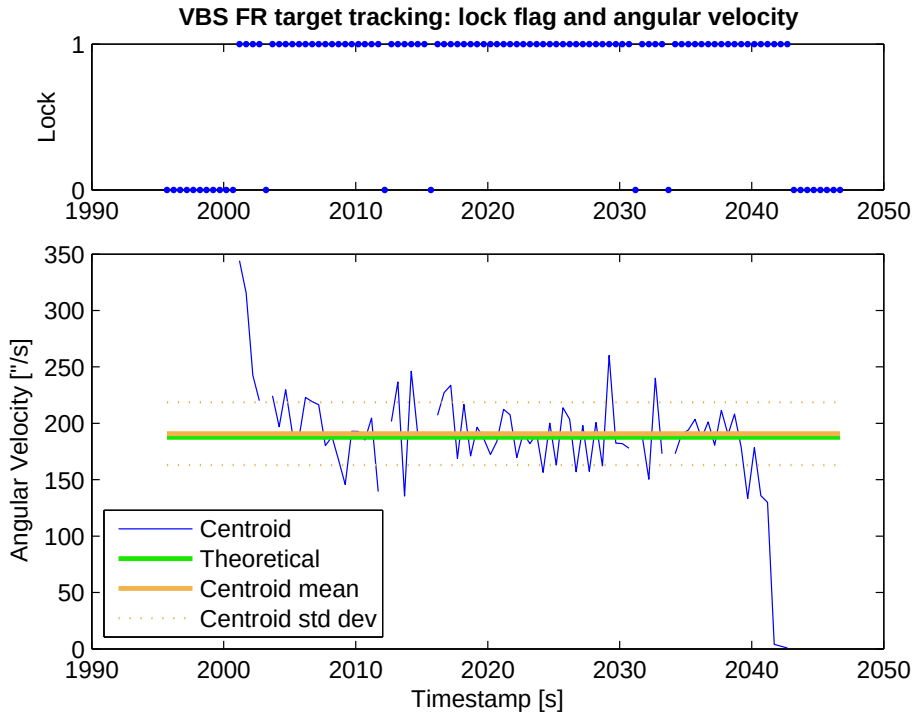

Figure 5.16: VBS FR tracking verification results P2tF03. (above) The target lock flag is valid when the target is moving. (below) Estimated target angular velocity during lock. The centroid mean velocity is measured at 190.888 "/s against the theoretical 187.513 "/s.

on three values: 0 (FR), 1 (IR) and 2 (SR). The mode was constantly 0 (FR) and the test was considered successful.

PHASE 2: Intermediate range mode

Intermediate range mode was verified by turning off the stars and checking that the VBS settled to IR mode while the target was the only object visible. The software is also expected to lock on it and provide a valid absolute direction (RA and DEC) in the virtual firmament coordinate system. This can be seen in the snapshot on Figure 5.20. The values of $RA \approx 0$ and $DEC \approx 90$ degrees correspond roughly to the target in the middle of the constellations, as expected. The mode was constantly 1 (IR) and the test was considered successful.

PHASE 3: Mode transitions

FR-IR and IR-FR mode switching have been tested by starting from FR mode and increasing the target brightness so as to overbloom the camera and trigger the

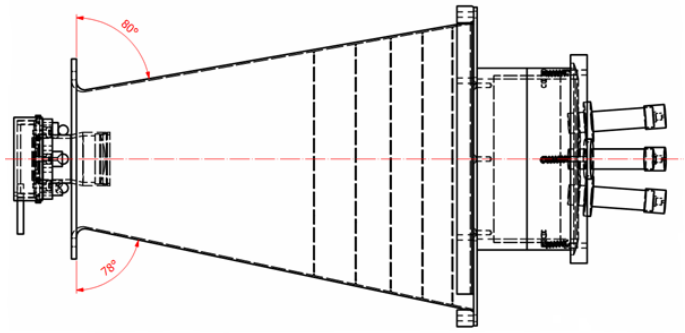

Figure 5.17: Pharos baffle assembly drawing for interfacing with the PRISMA flight system. Source: Measurement and Instrumentation Systems (DTU Space).

transition. The attempt has not been successful, despite an examination of the camera output showed a bright object at the center of the image (Figure 5.22). Instead, the mode transition has been verified by alternate on/off switching of the stars. A data sample is shown in Figure 5.21. The plots show values of RA and DEC differing from one mode to the other. This shift is due to the fact that in IR mode, the camera naturally loses track of the firmament, thus calculates the target direction relative to the camera's own coordinate system. Acknowledging this factor, the values of RA and DEC are correct.

Two consecutive null outputs can be observed at the IR to FR transition at 6456 s. This is a VBS feature as the target has to go through the FR filters and be tracked for at least three consecutive snapshots before being approved.

The mode transition was consistent in both directions and the test was considered successful.

5.3 SUMMARY

Pharos is the result of an integrated opto-electro-mechanical design aimed at simulating a movable luminous object within a background firmament. Work has covered all phases from concept to development and testing, including verification of the PRISMA far range algorithms. The module has shown the feasibility of implementing this functionality on a compact starfield stimulator, without interfering with the basic features, coupled with low power demands and simplicity of use.

During the tests, the need for additional functionality has emerged, like improving over the target brightness control for mode switching, or implementing a moving starfield. These changes require major modifications of the design and are left to future work.

Pharos is now also being used as a scene simulator for tuning algorithms for

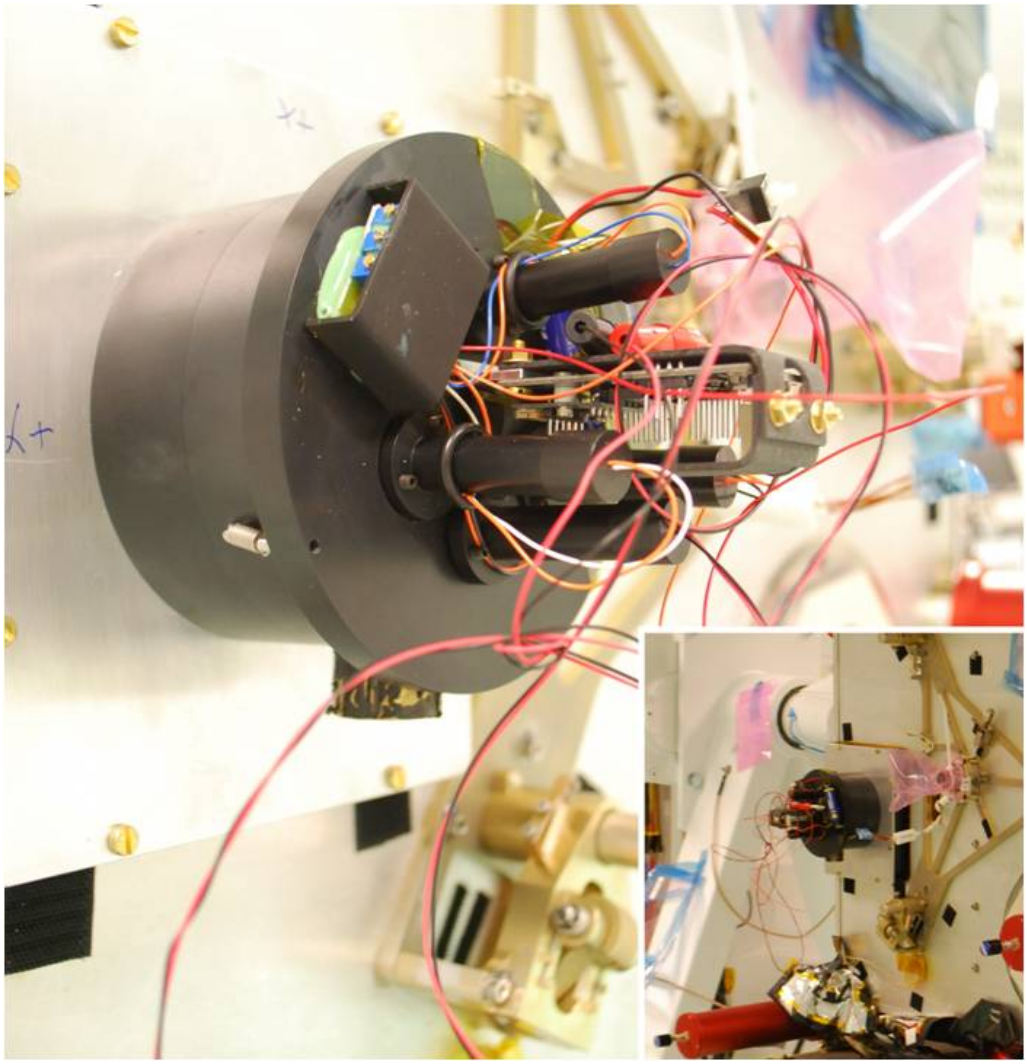

Figure 5.18: Pharos module attached on PRISMA for VBS verification at the OHB Sweden clean room facility.

asteroid detection. This capability is installed on the Juno spacecraft, currently traversing the asteroid belt, on its way to Jupiter.

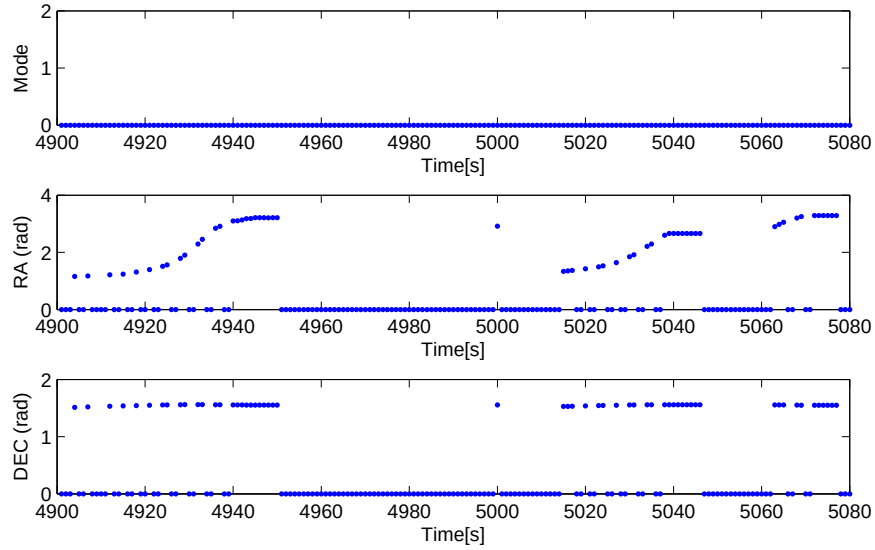

Figure 5.19: FR target lock verification on the PRISMA flight satellite.

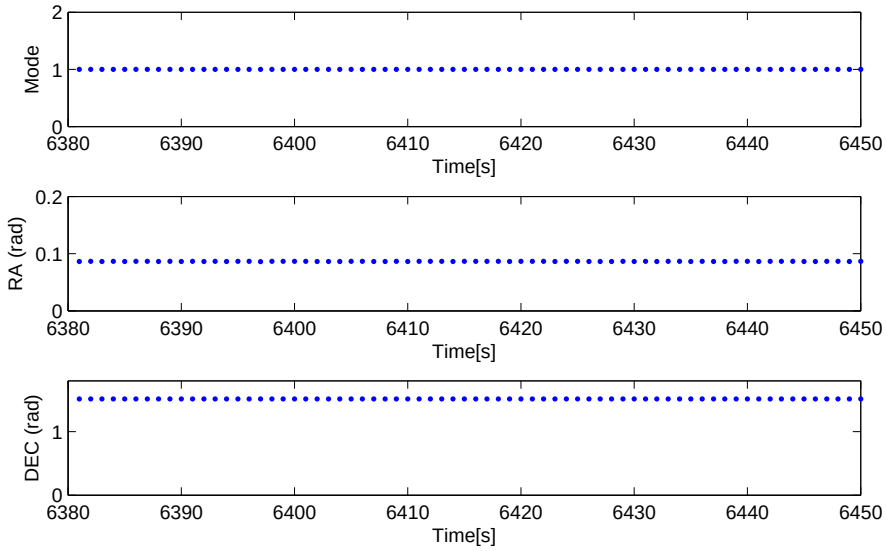

Figure 5.20: IR mode verification on the PRISMA flight satellite.

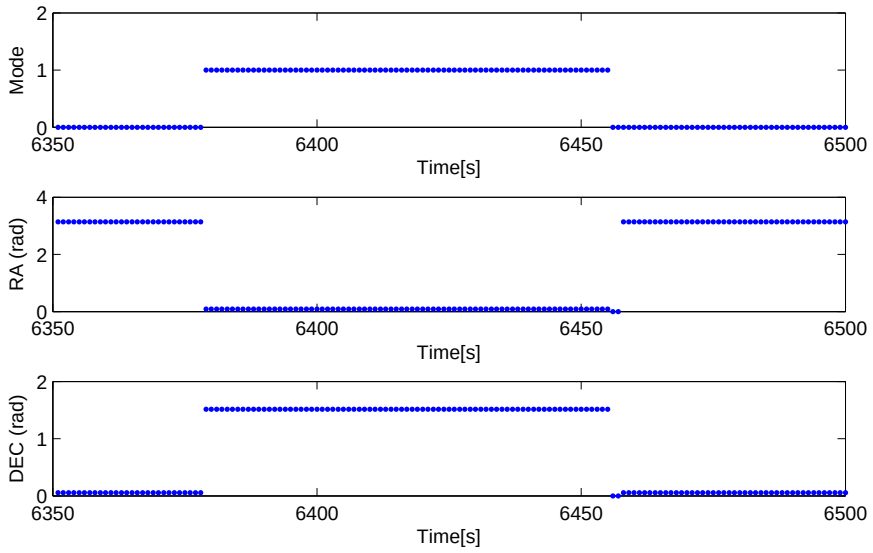

Figure 5.21: Mode transition verification on the PRISMA flight satellite.

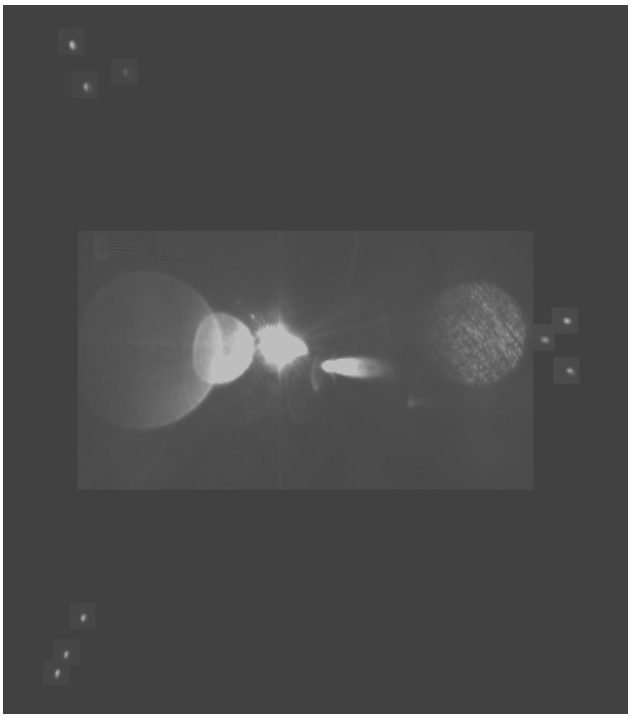

Figure 5.22: Overblooming test for stimulating a FR to IR mode transition. Image cropped and desaturated for print.

CHAPTER 6

Vision Based Sensors Verification and Validation Facility

This chapter describes the study, design and construction of the DTU Space optical test laboratory. The facility is now used for simulating the conditions in which the spacecraft will operate and provide more reliable tools for calibration of the vision based navigation sensors and verification of new technologies, so as to gain the highest possible confidence in the sensors' measurements before launch and in-flight operation.

Different procedures are used by engineers in order to achieve the required technology readiness level of a new instrument and ensure compliance with the defined specifications. Verification and validation are the "terms referring to the process of obtaining confidence by physical testing, analysis and simulation". The quote and the following definitions are taken from Fehse (2003).

- *Verification* is the proof that an item, function or process performs according to the specification, under which it has been developed.
- *Validation* is the proof that an item, function or process will behave as expected under real world conditions.

For space-borne systems, there are limits to what can be achieved in ground testing, as the dynamics of free fall flight, as well as the photometric conditions, are difficult to replicate to the full extent in a laboratory. Solutions for the positioning of sensors and target models have evolved along the years, from the complex gantry

structures used, for example, in the early Space Shuttle and MIR programs. Advances in the development of complex control and actuation components, now allow reducing some of the constraints and give more flexibility over the trajectories to be reproduced.

The chapter starts by outlining the identified requirements and environmental constraints for the construction of an optical test laboratory, meant to support the verification and validation of the vision based sensors developed at DTU Space (Figure 6.1). Thereafter, the final facility layout is described and the design and selection of the key elements of the laboratory is documented. My contribution on this work has covered all aspects, from concept to design and finally system integration.

The objective of the facility is to provide an environment that mimics the illumination conditions of the specified mission scenarios, and include precise sensor manipulators for replicating the expected trajectories in full - or reduced - scale. No information flows between the control systems and the sensor, thus the tests will run in open loop. The possibility of a future development including active mathematical models of the missing components and/or environmental effects, operated within an integrated AOCS system is not excluded for the future. The scope ranges from rendezvous and docking (RVD) and formation flight (FF) to precision planetary landing (PPL) and surface navigation. The development of the laboratory is grounded upon the experience gained during the verification and calibration of the VBS technology for the PRISMA satellites. This location will be the center for future development and ground testing of sensors for many missions to come.

6.1 REQUIREMENTS

Various instrumentation and equipment are required to reproduce a faithful approximation of every test scenario. This section focuses on the primary requirements needed to achieve the goal. A mission profile analysis can help in outlining each functional area and its related components. Table 6.1 collects the results of the preliminary investigation relative to the work that will be described in this chapter. The mission profiles of interest for this work can be classified in four main groups, despite some of them having many similarities: planetary roving, planetary landing, rendezvous and docking, formation flight.

Roving and landing apply techniques of robotic navigation focused on hazard detection and avoidance and terrain relative pose and position determination. They both require a representative physical terrain landscape, though their dynamics are considerably different. As the rover will be bound on ground, instead of flying, the sensors have to be mounted on a mobile vehicle. A lander, on the other hand, may require up to six free degrees of freedom (DOF) for replicating the orbital and landing translational and rotational trajectories, eventually including disturbances. The

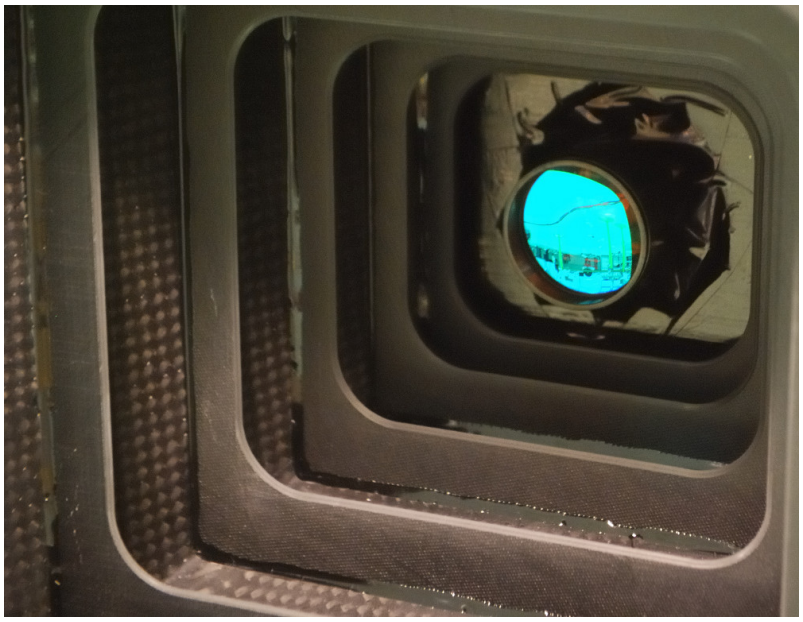

Figure 6.1: Closeup of the VBS short range "blue eye" camera.

Mission Profile	Requirements				
	Star Firmament	DOF	Terrain Simulation	Illumination	Camera Setup
Roving	No	Vehicle mounted	Yes	Sun & Diffuse	Stereo & Panoramic
PPL	Yes/No	6	Yes	Sun & Diffuse	Mono/Stereo
RVD	Yes (FR)	9	No	Sun & Secondary	FR/SR
Formation	Yes	9	No	Sun & Secondary	FR/SR

Table 6.1: Summary of the preliminary requirements investigation.

camera setup will have different configurations, depending on the specific test. Some examples can be: stereo vision for fast terrain mapping, or mono vision for landing attitude determination, potentially in coordination with a star camera. The use of star cameras in the facility will be restricted to simulated star fields. Illumination of the scene plays a big role in vision based systems and a complete lighting setup has to include a main Sun light and eventually a diffuse light (e.g. atmospheric scattering).

A different case is made for space flight missions like RVD and FF. Along their orbits, the spacecrafts perform all sorts of manoeuvres and will be free to rotate about all axes. Adding relative translations, a pair of satellites can have up to nine degrees of freedom. A star firmament is required when estimating the spacecrafts' attitudes relative to the inertial reference frame. The star field will naturally have to be simulated for indoor tests. Lighting includes again a main Sun light and a secondary light (e.g. the day-side illumination of the host planet). There may be cases in which the planet is required in the field of view, therefore a specific optical arrangement should be made. An obvious camera setup is a VBS class system, with a proper combination of short and far range camera heads.

Additional sensors can be part of the system for determining pose and position and performing photometric analysis. True relative and absolute (within the lab) pose and position of the sensors and targets can be determined with different methods. The readings shall be used to evaluate the quality of the estimates. Photometric instruments, such as VIS/NIR (visual/near-infrared) spectrometer and luxmeter, can be used to quantify the illumination and reach a more realistic approximation of the scene, as well as allow for more accurate parameters tuning.

The trajectories executed by sensors and targets during the verification tests, have to reproduce key moments of the flight manoeuvres. These may require, as mentioned above, a whole suite of manipulators giving up to nine DOF distributed between the two bodies. Nonetheless, since most of the experiments can be split in sub-phases and the constraints of a physical manipulation system cannot be overtaken (see Section 6.2.2), a compromise is needed.

The remaining requirements are in relation to the functional arrangement of the laboratory. The ideal placement should maintain a test area, where the operations are performed, isolated by the control area, where the user and the control systems are located. The test area should be optically isolated, so as to prevent external lighting to interfere with the scene illumination. More details are provided in Section 6.3. Finally, the facility has to include all interfaces for control and supervision of the machines and all the necessary generic installations, such as: power, data network and lighting.

6.2 ENVIRONMENTAL CONSTRAINTS

The location selected for erecting the facility is an underground room of 9.4×6.5×3.4 m (l×w×h) in the precincts of the DTU Space department. The constraints of this solution are hereby grouped by subject and described below.

6.2.1 A Matter of Size

Reproducing large scale scenarios, such as the ones this book focuses on, certainly dictates some boundary conditions. Spacecraft rendezvous covers distances ranging from tens or hundreds of kilometres, all the way down to a few meters during the final approach phase. The same range order of magnitude applies to precision planetary landing (PPL) missions where vast surfaces make up the scene from low orbit until touchdown. A different case can be made for deep space navigation, lying on a whole different scale. Finally, formation flight can be placed midway at some few hundred metres, as this is the range where this mission class has the potential to outplay long boom designs. Hence, a physical laboratory setup must be scaled down to a more manageable size. A good example is given by the SFS and Pharos stimulator modules discussed in Chapter 5, which are able to recreate an accurate representation of a star firmament and a distant moving target. Despite the artificial stars, a star camera interfaced with these modules will still provide valid telemetry. When real world conditions are needed, for example in real sky tests, outdoor setups will be favoured. For all other tests proving too complex for a physical reconstruction, virtual 3D modelling (discussed in another chapter, Section 3.7) may then come in handy for its flexibility, albeit at the cost of photometric accuracy. The laboratory has been designed for running separate and independent tests for the individual operating modes (e.g. short range, far range, etc.) at full scale, when possible, or scaled down. This means that for both RVD and PPL, scaled down models are needed and the resolution of the modelled features - whether spacecraft or terrain - should be coherent with the scale factor.

Lastly a few remarks about an element which plays an important role in remote sensing and in particular photometry: air. Air is most welcome in any living environment, though its presence as intermediate medium in an optical lab, introduces measurement noise. Light absorption and refraction grow larger with the distance between sensors and targets, as does turbulence, making the deployment of large scale tests for accurate calibration undesirable. For the purpose of ground based verification, the presence of air cannot be spared, as investing in a full scale vacuum chamber is unreasonable. Yet, the location of the laboratory offers a relatively still environment in which to measure.

6.2.2 Physical Limitations

With all the models physically bound to the various manipulators and not freely floating in space, the trajectories achievable are constrained by the kinematics and dynamics of the manipulators. Aside from the geometrical boundaries on translation and rotation, the setup also limits the ranges of velocity and acceleration.

Attitude adjustments occurring during flight can be frequent and sudden, and may trigger unexpected behaviours on the sensors and navigation system. The

inclusion of thrusters, or equivalent stimuli, in the verification process may be useful for characterizing the effect of continuous or pulsed bursts on the algorithms. Means for implementing this kind of tests should be investigated.

6.2.3 Scene Lighting and background

Lighting conditions in an open space environment can vary significantly, from total darkness to full Sun light. The Sun is the dominating light source in the scene, acting both directly and indirectly when reflected by other bodies' surfaces. The result is that even locally and at the same point in time, huge contrasts can be present and have to be dealt with by the optical systems. Alongside, large planetary bodies and small local objects may provide secondary illumination. As the latter sources are easy to emulate, the design challenge is to provide a parallel beamed light source emulating the large distance Sun, within the little room available.

Depending on the location within the solar system, the average full spectrum electromagnetic radiation arriving from the Sun can vary, for example from the 1360 W/m^2 in the vicinity of the Earth to the 600 W/m^2 around Mars, and can be approximated by Planck's law of black body radiator. The actual spectral band of importance for the vision based sensors falls within the visual and near infrared band. As artificial lamps have different spectral distributions than a black body, approximations have to be used. For example, testing extreme effects, such as blooming, can be achieved by adjusting the camera integration time. Diffuse lighting, like the one stemming from atmospheric scattering, can be simulated with standard lighting setups.

6.3 FACILITY LAYOUT

The location identified for hosting the facility is an underground room with a floor surface of 9.4×6.5 m. Most of the surface is dedicated to this scope, except for an area of about 3×3 m, dedicated to equipment for magnetometry experiments. The final layout is sketched in Figure 6.2. Three main areas highlighted: test, control and storage. The test area occupies the far end of the room over the long side, so as to offer the longest dimension for the approach and recede motion. This is where all manipulators are located and the area is isolated by a full light-blocking curtain running from side to side and from floor to ceiling. The area also hosts the illumination system and the planetary terrain. Most systems have been designed to be modular, in order to be flexible and easy to re-deploy for the different experiments, as described in the following sections.

The control area includes the laboratory's control station and data acquisition, telemetry and processing machines. This is where all the trajectories are pro-

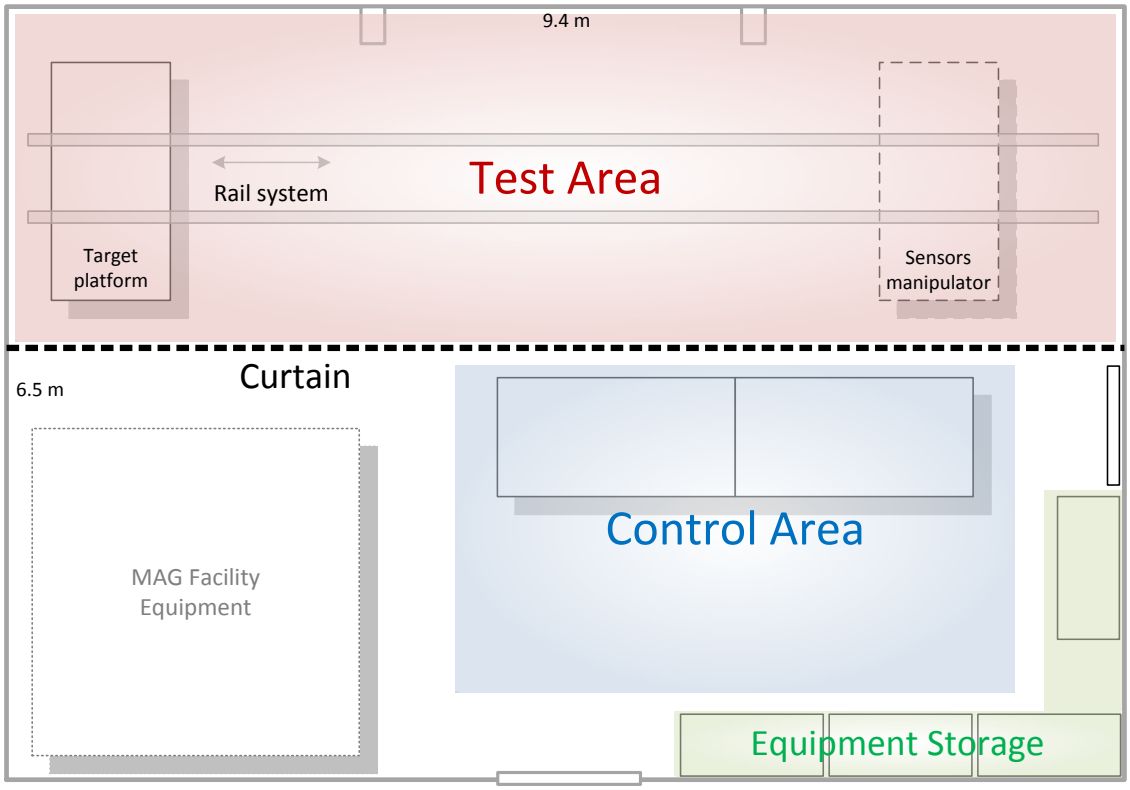

Figure 6.2: Test facility layout.

grammed and the manipulators are operated. All other sensors, tools and equipment necessary for running the show are stored in adjacent lockers.

6.4 SENSORS AND TARGET MANIPULATION

Following from the analysis of Section 6.1, the chapter continues with a detailed design of the facility components. A distinction is made between the sensors manipulator and the target platform (see Figure 6.2). In a typical setup, the sensors are mounted on a multi-axes manipulator, with up to six degrees of freedom. On the other end, a fixed platform hosts the target model. Target handling is discussed in Section 6.4.3.

For increased flexibility, the equipment enables for the sensor and target platforms to be swapped. This may be the case for scaled down RVD/FF tests, where the smaller sized target can be attached to the multi-axes manipulator.

Because under the majority of test scenarios the kinematics will be restricted to relative motions (spacecraft vs target), the degrees of freedom defined above can be distributed between the two platforms. This means, for example, that translations

Rotation range [deg]	>360
Backlash [μrad]	200
Repeatability [μrad]	50
Max velocity [deg/s]	90
Axial force [N]	550
Max torque [Nm]	$\pm$6
Mass [kg]	1.88

Table 6.2: Features list of the PI M-061.PD rotation stage.

can be applied only on one of the platforms. In flight, the camera setup will be located on the main spacecraft, which will be equipped with all the guidance, navigation and control systems. Therefore it is reasonable to implement up to 6 DOF to the sensor platform. This shall include 3 axes translation and 3 axes rotation. The remaining rotations are left to the fixed platform.

Depending on the required trajectory of each test, different manipulators can be employed. During this study, two solutions have been investigated: a yaw-pitch-roll (YPR) setup and a robotic arm. The YPR setup is based on three orthogonally mounted turntables. They are highly accurate, stable and reliable. This solution is appropriate for a simple rotational setup, though it would entail considerable costs and complexity for implementing additional linear positioning rails.

The favoured robotic manipulator solution can provide up to 6 DOF and a much higher flexibility in replicating the orbital trajectories and is favoured for use as multi-axes manipulator. These two setups are described in the following sections.

6.4.1 Yaw-Pitch-Roll Setup

The use of rotary tables for various testing purposes is very diffuse in testing and calibration of measuring instrumentation. A properly designed machine can provide a stable, controllable and predictable motion, ideally to the point where its presence becomes unnoticeable. The high accuracy and sensitivity of the sensors developed at DTU Space demands comparable performance levels, therefore I have probed the market for such a device, and found the PI (Physik Instrumente) precision rotation stage. This device is equipped with double row ball bearing, preloaded worm gear transmission and high resolution servo motor control. The result is a very accurate and stable continuous rotation stage. The main features are listed in Table 6.2, relative to the M-061.PD model which has a 100 mm diameter plate and PWM controlled servo drive (Figure 6.3).

The tables performance has been verified by the ASC team during a real sky test, where a DTU Space stellar compass was spun, directed at the sky, with a

Figure 6.3: PI M-061.PD precision rotation stage. Picture source: *www.physik-instrumente.com*

periodic oscillatory motion. Analysis of the collected attitude data has shown results consistent with the programmed motion profile. The results have been included in Appendix C.

Based on those results, the device is now used by the Department for testing various optical benches at in house or remote locations. Driven by the need of providing additional rotational degrees of freedom, I have developed an extended design which includes three orthogonal rotation stages, as in Figure 6.4. The assembly is combined by L shaped aluminium plates, dimensioned such that the camera's optical center is crossed by all three rotational axes. This prevents translation effects and allows testing solely the effects of rotations. The minimum estimated travel ranges for axes 1, 2 and 3 (from the base to the camera) are: ± 180, $+180/-45$, ± 180. These are calculated from the starting position of Figure 6.4, following the right hand screw rule for the positive sign, and are dependant on the camera field of view and cables flexibility. To reduce the amount of parts and improve portability, the assembly can be powered by a single supply line through a specially designed power box. The tables can be controlled via PC (USB or RS232) and programmed for autonomous operation.

6.4.2 Robotic Arm Setup

The YPR setup is an accurate and flexible solution. It can be programmed easily, thanks to a versatile macro architecture and language provided by the manufacturer. Nonetheless, this solution has various shortcomings. The reproducible motions are constrained to three rotational DOF. Each rotation is dissociated from the other, since each stage has its individual controller, therefore the programming quickly increases in complexity, as the operator is required to derive each individual motion resulting in the desired combined motion.

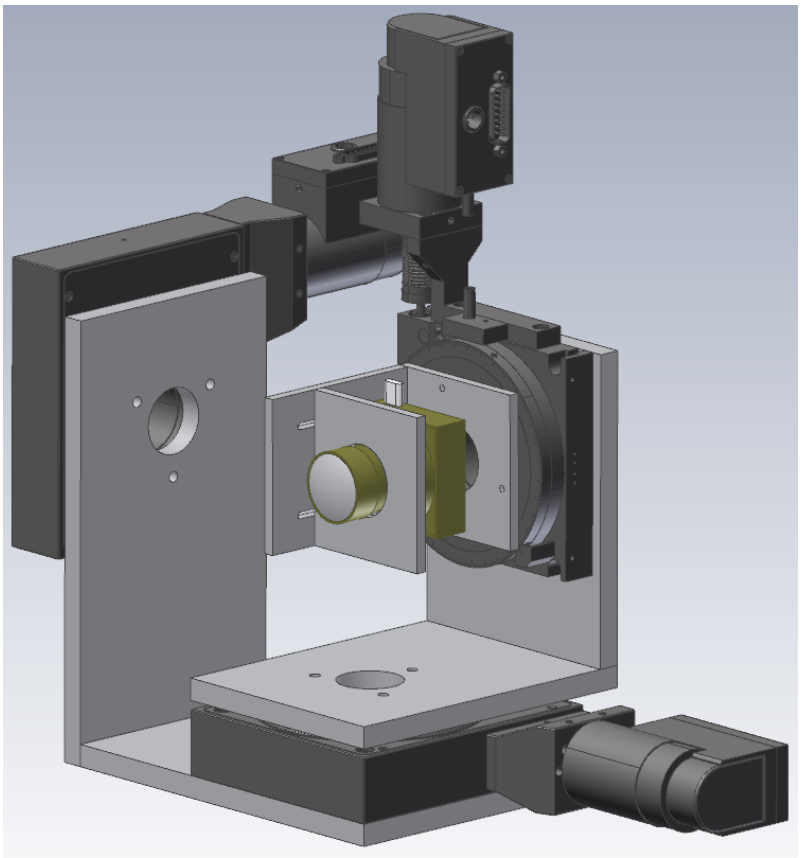

Figure 6.4: 3D drawing of the yaw-pitch-roll assembly for 3 axes sensor manipulation.

Industrial robotic manipulators have developed steadily and as performance increased, costs have been reduced, thanks to larger scale productions and standardized designs. Robotic arms provide better flexibility and dexterity than combined linear and rotational stages. A six axes arm can move objects with six degrees of freedom, within the volume allowed by its arms and joints. All this from a single controller, that can be operated remotely or with a transportable hand-held interface, typically referred to as pendant. Trajectories can be programmed (or taught) with code or by manually handling the arm's wrist. A sequence of transit points can be defined during teaching, after which the robot will automatically interpolate between them and memorize the path.

Table 6.3 includes a feature comparison of two candidate solutions in the same category, produced by the two market leaders. The criteria for selecting these models have been: size, weight, repeatability and control. Despite both models being comparable on most parameters, the KUKA stands out for its considerably lower

	ABB IRB140	KUKA KR5 sixx
Axes	6	6
Weight [kg]	98	29
Pose repeatability [mm]	±0.03	±0.03
Max. payload [kg]	6	5
Max. reach [m]	0.8	0.85
Pendant pad control	Yes	Yes
PC interface	Yes (Ethernet)	Yes (Ethernet)

Table 6.3: Feature comparison of two robotic arms.

weight. The fine repeatability and payload capacity of the KUKA KR 5 sixx (Figure 6.5), make this robot a valid solution for sensor manipulation.

The robot is mounted on a moving platform, on which it applies forces and moments. From the datasheet, the expected maximum moment applied on the mounting plate is about 1000 Nm. This value is critical in defining a proper rail guide, as described in the next section.

6.4.3 Target Platform

On the far end of the test area is located the target platform (Figure 6.2). Here is where the target spacecraft model is located. The area is therefore arranged with manipulators complementary to the rest of the facility, allowing additional freedom of movement. Translation drives have not been considered in this segment, as the design has been developed around the robotic arm solution, which is integrated on a main transport rail. Currently, the platform consists of a heavy load rotation table with virtually unlimited rotation range and speed from 0.1 to 12 rpm. The LT360 table (Figure 6.6) bearing system has been redesigned in house in order to improve its flatness with a special double conical bearing.

The target platform can also be used, as discussed above, to host the 3 axes yaw-pitch-roll setup for camera or other scaled down models depending on the test. In this case, the assembly can be mounted on a tripod for easier positioning without sacrificing stability.

6.5 ORBIT RAIL

A transport system is needed for two reasons: to support the sensors manipulators and to give them the required translational degrees of freedom. The purpose is to allow the drawing of trajectories for direct approach and recede tests and of

(a) (b)

Figure 6.5: The KUKA *KR 5 sixx* robotic arm with controller and control pendant. Pictures source: *www.kuka-robotics.com*.

Figure 6.6: LinearX LT360 rotation table. Picture source: *www.linearx.com*

planetary flyby and landing. A list of requirements can be laid out, in consideration of the investigation documented so far.

- 9 m stroke
- 0.4 m/s max speed
- Overhead mount
- Sub millimetre positioning accuracy and repeatability
- High stiffness for a maximum load of 50 kg and moment up to 1000 Nm

A simple, precise and effective system to transport equipment is railing. The rail can make use of the room's full length and, allowing for some tolerance, it can extend up to 9 m. I have chosen to place the whole transportation system overhead to give more freedom of movement in the lab and allow more room for setting and arranging the artificial terrain and other future setups on the ground. As rendezvous manoeuvres are notoriously slow (Fehse, 2003) and planetary landing manoeuvres will be scaled down, the rail linear velocity requirement is quite relaxed. A velocity of 0.4 m/s is therefore considered a reasonable top limit.

Instead, high accuracy and repeatability are desirable. These properties are important for the reproducibility of the verification and calibration data collected. Section 6.5.1 covers the design of the rail actuation and positioning system. Stiffness of the mechanical structures plays also a big role in this sense. Mechanical deformations cannot be avoided, but the structure should be designed so as to minimise them. For this reason the stiffness requirements, in terms of maximum applied forces and moments, have been dictated by the worst case load conditions induced by the class of robotic arm surveyed for the task and the expected payloads. Section 6.5.2 covers the design of the overhead rail support structure.

The study started with a simple solution to be developed ground up:

1. select a guide rail,
2. apply a closed loop motion system,
3. mount all against the ceiling.

Given the complexity of the system, only a fully fledged industrial class motion system would guarantee coverage of the requirements. From here on this section documents the orbit rail design.

The linear motion systems available on market are divided in different categories, depending on the application requirements. Table 6.4 summarizes the key features of each category and opens up to the selection of a valid candidate. The main selection criteria that define the performance features are drive and guide type.

The drive types available on market are: screw, belt (Figure 6.7) and wheel. Screw types are known for offering the highest repeatability in exchange for limited speed range and higher cost. Belt types provide better response for high speed and

Category		Feature			
Drive	Guide	Repeatability	Stiffness	Speed	Cost
Screw	Ball	High	High	Low	High
	Slide	Medium	Low	Low	Medium
Belt	Ball	Medium	High	High	Medium
	Slide	Medium	Low	High	Medium
	Wheel	Medium	Medium	High	Medium
Wheel	Wheel	Medium	Medium	High	Low

Table 6.4: Linear motion technologies feature comparison. The assessment shown here is the outcome of my survey over various manufacturers and models.

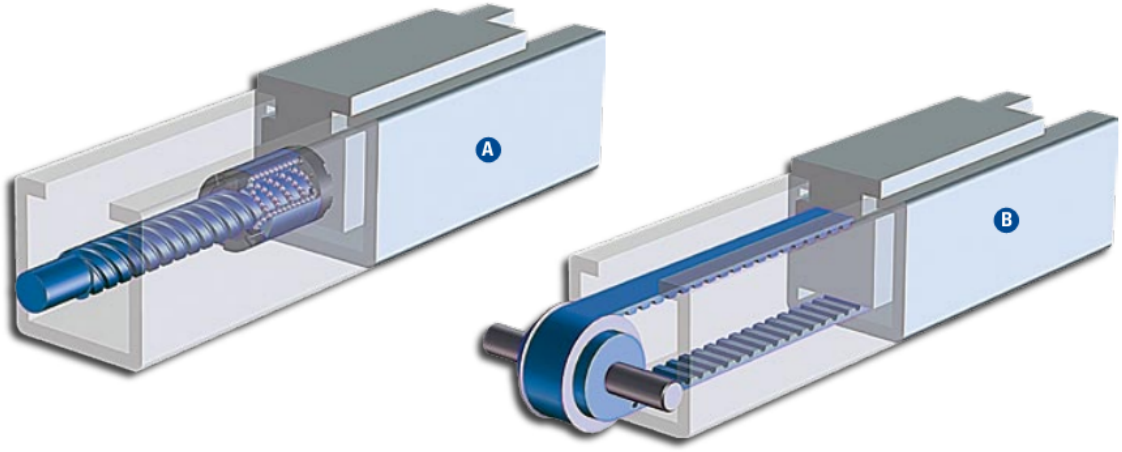

Figure 6.7: The most common linear drive techniques are ball screw (A) and belt (B). Screws offer higher repeatability and thrust at the cost of speed and weight. Drawing source: *www.thomsonlinear.com*.

accelerations but lesser repeatability compared to screws. This stems from elastic and backlash effects of the belt-cog design. In wheel drives the thrust is applied by the wheel directly on the profiled support. Performances are in the average range, though the need to place the motor on the moving platform can transfer unwanted vibrations to the measuring system it is moving with. Despite screw drive can lead to the best performance, a full size screw of the required length cannot be physically brought into the basement room (assembling is also not possible for the surveyed manufacturers), therefore it has been excluded from the options. Elastic belt effects are negligible at low speeds and accelerations, though the effect of backlash on repeatability has to be accounted for by calibration or other methods.

A guide system for accurate motion is typically made of a profiled high-carbon steel raceway supported by an extruded aluminium beam, that helps to reduce deflection under load. On market are available three guide types: ball bearing, slide, wheel bearing. Ball bearing guides offer best performance in terms of stiffness, accuracy and repeatability. Slides are not the most recommendable for dynamic operations due to unpredictable friction effects and wear. A standard sized wheel guide system can satisfy the requirements for the relatively small load, though it will not sustain the worst case moments applied by the robot arm solution unless a heavy duty model is used.

Few manufacturers provide a combined rail and drive system and in most cases these are limited to a few meters. As emerged from the market research, manufacturers offer substantially equivalent performances in the same price range, therefore the choice has been based on the design flexibility and local availability offered by the British Hepco Motion. Hepco rails can be assembled to bigger lengths and the integrated belt drive solutions are complete of motor interface. One such model is the Hepco SBD (Sealed Belt Drive), which offers a combination of caged linear ball bearing guides and high strength tooth belt drive in a sealed package, improving safety and cleanliness. A drawing of such a model is shown in Figure 6.8.

To find out whether the rail is able to sustain the estimated loads, we have to take a look at the manufacturer declared load capacities. The data extracted from the datasheet, relative to the long carriage option, is listed in Figure 6.9. The system is offered in two typical sizes: SBD20-80 and SBD30-100. While both can take very heavy force loads, neither option can tolerate the required 1000 Nm moment (about all three axes) exerted by the favoured small robotic arm solution. Both fall short on M_s. Facing this data, I have decided to build a dual SBD20-80 rail system, where the weaker moment capacity is distributed between two parallel beams. Structural rigidity will also benefit from this arrangement.

The Hepco SBD rail comes standard in lengths up to 6 m. Longer distances are possible with provided special assembly components. Given the 9 m design choice, and logistics constraints, the beams have been ordered in two pieces of about 4.5 m to be assembled in house.

According to the declared capacities, a single SBD rail cannot sustain the maximum torques exerted by a small robotic arm (circa 1000 Nm), therefore a dual rail solution has been brought along. Two rails can distribute loads and increase robustness and stiffness. Uniform thrust and alignment are ensured by a common drive shaft controlled by a single motor.

As none of the commercially available rails are self-supporting over long spans, an appropriate support structure is needed. This is discussed in Section 6.5.2, where the expected operational loads and induced deformation are analysed.

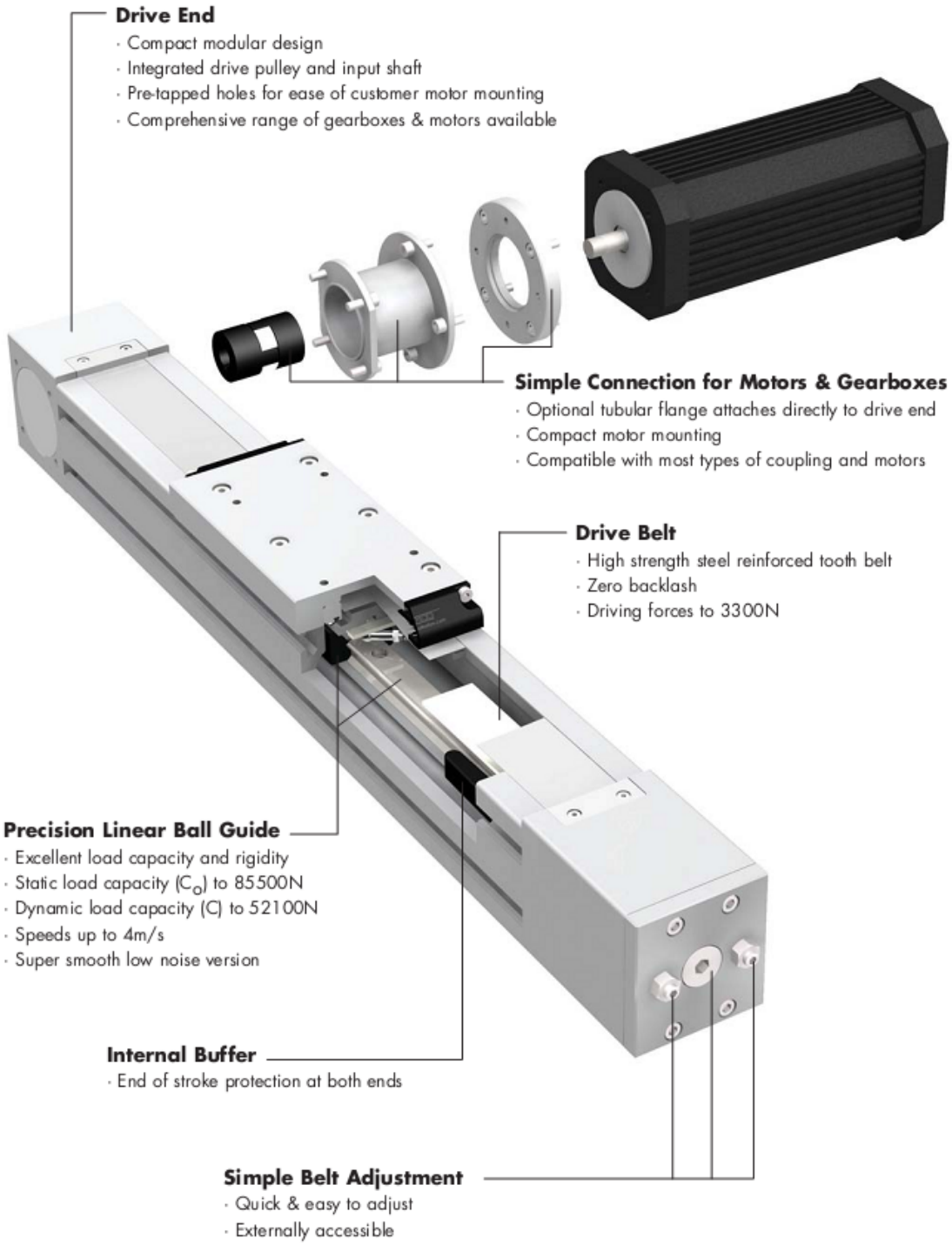

Figure 6.8: Hepco SBD (sealed belt drive) linear rail. Drawing source: Hepco SBD datasheet.

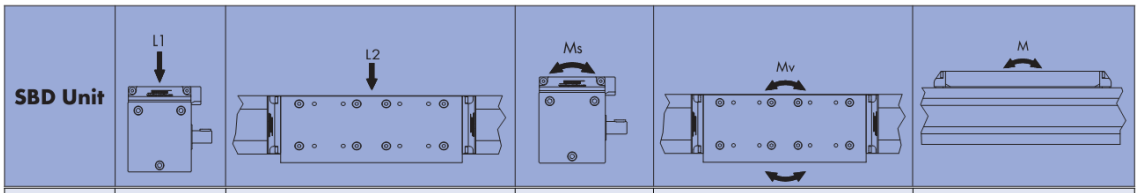

SBD20-80	33920N	33920N	302Nm	1611Nm	1150Nm
SBD30-100	68800N	68800N	848Nm	4214Nm	2990Nm

Figure 6.9: Hepco SBD (sealed belt drive) long carriage maximum load capacities. Data from the SBD datasheet.

6.5.1 Actuation and Positioning

The various shaft interface options of the SBD rail allow a good degree of flexibility in defining the actuation system. Various types of motors can be used to convert the shaft's rotary motion to linear carriage motion. For this project I have considered electric AC motors combined with gearbox, in order to achieve the desired torque and speed requirements. An important selection criterion relating to actuation, is the distinction between open and closed loop systems. For calibration and validation, it is necessary to obtain accurate positioning values, in order to have a secure reference to measure against. As open loop systems do not provide a feedback, confirming the motor's position, this category would not provide sufficient controllability over the system. A servo solution can technically satisfy all requirements. Servo motors provide accurate positioning feedback using sensors, such as encoders or resolvers. In addition, they have the option to be operated and supervised remotely with other systems, like a PC. The latter is a very desirable feature for the laboratory, because it allows real time supervision and telemetry logging.

The targeted servo solution is the Bonfiglioli Vectron (Figure 6.10). This product includes a servo motor with resolver feedback, inverter controller and an optional reduced-backlash planetary gearbox. A motor brake is not deemed necessary, as the cart will come to a halt immediately after power cut, due to friction effects and the low speeds involved.

The following is a numerical discussion of the motor parameters design. The physical quantities of interest are: velocity, acceleration and torque. All motor parameters have been selected in accordance to catalogue availability. Given an SBD belt pulley radius $r = 2.39$ cm and a chosen motor speed of 3000 rpm, the carriage top speed can be derived.

$$v_{@3000rpm} = 3000 \times \frac{2\pi r}{60} = 7.51 m/s \tag{6.1}$$

For a maximum carriage velocity of about 0.4 m/s, the motor requires a reducing gearbox. With a 20:1 ratio, the velocity will be:

$$v_{@3000rpm,20:1} = \frac{v_{@3000rpm}}{20} = 0.38m/s \tag{6.2}$$

Therefore, a 20:1 planetary gearbox is a fitting choice. The calculation of the worst case torque starts from an estimate of the expected forces applied to the belt and guide system. These are: rail friction ($F_{friction}$), thrust force (F_{thrust}, to impart kinetic energy to the load) and break away friction ($F_{b-a} = 29N$). The latter value is provided by Hepco, together with the rail friction coefficient $\mu = 0.01$. For a load mass $m = 50$ kg and acceleration $a = 0.3$ m/s^2 the total force to be applied is:

$$F_{total} = F_{friction} + F_{thrust} + F_{b-a} \tag{6.3}$$

$$F_{total} = \frac{m}{2}g\mu + \frac{m}{2}a + 2 \cdot 29N = 68N \tag{6.4}$$

The calculation considers the load equally distributed among the two rails. Multiplying this force by the pulley radius yields the motor torque load M.

$$M = F_{total} \cdot r = 1.62Nm \tag{6.5}$$

Evaluation of the actuator's positioning accuracy starts from the declared resolver angular accuracy, from datasheet, at ± 4 minutes of arc (about $\pm 1.164 \times 10^{-3}$ rad). This value can be translated to linear motion as follows. $r = 2.39$ cm is again the belt pulley radius.

$$\varepsilon = \pm 1.164 \times 10^{-3} r = \pm 27.809 \times 10^{-6} m \tag{6.6}$$

Which can be further reduced by the gearbox 20:1 reduction ratio.

$$\varepsilon = \frac{\pm 27.809 \times 10^{-6}}{20} = \pm 1.390 \times 10^{-6} m \tag{6.7}$$

This is the theoretical linear accuracy achievable by the servo motor and rail solution. In reality, undesirable effects such as backlash and elastic deformation, will result in additional bias. For example, the declared backlash of the two stages reduced-backlash gear included is 8 minutes of arc. No information is provided regarding the rail, since the guide is reportedly backlash free.

Alternative positioning solutions have also been investigated. Linear scales, mounted alongside the rail, can provide absolute linear positioning and better accuracy compared to the servo. Nonetheless, this solution is more costly and adds to the complexity of the system, bidding against the integrated servo solution. Laser scales

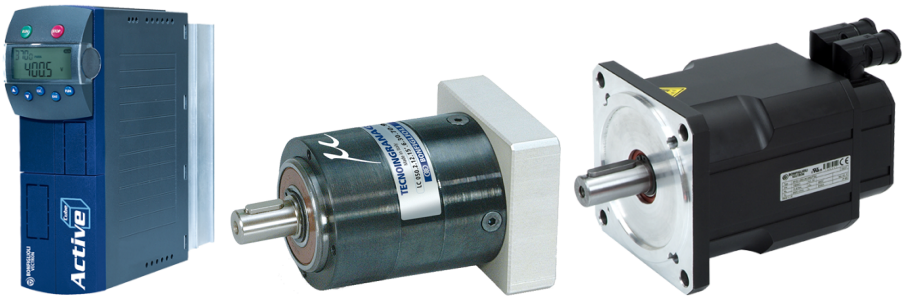

(a) (b) (c)

Figure 6.10: A complete industrial servo solution includes: inverter (a), servo motor (c) and gearbox (b). Here is shown the selected Bonfiglioli Vectron servo technology. Pictures source: *www.bonfiglioli.com*.

are another technology enabling true[1] absolute position. These instruments require static reference reflectors and are typically temperature compensated to achieve nanometre accuracy. The low market penetration of these devices and their inherently high costs led to them not being considered in the design.

6.5.2 Support Structure and Assembly

A dedicated structure is needed for the overhead design to provide rigid support to the railing system, but also to make the ceiling-fixed sensors platform more accessible to the operator. This floating configuration does not offer a flat surface on which to mount the rails, as would the floor. Instead, the beams will be unsupported between the selected span lengths, which have to be defined in this design. This will induce a beam deflection which will depend on two factors: the distance between adjacent supports and the applied load. The following is a calculation of deflection performed with data and formulas provided by the rail manufacturer HepcoMotion, relevant to the SBD20-80 rail system. The bending equation for a beam supported at two points separated by a distance L, with a load W applied at the midpoint, enables estimating the worst case deflection d as:

$$d = \frac{WL^3}{48EI} \tag{6.8}$$

Where E is the Young's modulus of the material and I the section moment of inertia. Lengths are measured in [mm] and forces in [N]. With the following formula it is also possible to estimate the deflection of the beam under its own weight.

[1]Linear scales and servos measure the carriage (or pulley) position relative to their own. Instead, laser scales can be referenced against the facility's walls, thereby compensating for possible structural motions.

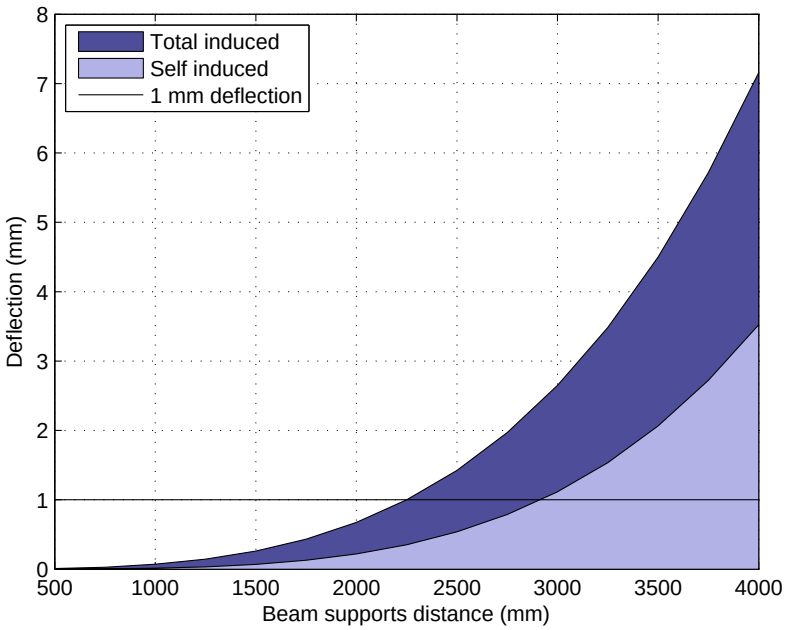

Figure 6.11: Deflection plot for a horizontal beam supported at both ends. The data is derived from the selected SBD20-80 rail mechanical properties and evaluated for growing distance between the supports. The light area shows the deflection under the beam's own weight, while the dark area includes the effect of a 25 kg load.

$$d = \frac{5L^3}{384EI} \times \frac{LQg}{1000} \tag{6.9}$$

Where Q is the mass of the beam given in [kg/m] and g the acceleration of gravity. Note the division by 1000 to equalize the length units. The total deflection can be obtained by adding the two effects. The result is plotted in Figure 6.11 against a variable support span. This is the expected worst case deflection of a single rail under the two combined effects, with a load of 25 kg (50 kg divided between the two rails). Here we can see how, if the threshold is set at 1 mm, the supports distance should not be much longer than 2 m. Since a larger span will also mean higher loads on each rail fixing point, I have decided to place the joints every 1.2 m. The actual spacings are compatible with the truss beams placement.

As any material manifests elastic properties, there can never be an absolutely rigid structure, able to withstand the rails' static load without deformation at any point along its span. Deformations are introduced both during assembly and during testing. Furthermore, deformations will not only be static but also dynamic, with

vibrations that may become hard to damp if too close to the structure's eigenfrequency, to the point of disrupting the measurements and reliability of the setup and the quality of the measurements. During the design, one can only define a maximum tolerated deformation where the final structure should fall in, to reduce the risk of having a less reliable measurement setup. The optimal approach is to use statically determinate (or isostatic) structures, that is structures in which the number of degrees of freedom of each element is compensated by an equal number of independent constraints. This condition guarantees stability against mechanical and thermal stress. A truss is an example of such a structure, widely used in architecture and structural engineering for stages, bridges and buildings. The use of triangular units makes the truss a strong support as par as heavier solid beams. For this facility, a truss can be used for bridging the building's reinforced concrete ceiling beams and supporting the transport rails. A wide variety of designs have been created along the years, though the most appropriate solution is chosen to be a standard trussed mast mounted horizontally.

The mast acquired for the facility has a squared section and its trussed profile is extended along its length on all sides. The constructor allowed to define some of the geometrical properties, so the shape could be adapted to the needs and constraints of the facility. Due to logistics constraints in bringing the parts inside the room, the mast has been divided in three sections of 2.7 m each, for an assembled length of 8.1 m. This length offers the longest possible support to the rails without interfering with the pre-existing ventilation and cabling systems. The side length is 600 mm, for a final positioning of the rails at about 1 m from the ceiling and 2.2 m from the ground. One important factor in all structures is the material. This one is made of galvanized massive iron, for best strength and durability.

The truss structural analysis performed by the constructor, has resulted in an expected maximum vertical truss deformation of about 1 mm. The value is calculated for an expected load of about 250 kg (including rails, manipulators and sensors) distributed to about 35 kg/m along the assembled 8.1 m structure, mounted to the ceiling via four uniformly distributed points. Figures 6.12 and 6.13 depict a CAD view of the test area from a top view and interior view. Drawings of the designed interface elements are found in Appendix C.

6.5.3 Cables Management

For preventing cables damage and reducing safety risks, I have decided to include a cable carrier system for the routing of all power and data cables required, from their fixed location to the moving carriage. The design parameters concerning a commercial cable carrier involve standard mechanical properties such as section size and length, which depend on the amount and size of the routed cables. A critical parameter is the carrier return loop bending radius. The return loop is the region

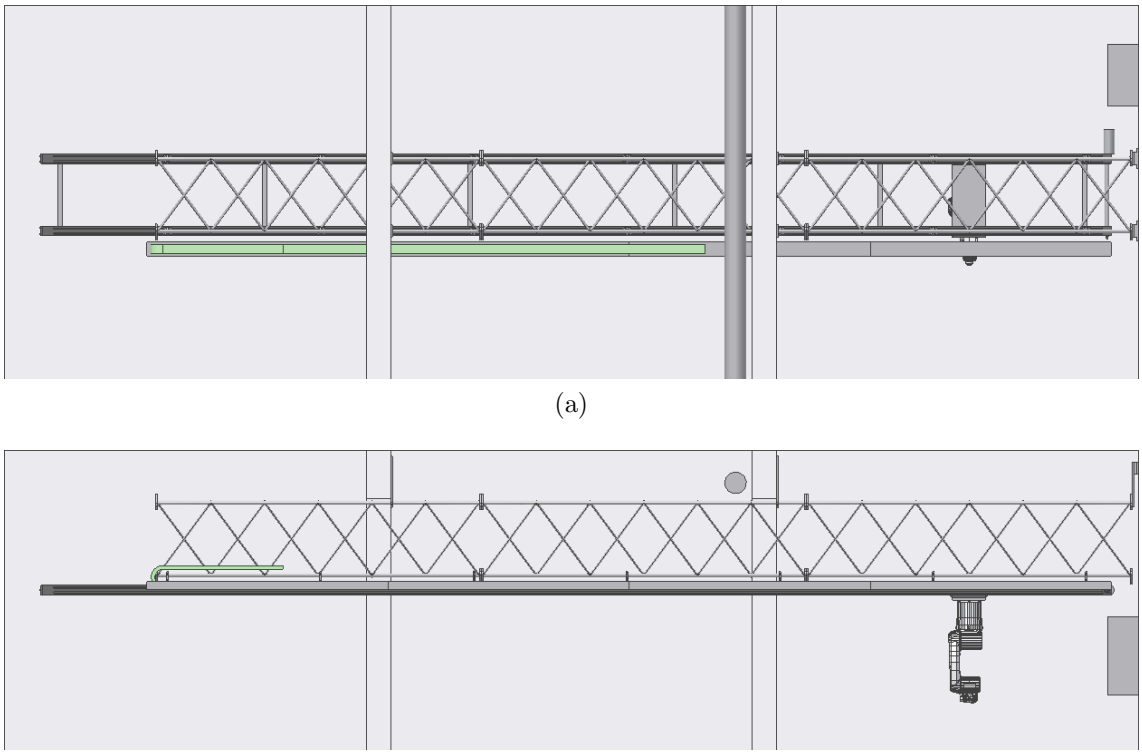

(a)

(b)

Figure 6.12: Top and side view of the test area ceiling mounted rail structure. The side view shows the robotic arm attached to the carrier platform.

applying the flexing force and therefore the most mechanically stressful point for the cables. The carrier bending radius has to be chosen as the cables minimum tolerated bending radius. KUKA recommends a minimum of 50 mm for their robots' cables. A design rule of thumb, where data is not provided by manufacturers, uses the cable's outer diameter: $R > 10D_{max}$. To allow for more flexibility toward unforeseen future test setups, I have picked dimensions slightly larger than currently estimated.

For optimal sizing, the carrier's fixing point is located midway through the rail stroke and its length is defined by the simple formula below. The loop length L_{loop} varies according to the chosen bending radius.

$$L_{track} = \frac{L_{stroke}}{2} + L_{loop} \tag{6.10}$$

Due to the cable track being able to self support only for short lengths, a metal guide channel has been added to the solution, making it possible to extend and sustain the track along the whole rail stroke length. The guide is produced by the same manufacturer and is built to offer two levels of support, both for the lower and

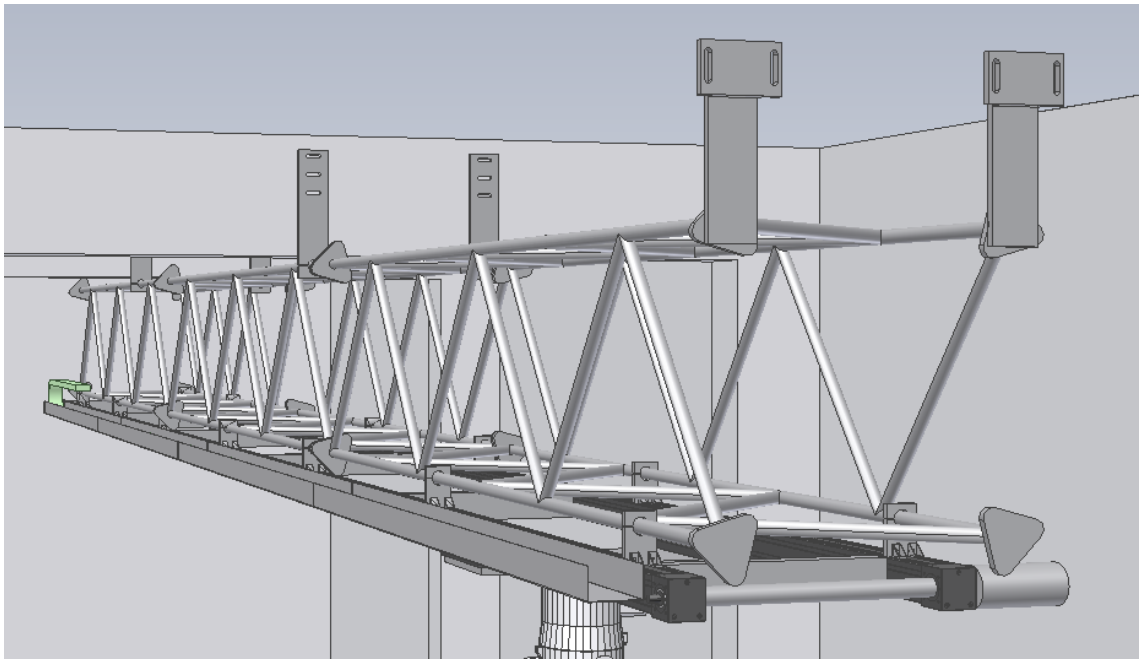

Figure 6.13: Drawing of the railing and the supporting truss elements. On the side is also mounted a cable carrier system.

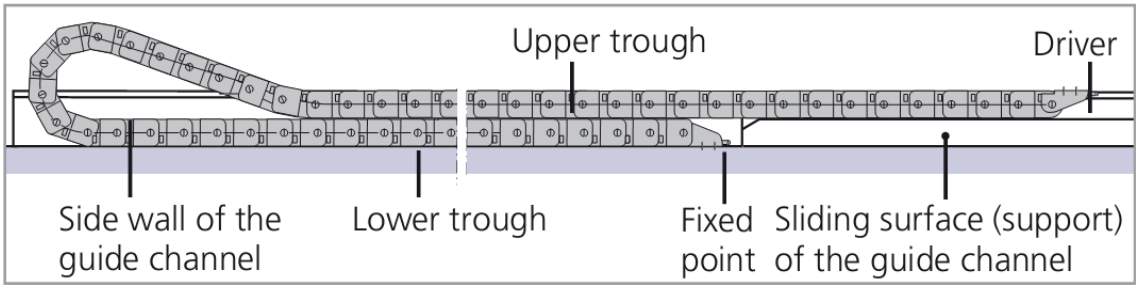

Figure 6.14: Cable track system for routing connections between moving machines. Drawing source: *www.kabelschlepp.de*.

for the higher track segments gliding along each other, as shown in Figure 6.14. The guide has been mounted alongside the railing on the opposite side of the servo.

6.6 PLANETARY SURFACE MODEL

For testing planetary landing sensors, the facility includes an artificial terrain that reproduces various planetary landscapes at different scales, inspired by data from various orbiters. Accurate mirroring of real existing regions is not important for

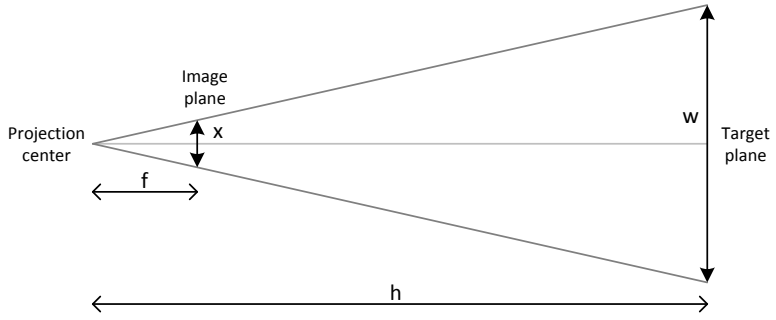

Figure 6.15: Camera perspective projection model.

two reasons: first, the landing area is mission dependent and will not be defined until a later phase; second, the system should be able to operate with all types of surface features. Due to the unstructured natural terrains of Lunar and Martian environments, the typical features include craters, cliffs and boulders (ref. Section 3.3).

The choice of the material for making up the scene can be restricted to a combination of granular materials and clays. Various types of sands or other powdered compounds are of potential interest. This gives moldable and easy to rearrange materials with the flexibility required to shape all sorts of terrains. The color of the selected constituents does not matter as much as their reflectance properties, as camera sensors for landing will likely be grayscale. A closer surface BRDF approximation is instead desirable, in order to ensure higher fidelity.

Surface scale and features resolution are defined according to the anticipated mission profile. For example, most spacecrafts have been flying in Lunar orbit at an altitude of 100 km. An optical head with focal $f = 10$ mm and a 6.5×4.8 mm sensor will have a FOV of 36×27 degrees. According to the camera projection model (Figure 6.15), the viewed surface width (for $x = 6.5$ mm and a downward looking camera) can be calculated as

$$w = \frac{x}{f} h \tag{6.11}$$

Resulting in 65 km at full scale ($h = 100$ km) and 1.3 m for an assumed 2 m mock-up distance. The system scale is then 50000:1.

Two different landscapes have been arranged. One meant to test high altitude terrain relative navigation; thus with the largest scale ratio and a morphology mimicking mountains, valleys and big craters. Another built for closer range, aimed at the final descent phase. Since the problem is to find hazards to the spacecraft's body, the scene replicates boulders and depressions at a considerably smaller scale ratio. The size of the planetary surface mock-up fits the dedicated space of about

2.5×6 m, within the laboratory test area as can be seen in Figure 6.18. With this setup, different image sequences have been recorded with camera fly-bys and approaches which have helped testing the algorithms described in Chapter 3.

6.7 LIGHTING CONTROL

A sensitive element of a laboratory dedicated to the operation of spacecraft vision based sensors, is the control of illumination sources and their diffusion within the scene. The scene lighting takes from professional photo studios and theatres. Photographers make use of many tools for manipulating light sources, both physically and optically by placing them, for example, on flexible tripod-mounted arms and attaching various diffusers or concentrators of light depending on the desired effect. Such tools and methods can indeed be very practical for deploying lighting around the facility. What follows is a coverage of the work done to accomplish lighting control.

6.7.1 Curtaining

Complete optical isolation of the test area from the rest of the facility is obtained by a custom made curtain arrangement. Given the defined test area, the curtain should offer the following features:

- Floor to ceiling light blocking on the entrance side,
- Easy access to the test area through full opening,
- Complete closure for the tests.

A structure for sustaining the curtain railing and ensuring complete confinement of the test area has been constructed and mounted along the areas division line. A drawing is shown in Figure 6.16. The structure extends along the whole room's width and is fixed to the ceiling. Two curtains are running wall to wall to provide flexible access zones. These curtains do not extend to the full room's height, therefore a ceiling fixed tapestry of the same garment is attached to the support structure. Valance (vertical overlap) is included for better light blocking. The walls of the optical target area can be blackened arbitrarily if a true black background is desired. Another internal curtain arrangement may eventually allow to divide the test area in separate modules and run different experiments at the same time.

The curtain for accessing the test area and shielding from external light has to be dark (so as to minimize internal reflections) and 100 % light blocking. Black is the favoured color. Various fabric samples have been acquired and evaluated, from the range of products dedicated to Sun blocking. These include: velvet, wool felt and polyester. Some materials present intense diffuse reflections, while others are limited to specular effects that are therefore mainly visible at direct angles. The

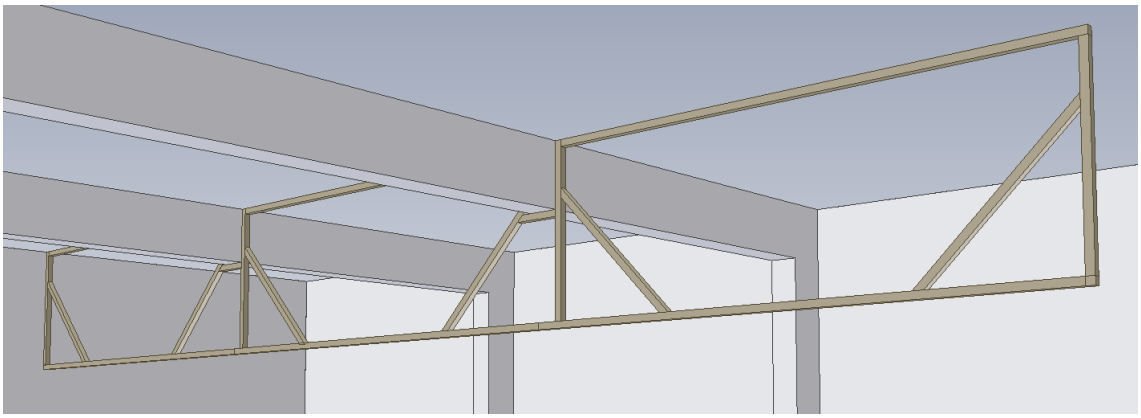

Figure 6.16: Drawing of the support skeleton on which the shielding curtains are mounted.

acquired polyester fabric has a very smooth and dense surface, resulting in limited light scattering and total light blocking (no light was leaking through when examined in broad daylight). Its low weight, combined with the previous features, makes it the fabric of choice for darkening the room.

6.7.2 Interior Lighting

The interior lighting solution includes equipment with two purposes: maintain clear visibility for the operator to move around and provide scene lighting according to each test scenario. Spot and LED floor lights are meant to illuminate some key areas without interfering with the test lighting or the sensors and have been placed accordingly. When the operator requires more light, the curtains can be fully or partially opened to let in light from the control area.

The testing lamps are mounted on tripods with flexible heads so as to give stability and flexibility for different arrangements. A high power lamp is used to generate the primary light. Different techniques can be employed if a parallel beam is required, involving the use of a parabolic mirror or a Fresnel lens. These are currently under investigation.

Secondary diffuse lighting is achieved by shining a wide cone of light against one of the side walls not covered by curtains. An additional set of curtains can be mounted in order to prevent these lamps to be detected by the cameras or to partition the area for isolated tests that have to be run concurrently and independently from each other.

6.8 SUMMARY

This chapter has covered the design of a calibration and testing facility for vision based sensors. The work has covered study of the possible mechanical setups and various designs for achieving accurate and flexible positioning of the sensors with respect to the targets. The laboratory now includes a nine meters linear rail and a six axis robotic arm operated remotely and in a lighting controlled environment. It is now possible to simulate scenarios ranging from formation flight to planetary landing, including trajectories, lighting and target scenes.

A suggestive shot of the completed facility is shown in Figure 6.17. All systems are integrated and have already been used for various experiments. Testing and verification of new non-cooperative algorithms for formation flight are being performed at the time of writing as part of the ESA PROBA 3 mission. A 10:1 scale model of the target spacecraft is now under scrutiny by the Department camera sensors dancing around it. Additional pictures are included in Appendix C.

An advanced feature of the test facility would be the implementation of a true orbital model, where a simulation computer generates the virtual kinematics of the case. Closed loop actuation, according to these "true" orbital trajectories and vision sensor data, is then generated. This requires tools for translating the modelled trajectories to actual manipulators commands. Furthermore, on the other end of the loop, an interface between the sensor processing unit and the simulation computer should be designed. This is open for future development, as it is expected to play an important role for achieving complete ground validation.

Figure 6.17: The finished laboratory, arranged for a rendezvous test scene.

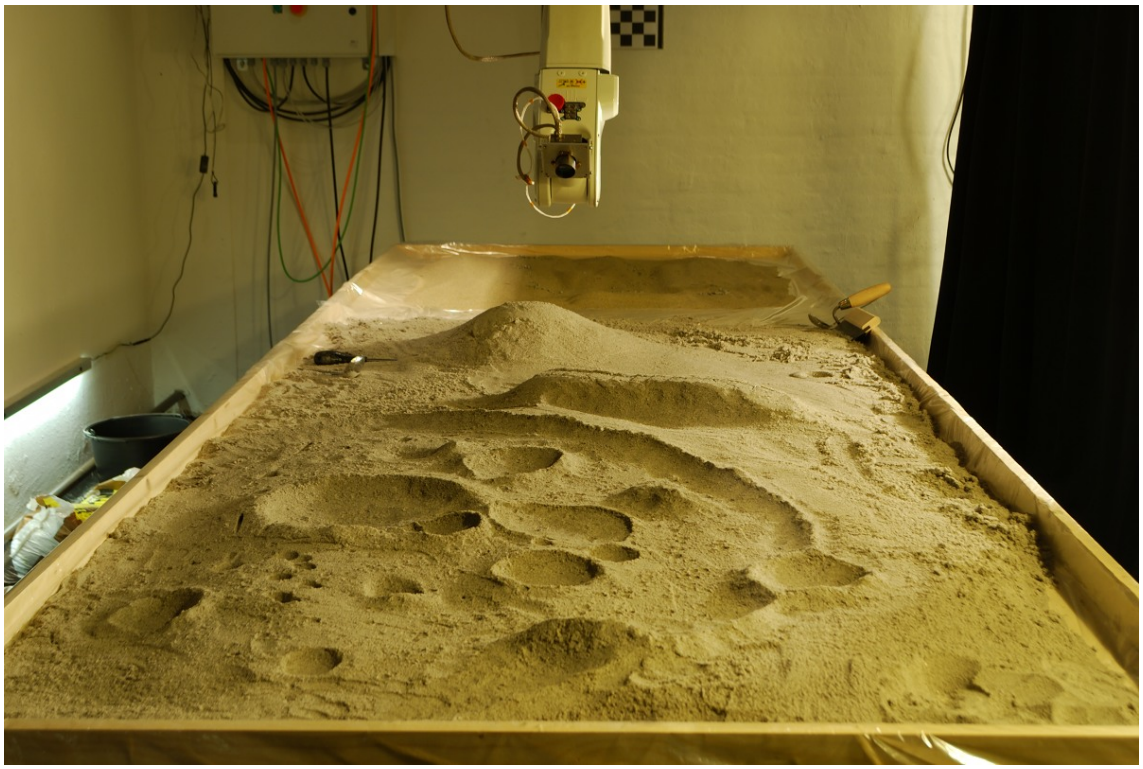

Figure 6.18: Simulated planetary terrain setup.

CHAPTER 7

Conclusions

A feasibility study targeting vision based autonomous lunar landing has been completed and documented in this report. Synthesis of key elements for an optimal awareness sensor shows the potential of novel algorithms for determining the spacecraft ego motion during descent and the identification of surface hazards for safe landing. Experimental solutions have been investigated and implemented on a commercial computer setup, with algorithms optimized for the constraints of the case. The documented results – in terms of autonomy, accuracy and execution time – are encouraging, opening the way to a hardware implementation on a representative processing system for further analysis.

Design and testing of the software and hardware tools developed for calibration and validation of the PRISMA VBS sensor are also described in this book. These components have contributed to assessing the correct functionality of the sensor and improving the precision of the pose and position determination. The Pharos OGSE has expanded upon a previous generation camera stimulator and now includes precise control of a collimated light beam projected onto the image sensor. This capability can be used to simulate distant luminous objects moving relatively to a starfield. A practical use for this device is the ground verification of asteroid detection filters, which DTU Space has installed on the stellar compass flying onboard the NASA Juno spacecraft.

The experience and know-how that I have gained alongside this effort was applied to the ground up design and integration of an optical test environment, meant for supporting the development of all future vision based sensors at DTU Space. The architecture of the facility is suitable for the deployment of representative deep

space and planetary landing scenarios. Simulated sequences, recorded within a lunar analog setup, were employed for evaluating the novel landing algorithms. The laboratory is also being used to verify non cooperative algorithms designed for the ESA solar coronagraph mission PROBA-3.

7.1 RECOMMENDATIONS FOR FUTURE WORK

Concerning the VBLS, both MOHVE and MOSARD should be further tested under varying conditions (i.e. lighting, terrain morphology, trajectory). Additional performance tests are also recommended. Eventually, implementation of optics and algorithms on a qualified engineering model, ideally based on heritage from DTU's Advanced Stellar Compass, would be a big step towards increasing the sensor's TRL. Investigation about IMU data fusion with the camera is another pending task.

A preliminary investigation about optimal terrain relative navigation techniques is currently under way for breaking down the global and local positioning problems. A novel crater identification and categorization method based on statistical moments is being studied. This is expected to outperform other methods that make use of Hough transform for shapes recognition.

Concerning cooperative target calibration, more research remains to be done about finding and implementing a precise and reliable fine tuning algorithm. Furthermore, the insight gained during this work can be applied to other related problems of formation flight and rendezvous (e.g. non cooperative target identification and tracking).

Concerning Pharos and the subject of validation tools, it is envisaged the augmentation of the module with additional functionality. Features such as controllable target beam width and movable background starfield are desirable for various upcoming experiments.

Concerning the calibration and validation VBS laboratory, a complete integration of synchronized control and telemetry of the manipulators remains to be done. Testing of new cooperative algorithms for the PROBA-3 mission would benefit from these capabilities. Improvements on the lighting system and sampling of different soil compounds, possibly complemented by photometric analysis, may provide better fidelity for the planetary analog terrain.

APPENDIX A

Calibration Extras

A.1 PRISMA COOPERATIVE FM CALIBRATED PANELS

The following figures show the collection of imaged centroids and calibrated mires' coordinates acquired during the flight model (FM) calibration for each of the 6 faces. Face 7 is referred to the docking pattern located on face 5 ($-y$).

Table A.1 collects the mires coordinates before and after the calibration.

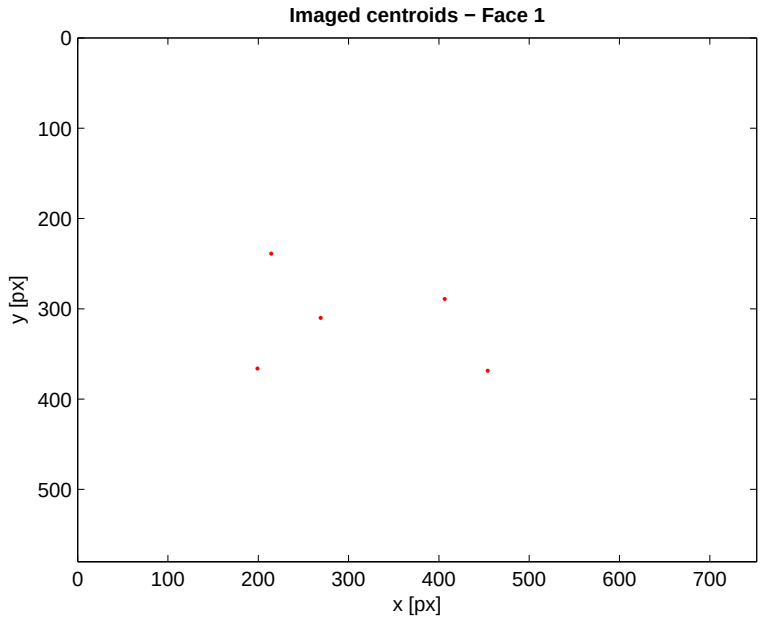

Figure A.1: PRISMA target FM imaged face 1 ($+x$) centroids acquired for calibration.

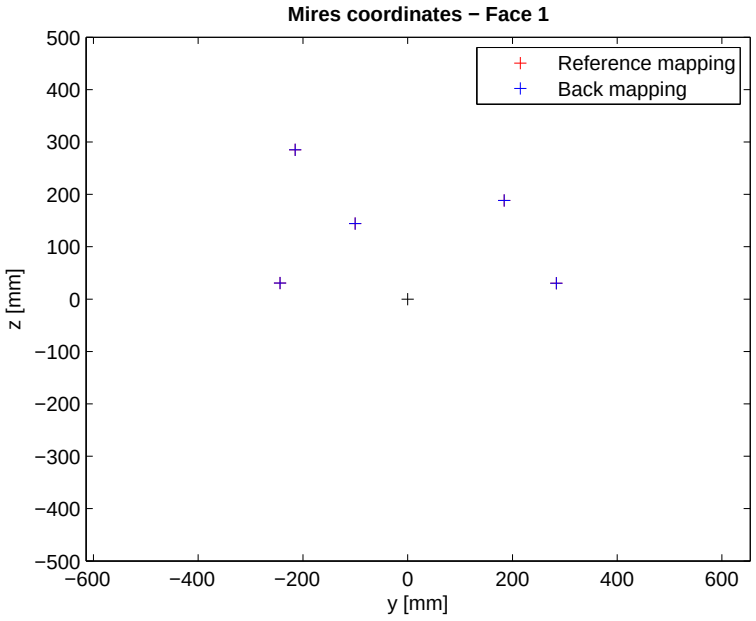

Figure A.2: PRISMA target FM calibrated face 1 ($+x$) mires expressed in spacecraft frame coordinates.

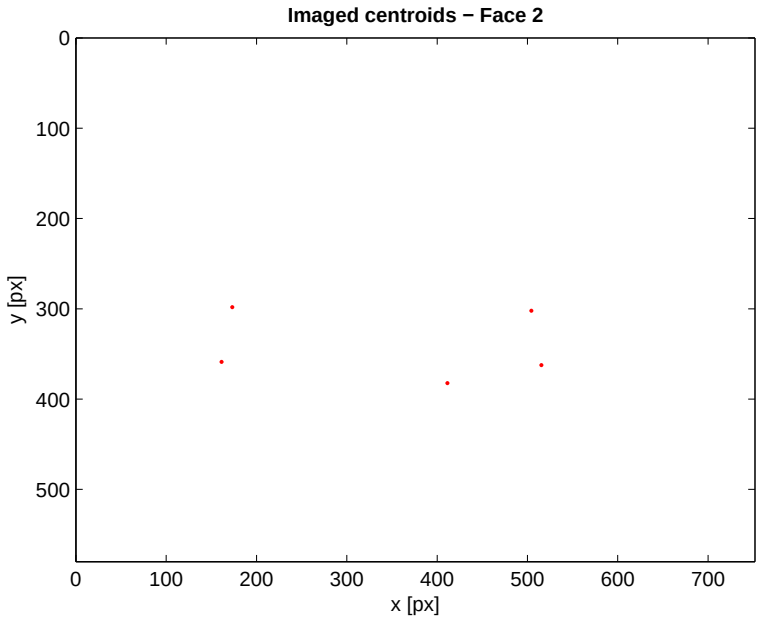

Figure A.3: PRISMA target FM imaged face 2 ($+y$) centroids acquired for calibration.

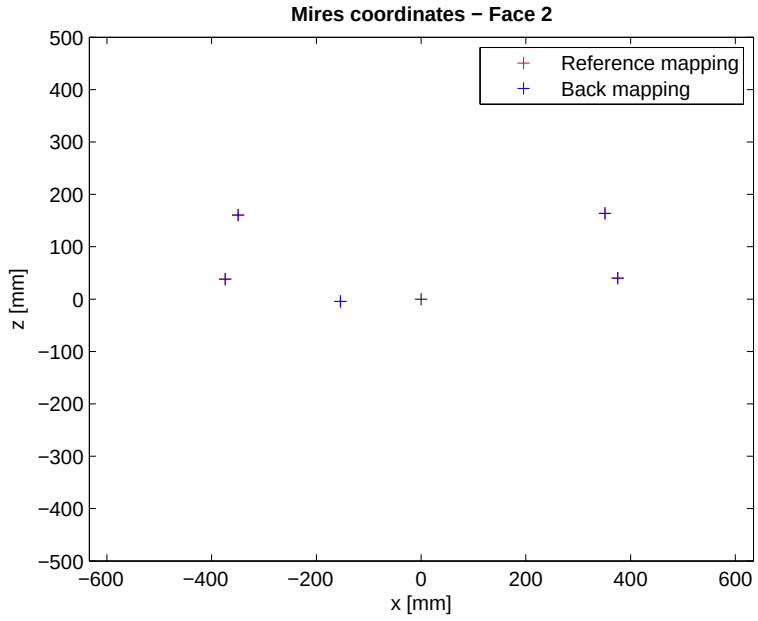

Figure A.4: PRISMA target FM calibrated face 2 ($+y$) mires expressed in spacecraft frame coordinates.

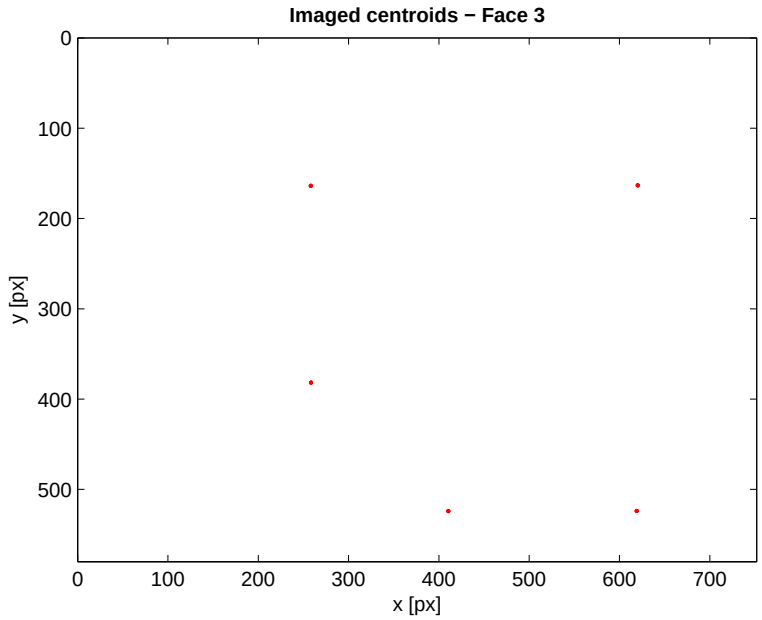

Figure A.5: PRISMA target FM imaged face 3 ($+z$) centroids acquired for calibration.

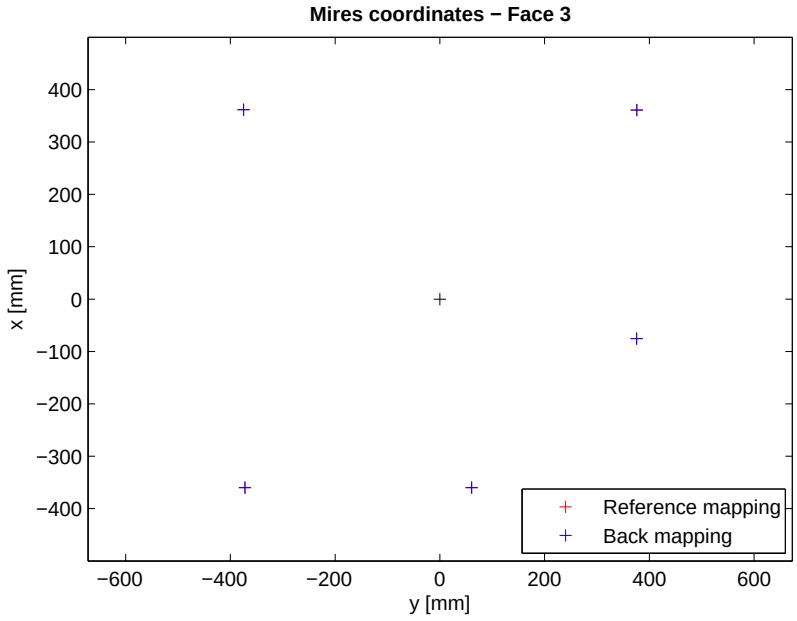

Figure A.6: PRISMA target FM calibrated face 3 ($+z$) mires expressed in spacecraft frame coordinates.

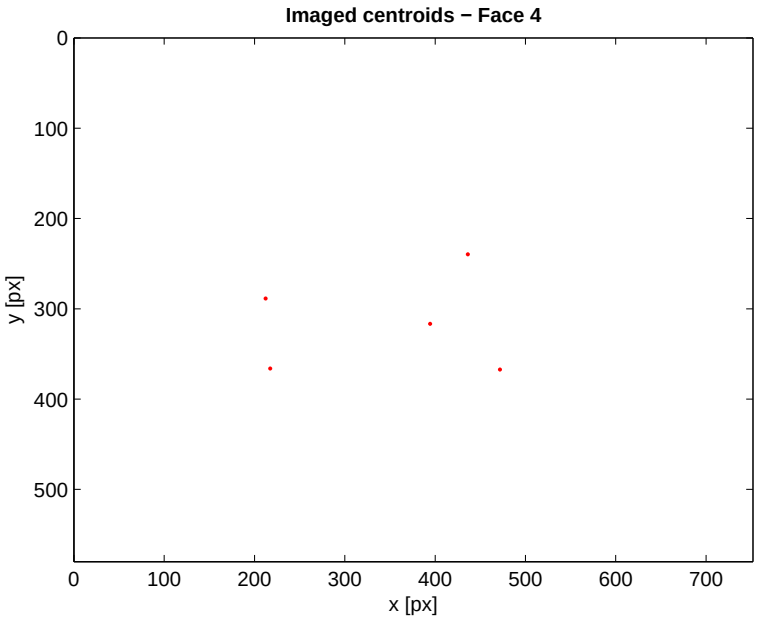

Figure A.7: PRISMA target FM imaged face 4 ($-x$) centroids acquired for calibration.

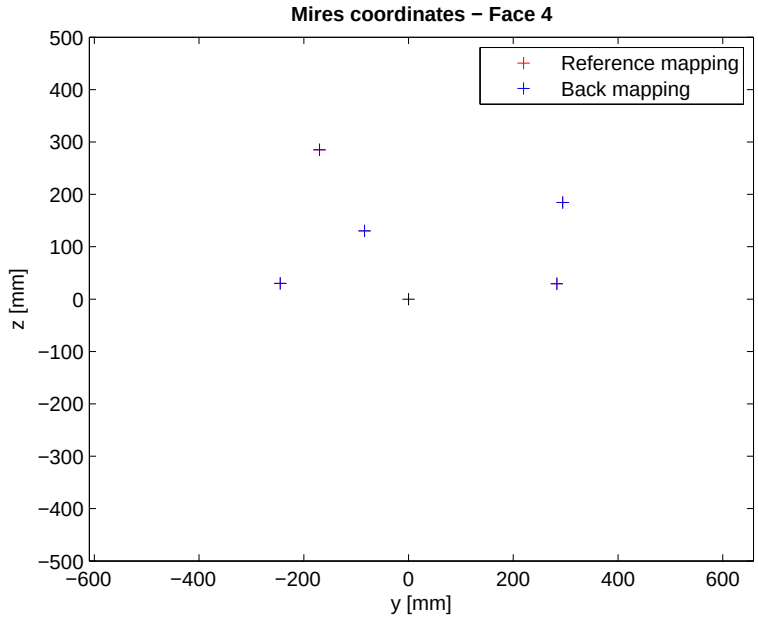

Figure A.8: PRISMA target FM calibrated face 4 ($-x$) mires expressed in spacecraft frame coordinates.

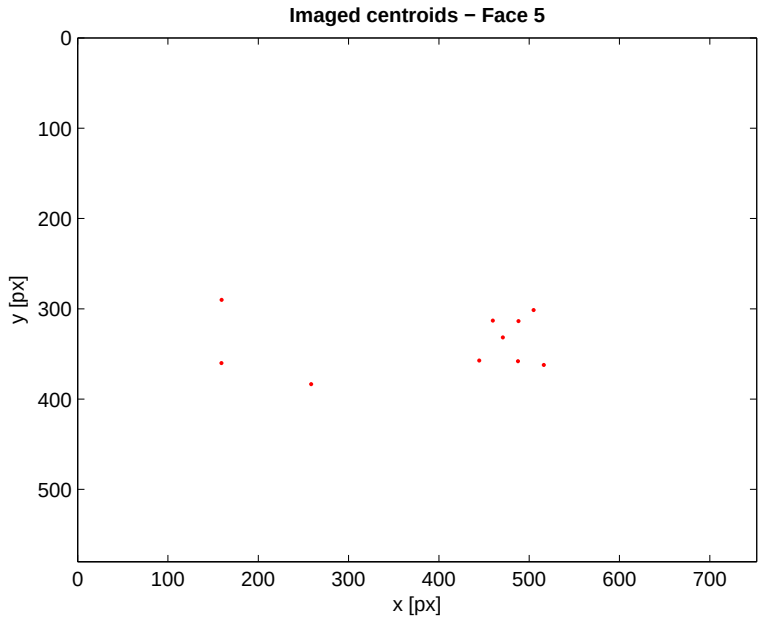

Figure A.9: PRISMA target FM imaged face 5 ($-y$) centroids acquired for calibration.

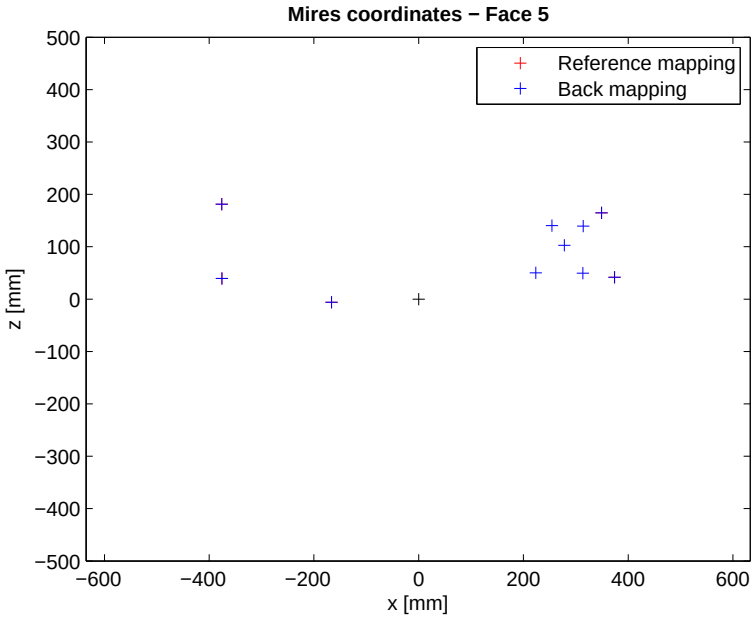

Figure A.10: PRISMA target FM calibrated face 5 ($-y$) mires expressed in spacecraft frame coordinates.

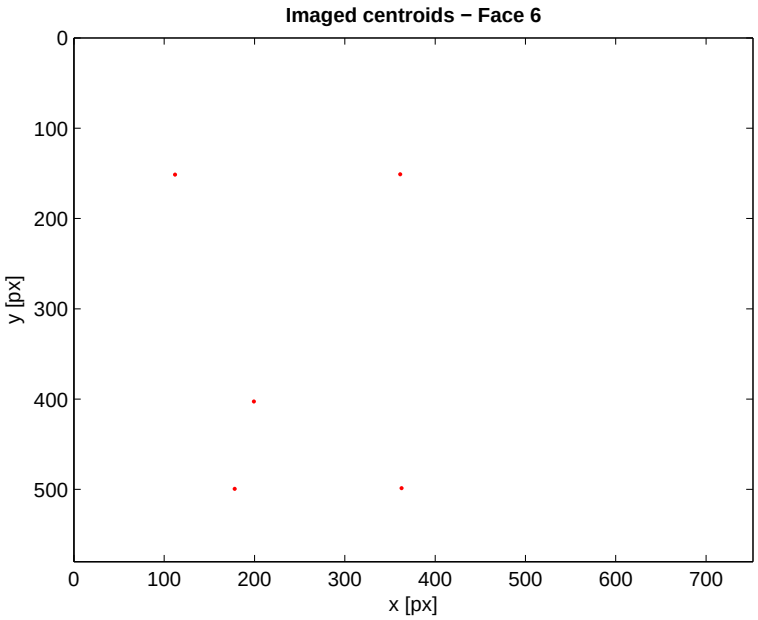

Figure A.11: PRISMA target FM imaged face 6 $(-z)$ centroids acquired for calibration.

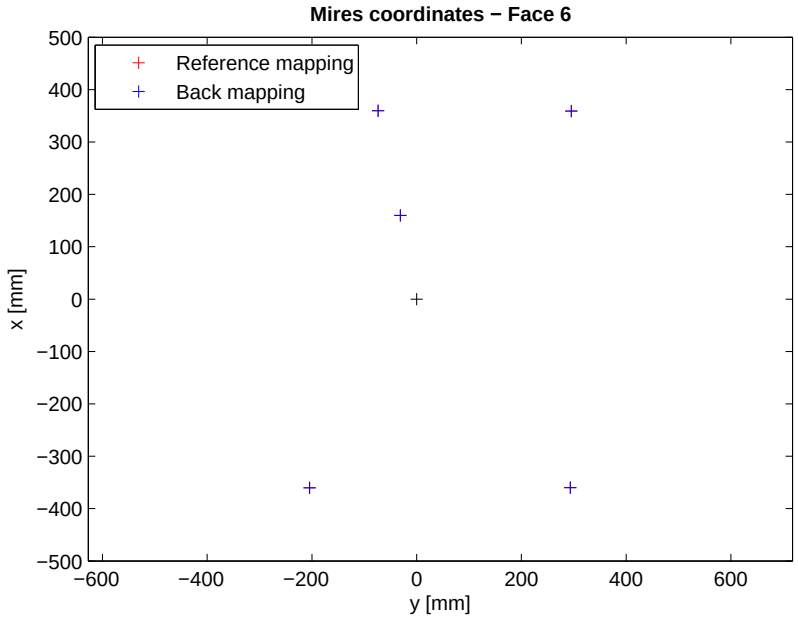

Figure A.12: PRISMA target FM calibrated face 6 $(-z)$ mires expressed in spacecraft frame coordinates.

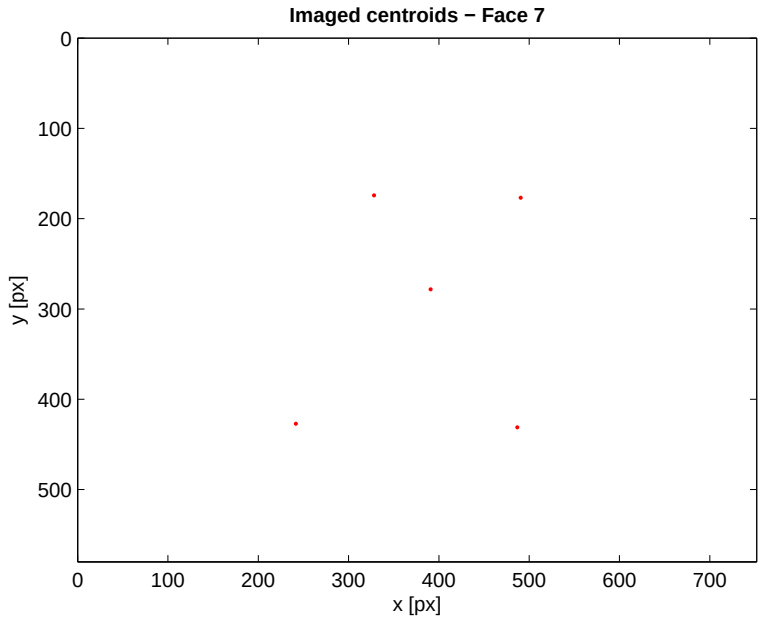

Figure A.13: PRISMA target FM imaged docking pattern ($-y$) centroids acquired for calibration.

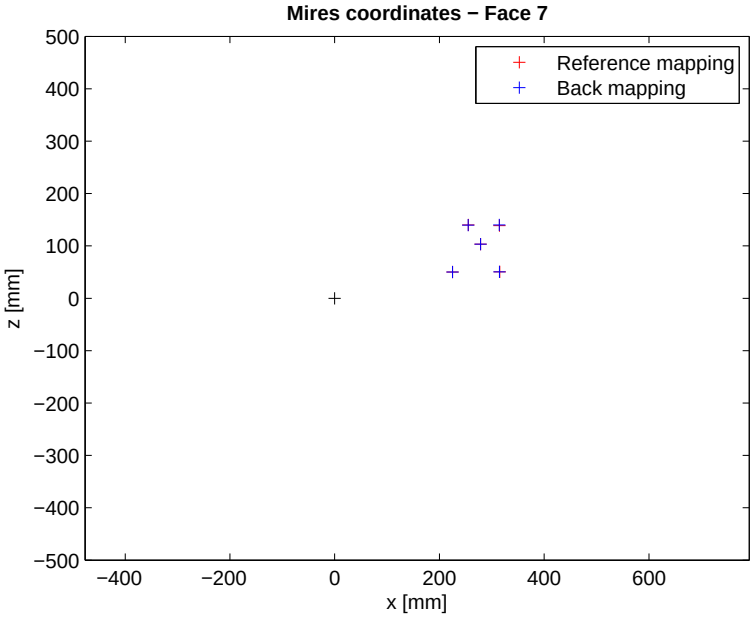

Figure A.14: PRISMA target FM calibrated docking pattern ($-y$) mires expressed in spacecraft frame coordinates.

Mire	Panel	Pre-calibration			Post-calibration		
1	1	375	-243,876	30,505	375	-243,876	30,505
2	1	375	283,947	30,474	375	283,9472	30,474
3	1	375	184,141	188,245	375	184,1408	188,2454
4	1	375	-100,235	144,106	375	-100,2353	144,1064
5	1	375	-214,858	284,993	375	-214,8575	284,9934
6	4	-375	-245,119	29,872	-375	-245,1189	29,8722
7	4	-375	-170,019	284,897	-375	-170,0191	284,8971
8	4	-375	-84,045	130,116	-375	-84,0452	130,1163
9	4	-375	294,444	184,592	-375	294,4442	184,5916
10	4	-375	283,2	29,391	-375	283,2	29,391
11	2	-375,9278	304,1741	40,8352	-373,9834	304,1741	38,0529
12	2	-351,4328	304,1741	163,3852	-349,4878	304,1741	160,6029
13	2	349,2462	304,1741	166,4922	351,1908	304,1741	163,7104
14	2	373,3712	304,1741	42,7782	375,316	304,1741	39,996
15	2	-156,1458	304,1741	-1,7198	-154,2014	304,1741	-4,5015
16	5	-367,2015	-275,7106	41,0106	-375,534	-275,7106	39,416
17	5	-157,9535	-275,7106	-4,3914	-166,2861	-275,7106	-5,9859
18	5	382,3365	-275,7106	43,3156	374,0039	-275,7106	41,7214
19	5	357,5215	-275,7106	166,1926	349,1893	-275,7106	164,5975
20	5	-367,5235	-275,7106	182,9216	-375,8559	-275,7106	181,3273
21	3	-362,4653	-373,393	323,4806	-359,8919	-372,0267	323,4806
22	3	358,9757	-375,967	323,4806	361,5489	-374,6009	323,4806
23	3	358,3567	374,526	323,4806	360,9305	375,892	323,4806
24	3	-77,9233	374,474	323,4806	-75,3495	375,8397	323,4806
25	3	-362,5863	59,218	323,4806	-360,0130	60,584	323,4806
26	6	-364,0956	-206,2676	0,8786	-360,2340	-204,4550	0,8786
27	6	-363,8936	291,4554	0,8786	-360,0323	293,2681	0,8786
28	6	156,0084	-32,8396	0,8786	159,8698	-31,0269	0,8786
29	6	355,3124	293,4414	0,8786	359,1738	295,2543	0,8786
30	6	355,9244	-75,5416	0,8786	359,7862	-73,7291	0,8786
31	5	232,0055	-275,7106	51,8606	225,0180	-275,7106	50,0260
32	5	322,0875	-275,7106	51,1896	314,5580	-275,7106	50,0260
33	5	322,6835	-275,7106	140,9926	314,2205	-275,7106	139,8727
34	5	263,0315	-275,7106	142,6576	254,9588	-275,7106	139,7214
35	5	286,5535	-295,7106	104,4366	278,5054	-295,7106	103,4976

Table A.1: Pre and post calibration PRISMA FM mires model. Units in [mm]

APPENDIX B

Pharos Extras

B.1 DRAWINGS AND PICTURES

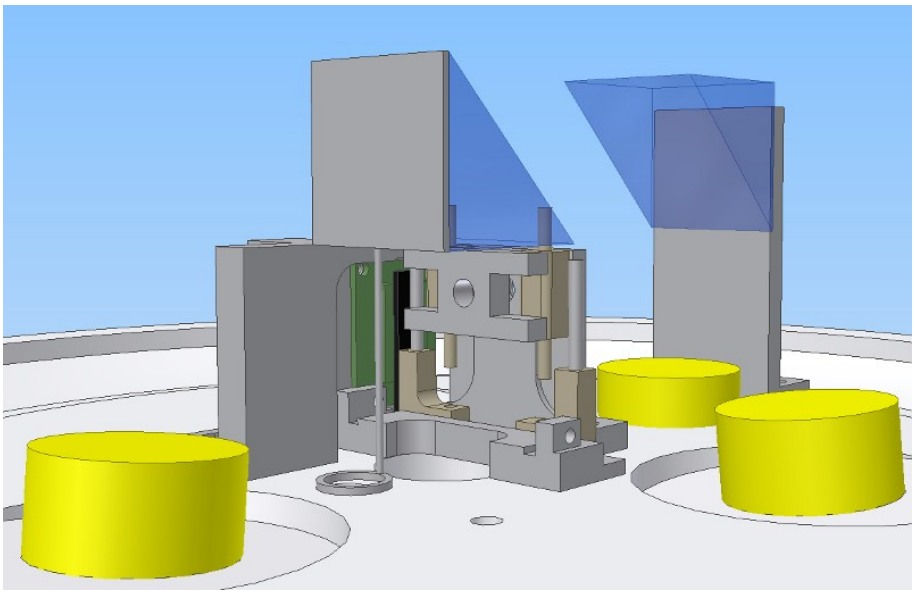

Figure B.1: Pharos 2 CAD design close up view.

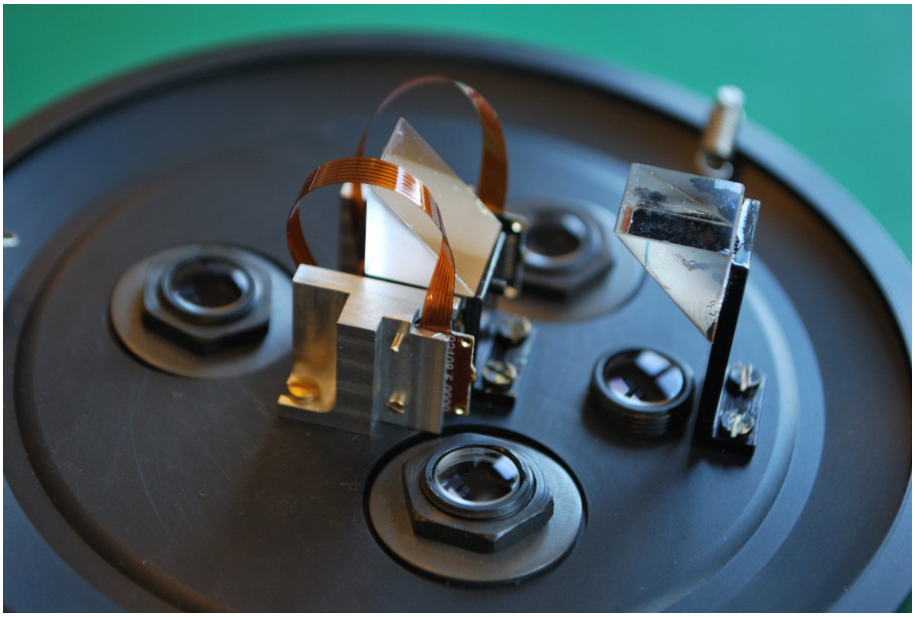

Figure B.2: Pharos 2 internal side view.

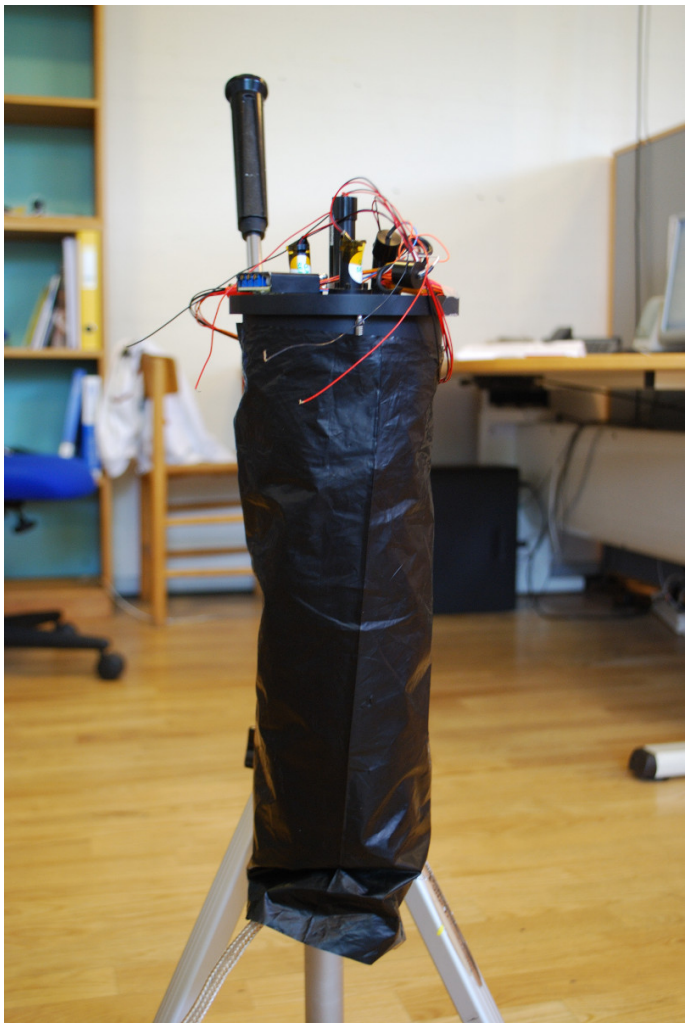

Figure B.3: Pharos test setup on a tripod mount. The obscured chamber connects the module to the camera head at the other end.

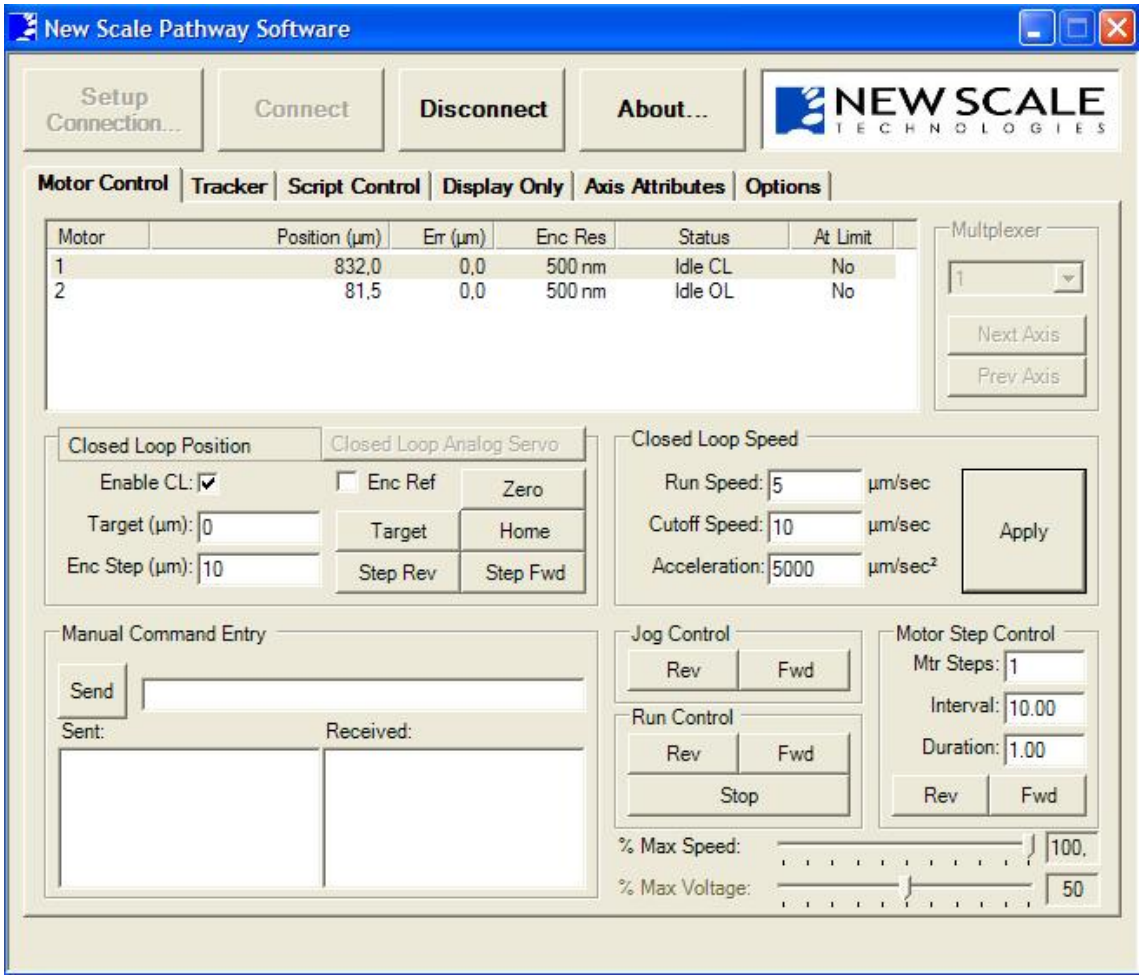

Figure B.4: Pathway interface software control for the Squiggle piezo motor.

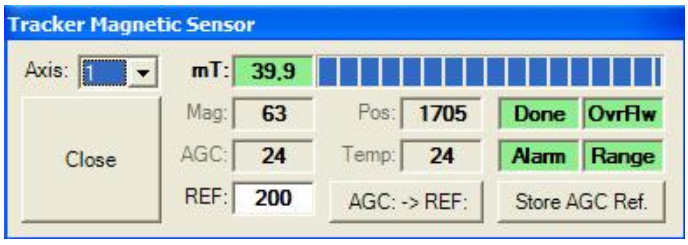

Figure B.5: Verification of sufficient magnetic field at each feedback sensor.

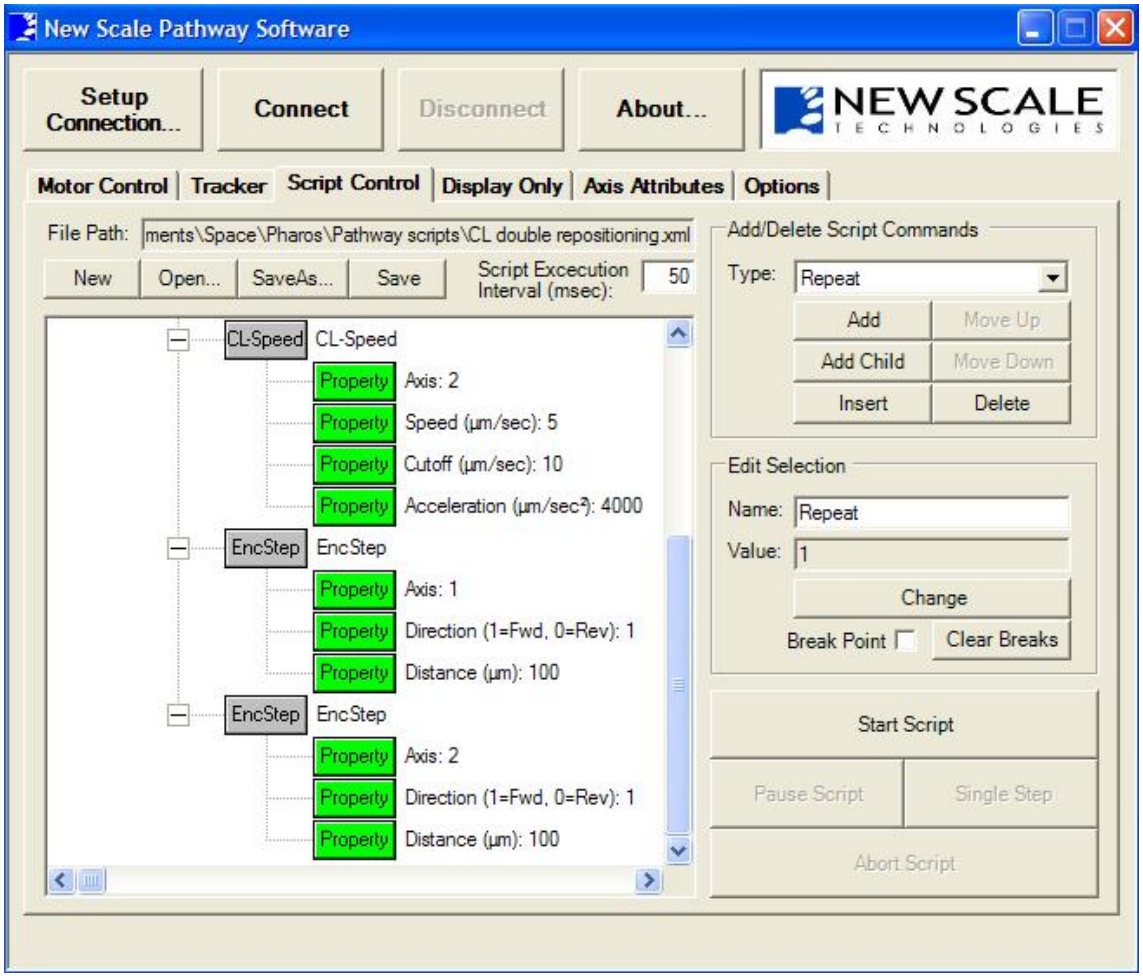

Figure B.6: Pathway software scripting interface for motion programming.

B.2 TECHNICAL DRAWINGS

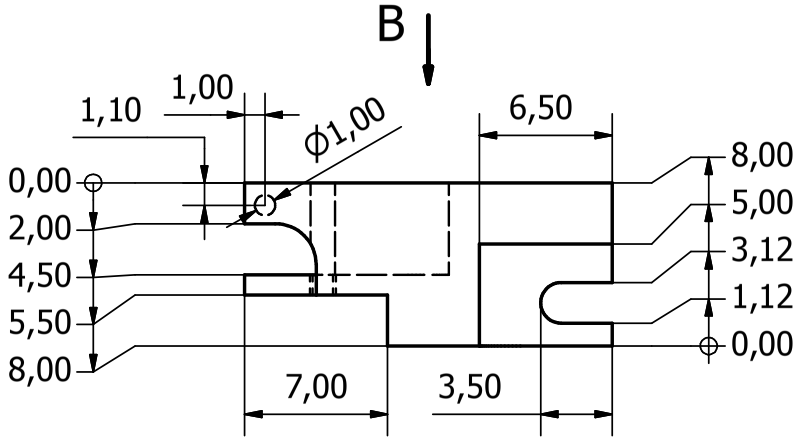

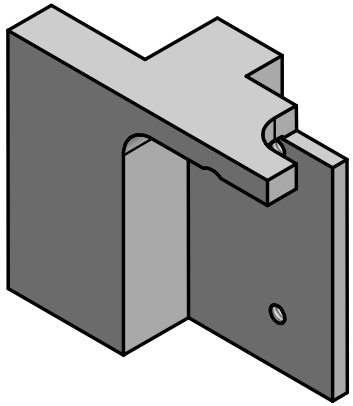

(3 : 1)

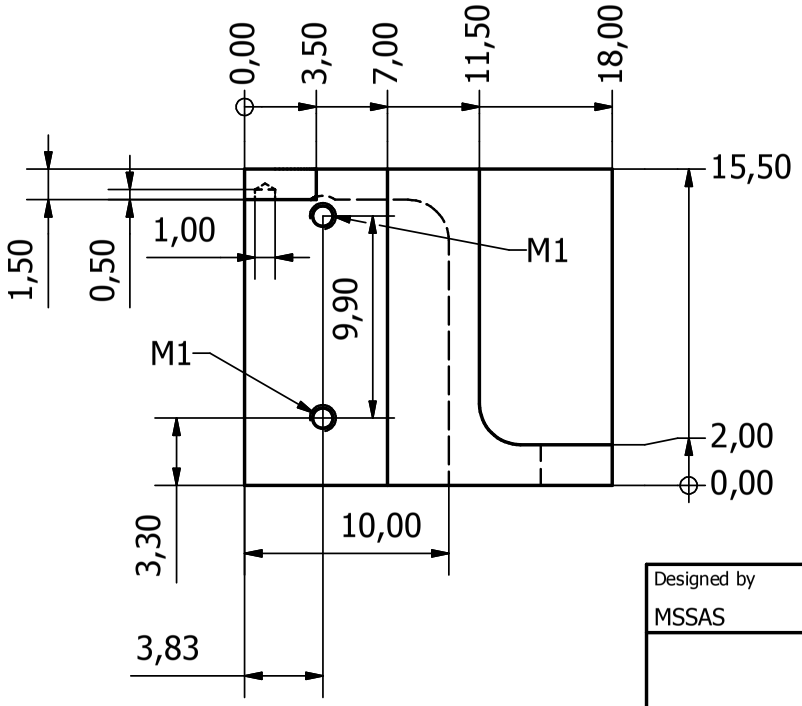

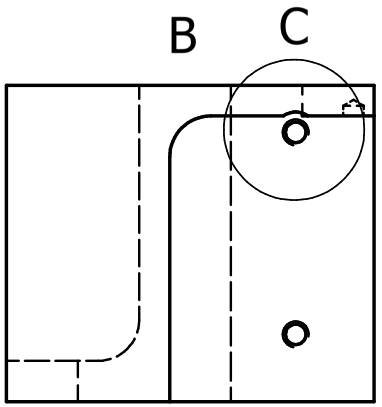

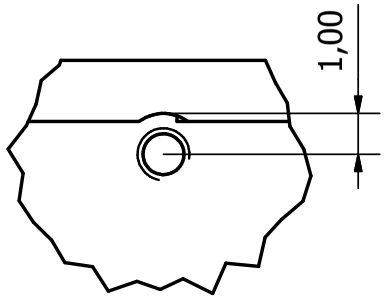

C (6 : 1)

Designed by	Checked by	Approved by	Date		Date	
MSSAS						

	mega_support	Edition	Sheet 1 / 1

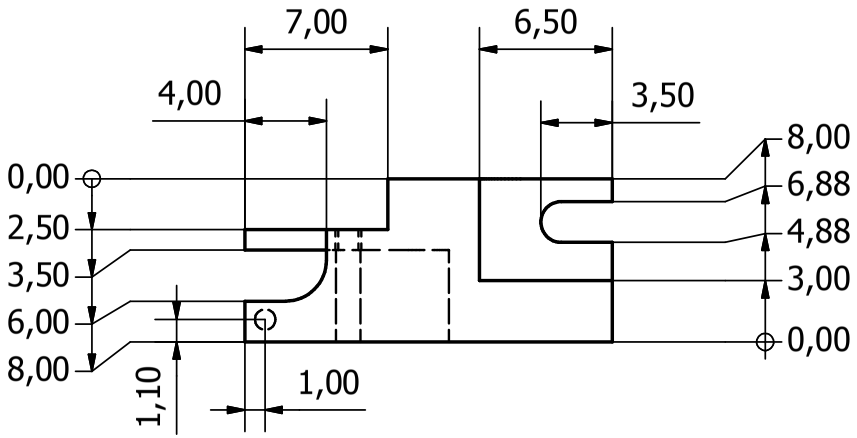

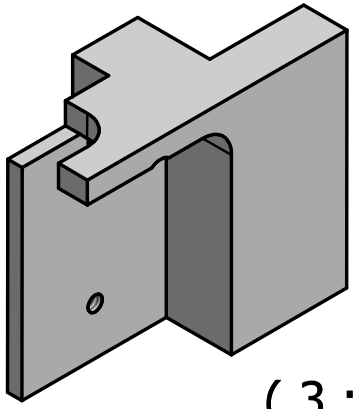

(3 : 1)

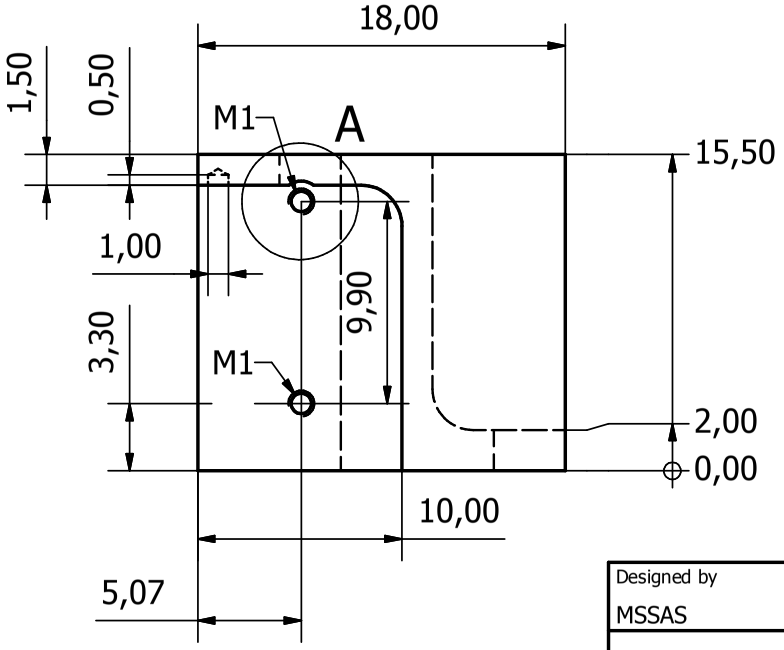

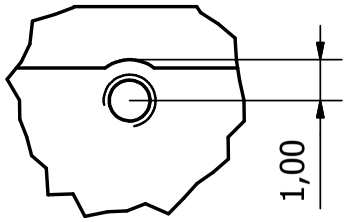

A (6 : 1)

Designed by	Checked by	Approved by	Date		Date	
MSSAS						

	mega_support_b	Edition	Sheet 1 / 1

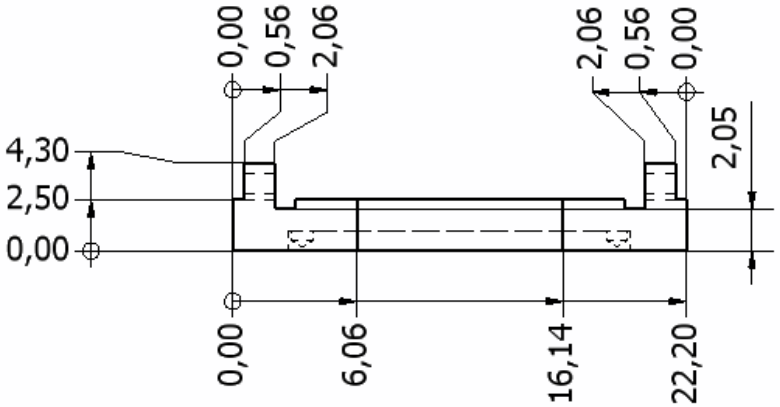

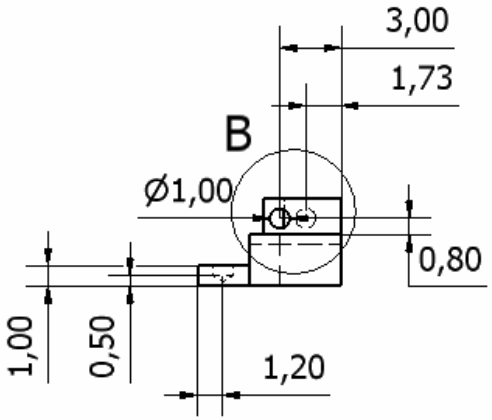

B (6 : 1)

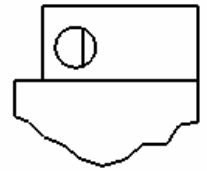

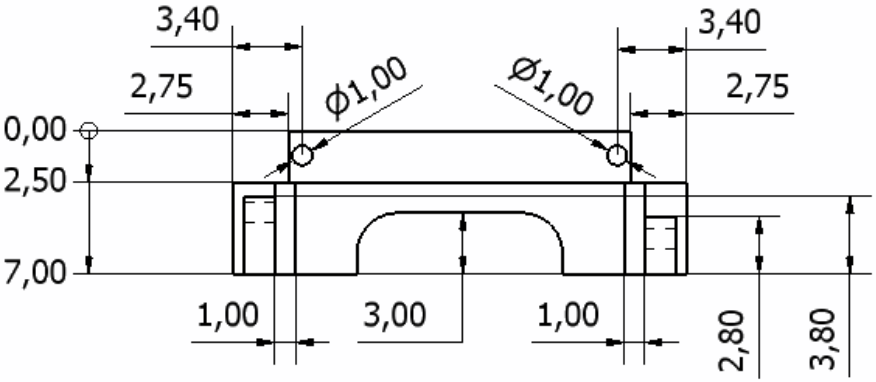

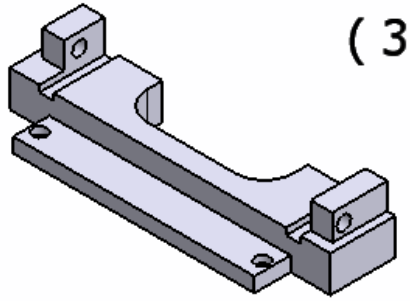

(3 : 1)

Designed by	Checked by	Approved by	Date		Date	
MSSAS						

	jack	Edition	Sheet 1 / 1

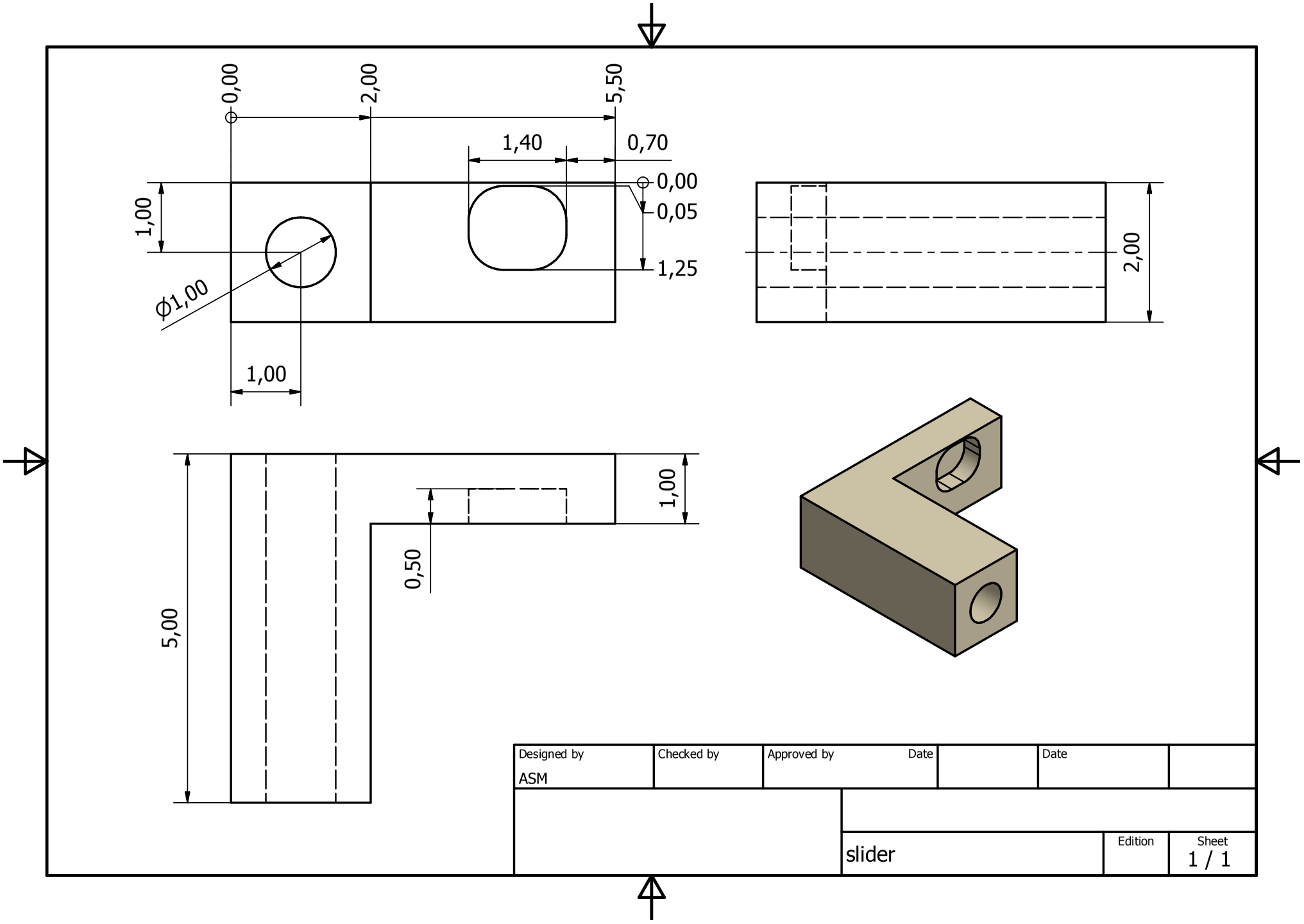

Designed by	Checked by	Approved by	Date		Date	
ASM						

slider

Edition	Sheet
	1 / 1

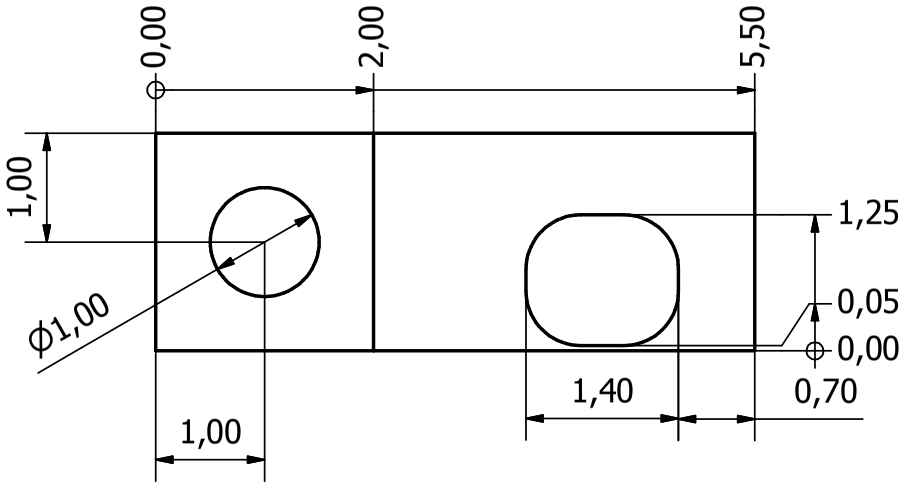

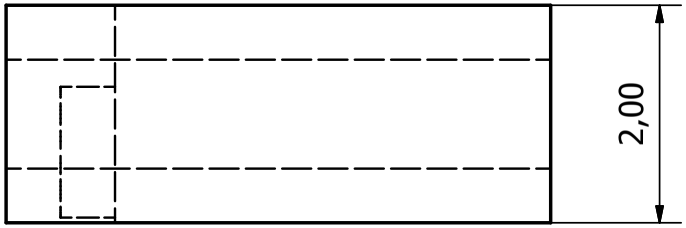

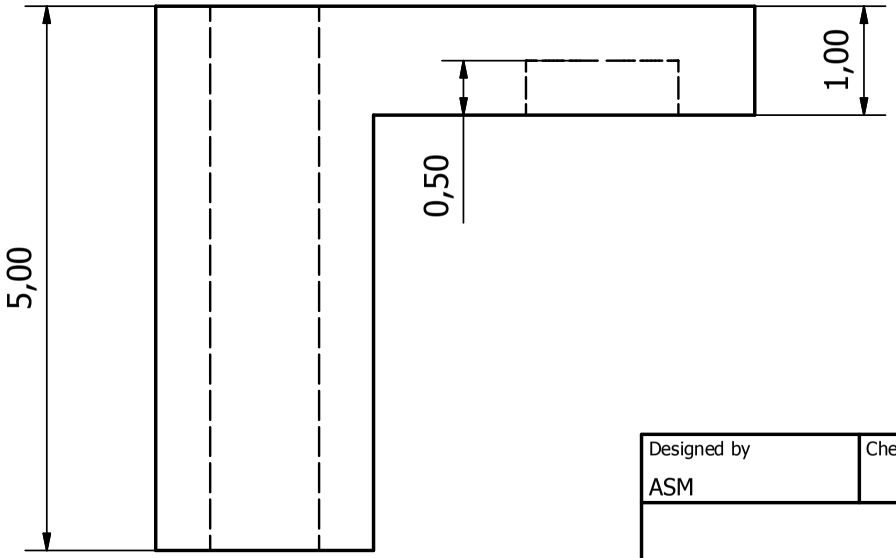

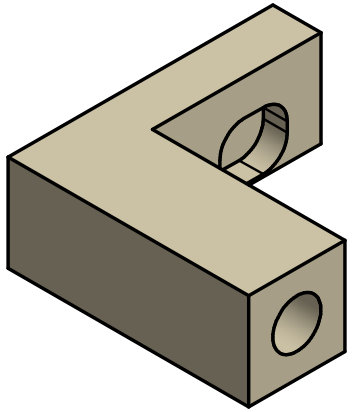

(10 : 1)

Designed by	Checked by	Approved by	Date		Date	
ASM						

	slider_b	Edition	Sheet 1 / 1

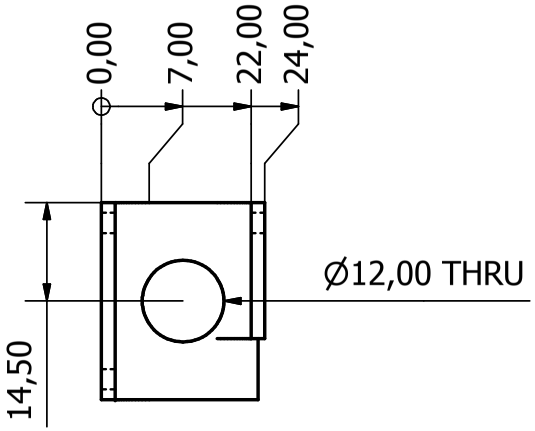

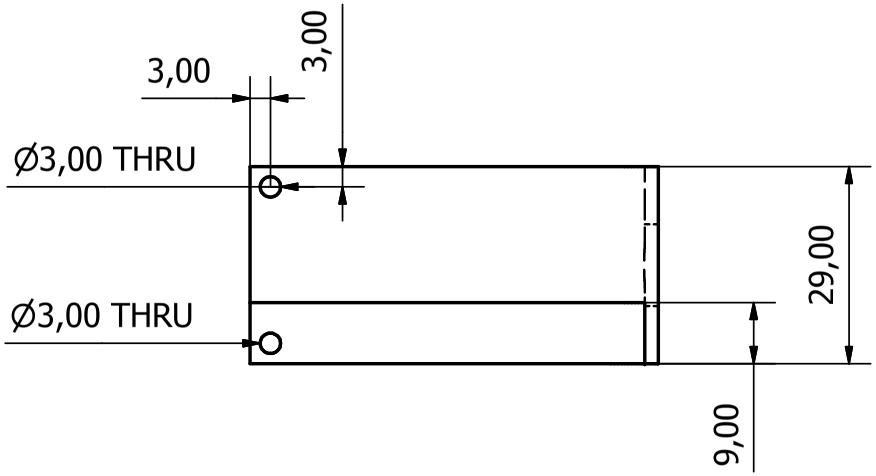

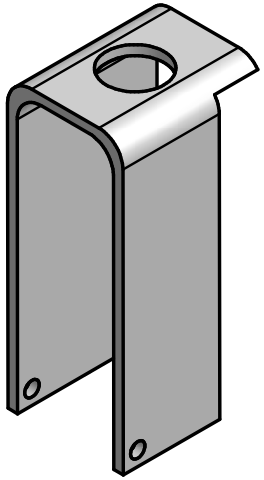

(1 : 1)

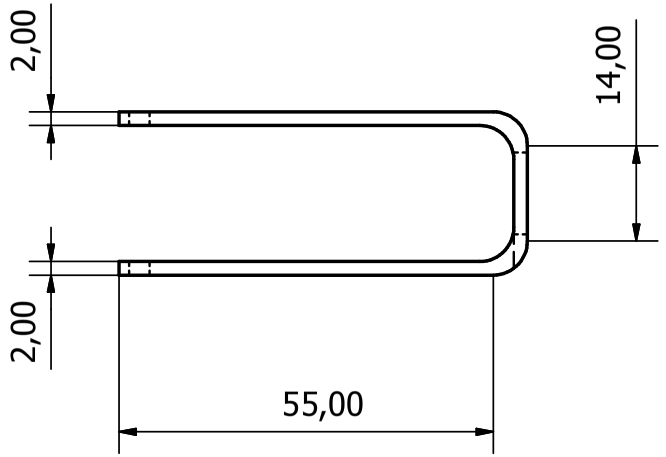

Designed by	Checked by	Approved by	Date		Date	
MSSAS						

DTU Space	Pharos 2.0 - Control board cover		
	board cover	Edition	Sheet 1 / 1

APPENDIX C

Vision Lab Extras

C.1 REAL SKY TEST OF THE M-061.PD ROTARY TABLE

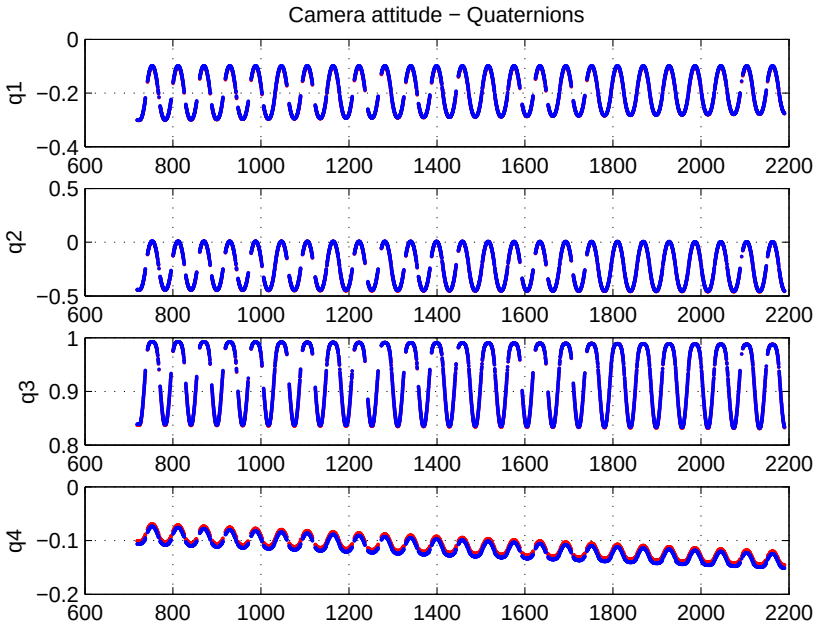

Figure C.1: Cameras telemetry attitude quaternions.

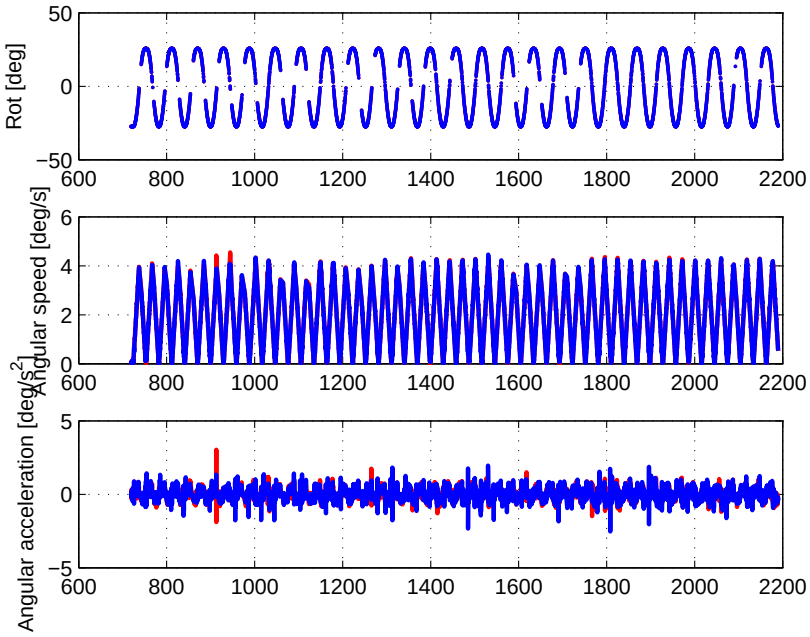

Figure C.2: Cameras telemetry motion profiles.

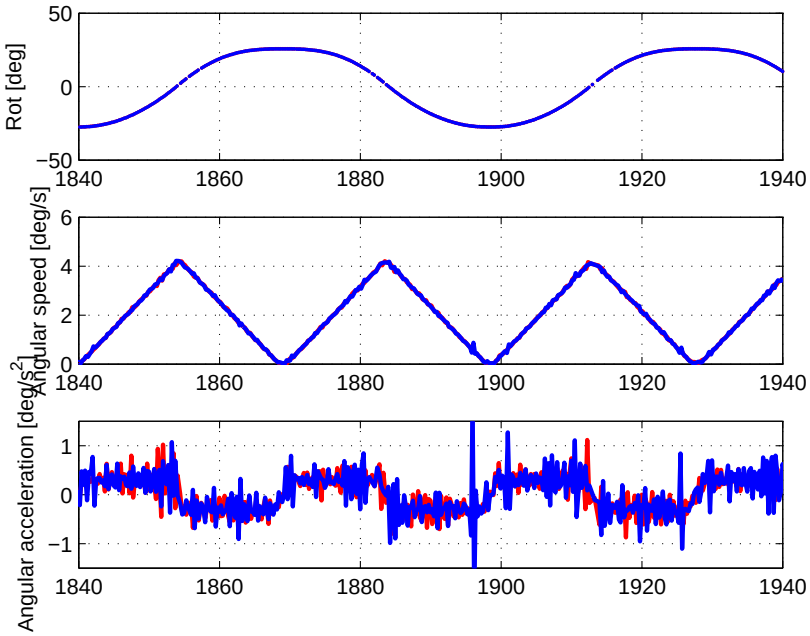

Figure C.3: Cameras telemetry zoomed motion profiles.

C.2 MECHANICAL INTERFACE ELEMENTS DRAWINGS

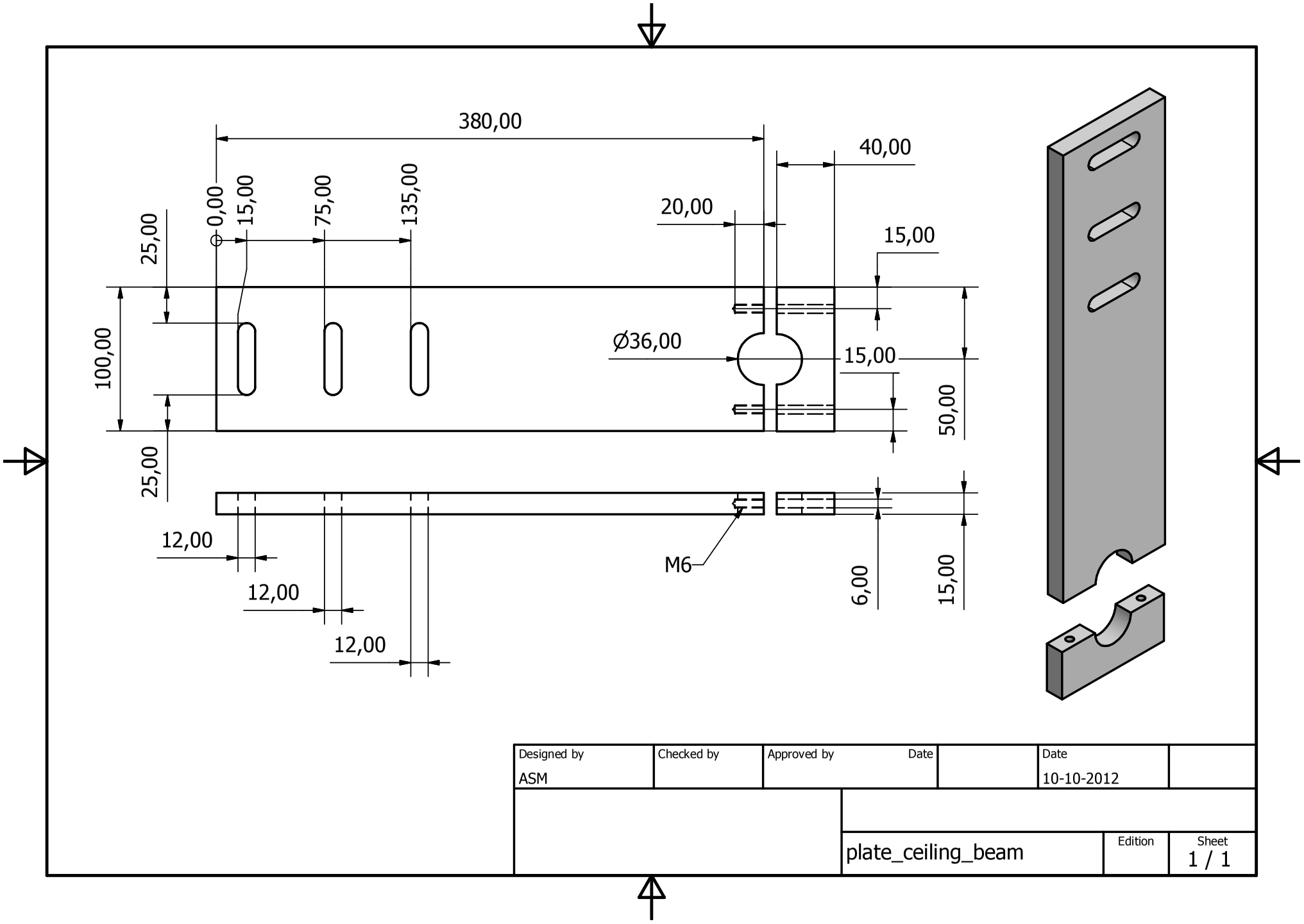

Designed by	Checked by	Approved by	Date		Date	
ASM					10-10-2012	

plate_ceiling_beam	Edition	Sheet
		1 / 1

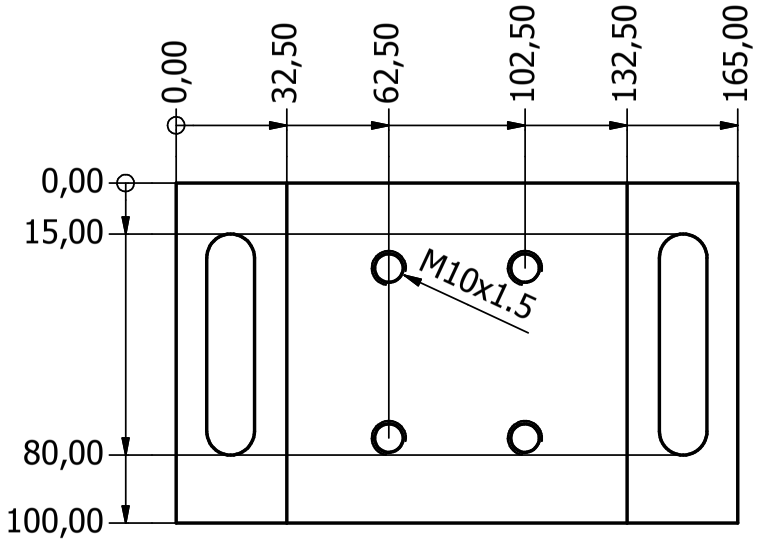

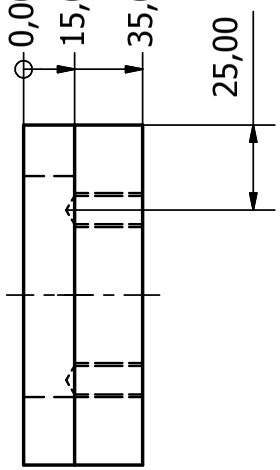

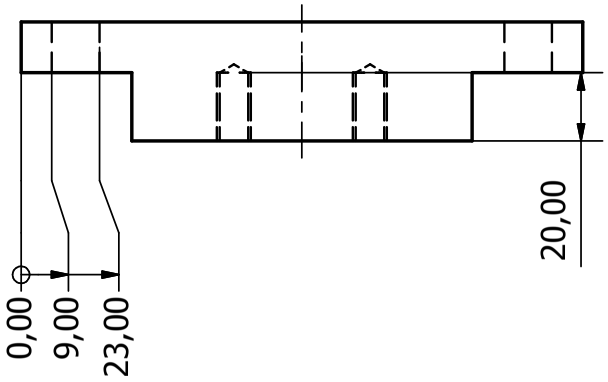

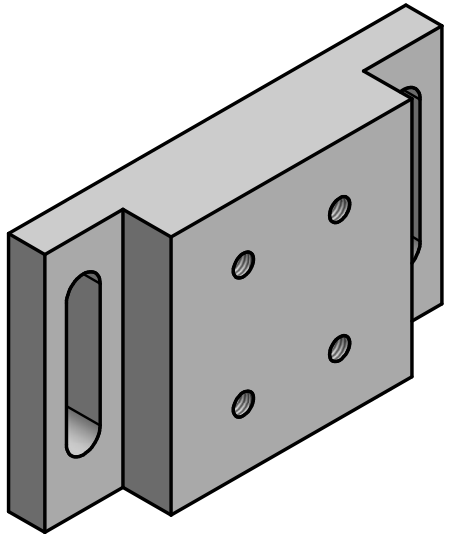

Designed by	Checked by	Approved by	Date		Date	
ASM					19-10-2012	

plate_ceiling_beam_right_wall	Edition	Sheet	1 / 1

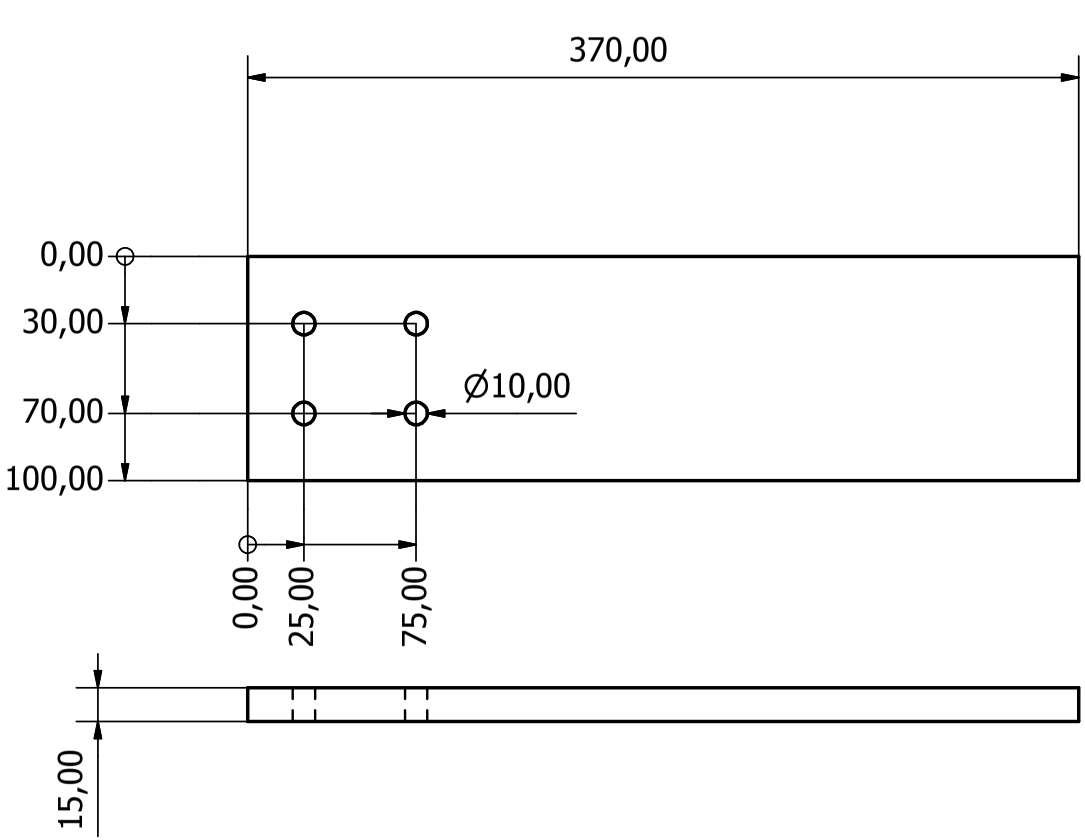

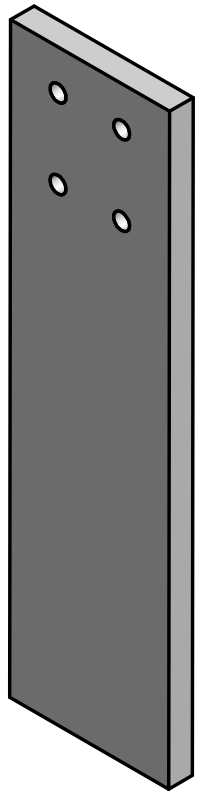

Designed by	Checked by	Approved by	Date		Date	
ASM					19-10-2012	

plate_ceiling_beam_right2	Edition	Sheet 1 / 1	

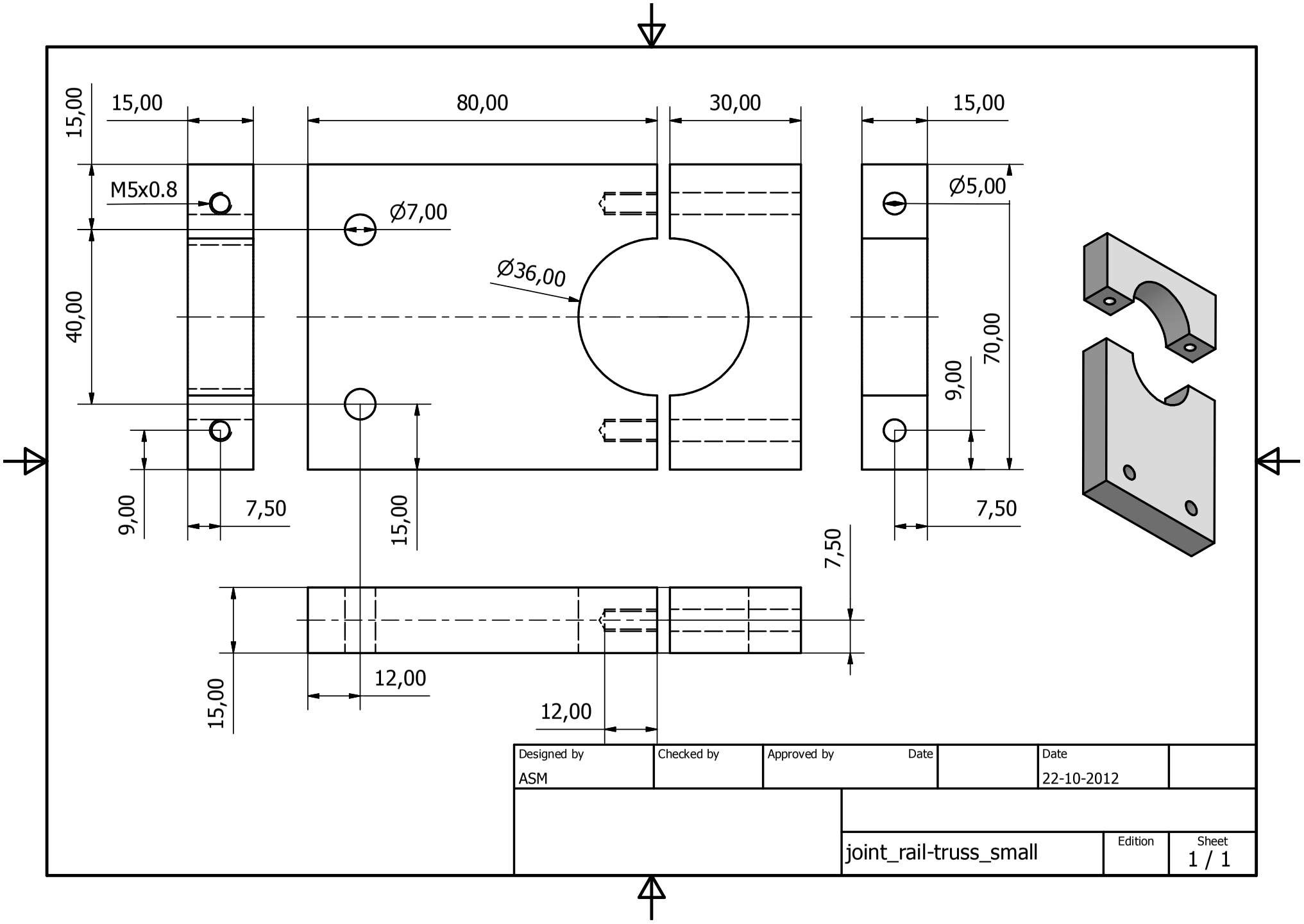
15,00
15,00
80,00
30,00
15,00
M5x0.8
Ø7,00
Ø36,00
Ø5,00
40,00
70,00
9,00
9,00
7,50
15,00
7,50
7,50
12,00
15,00
12,00
Designed by
ASM
Checked by
Approved by
Date
Date
22-10-2012
joint_rail-truss_small
Edition
Sheet
1 / 1

C.3 FINAL RESULT

Figure C.4: Facility view from the control area.

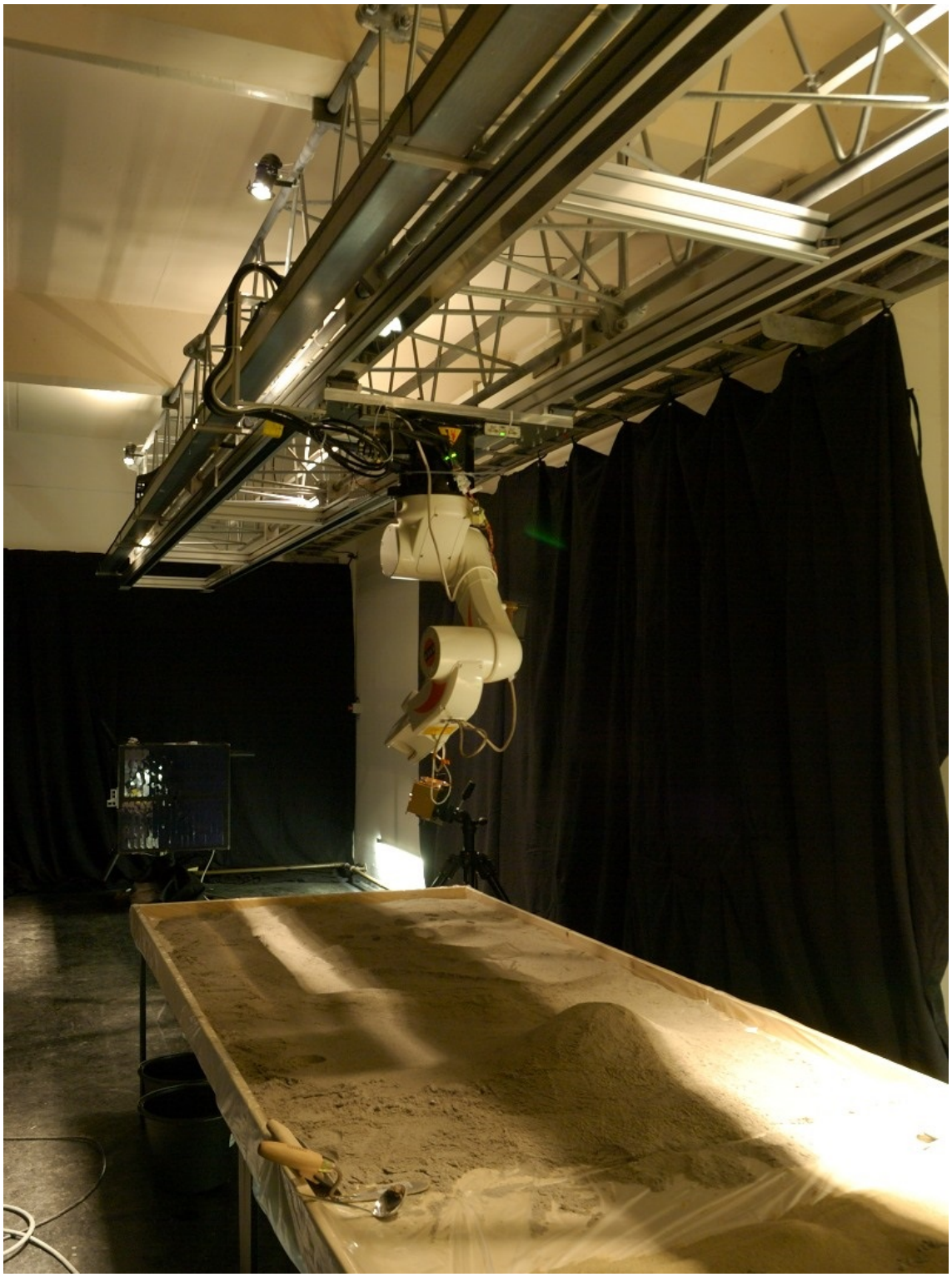

Figure C.5: Facility view from within test area.

Bibliography

Abidi, M. A. and Chandra, T. (1990). Pose estimation for camera calibration and landmark tracking. In *IEEE International Conference on Robotics and Automation*, pages 420–426.

Benn, M. (2010). *Vision Based Navigation Sensors for Spacecraft Rendezvous and Docking*. PhD thesis, Technical University of Denmark.

Besl, P. J. and McKay, N. D. (1992). A method for registration of 3-d shapes. *IEEE Transactions on Pattern Analysis and Machine Intelligence*, 14(2):239–256.

Bjarnø, J. B. (2010). *Attitude Fusion Techniques for Spacecraft*. PhD thesis, Technical University of Denmark.

Brown, D. C. (1966). Decentering distortion of lenses. *Photometric Engineering*, 32(3):444–462.

Carpenter, J. D., Fisackerly, R., Pradier, A., Houdou, B., De Rosa, D., Vanoutryve, B., Jojaghaian, A., Espinasse, S., and Gardini, B. (2010). Objectives and Model Payload for Human Exploration Preparation on ESA's First Lunar Lander. *International Astronautical Congress 2010, Prague, Czech Republic*.

Cheng, Y. and Ansar, A. (2005). Landmark based position estimation for pinpoint landing on mars. In *Proceedings of the 2005 IEEE International Conference on Robotics and Automation, ICRA 2005, April 18-22, 2005, Barcelona, Spain*, pages 4470–4475. IEEE.

Fehse, W. (2003). *Automated Rendezvous and Docking of Spacecraft*. Cambridge University Press.

Forsyth, D. A. and Ponce, J. (2003). *Computer Vision: A Modern Approach*. Prentice Hall.

Harris, C. and Stephens, M. (1988). A combined corner and edge detector. In *In Proc. of Fourth Alvey Vision Conference*, pages 147–151.

Horn, B. K. P. (1986). *Robot Vision*. MIT Press.

Irani, M. and Anandan, P. (1999). About direct methods. *ICCV Workshop on Vision Algorithms*, pages 267–277.

Johnson, A. E., Huertas, A., Werner, R. A., and Montgomery, J. F. (2008). Analysis of on-board hazard detection and avoidance for safe lunar landing. In *Aerospace Conference, 2008 IEEE*, pages 1–9.

Johnson, A. E. and Montgomery, J. F. (2008). Overview of terrain relative navigation approaches for precise lunar landing. In *Aerospace Conference, 2008 IEEE*, pages 1–10.

Kjaergaard, M., Massaro, A. S., Bayramoglu, E., and Jensen, K. (2011). Terrain mapping and obstacle detection using gaussian processes. In *IEEE International Conference on Machine Learning and Applications, ICMLA 2011*, volume 1, pages 118–123.

Lowe, D. G. (2004). Distinctive image features from scale-invariant keypoints. *Int. J. Comput. Vision*, 60(2):91–110.

Maass, B., Kruger, H., and Theil, S. (2011). An edge-free, scale-, pose- and illumination-invariant approach to crater detection for spacecraft navigation. In *7th International Symposium on Image and Signal Processing and Analysis (ISPA), 2011*, pages 603–608.

Massaro, A. S. (2009). Remote operator-assisted visual navigation system for a rover. Master's thesis, Technical University of Denmark.

Massaro, A. S., Jørgensen, J. L., and Benn, M. (2009). Test report of the final PRISMA SW load campaign. Technical report, DTU Space.

Matthies, L., Huertas, A., Cheng, Y., and Johnson, A. E. (2008). Stereo vision and shadow analysis for landing hazard detection. In *IEEE International Conference on Robotics and Automation, ICRA 2008, May 19-23, 2008, Pasadena, California, USA*, pages 2735–2742. IEEE.

McEwen, A. S. (1991). Photometric functions for photoclinometry and other applications. *ICARUS 92*, pages 298–311.

Minnaert, M. (1941). The reciprocity principle in lunar photometry. *Astrophysical Journal*, 93:403–410.

Mourikis, A. I., Trawny, N., Roumeliotis, S. I., Johnson, A. E., Ansar, A., and Matthies, L. (2009). Vision-aided inertial navigation for spacecraft entry, descent, and landing. *IEEE Transactions on Robotics*, 25(2):264–280.

Mourikis, A. I., Trawny, N., Roumeliotis, S. I., Johnson, A. E., and Matthies, L. (2007). Vision-aided inertial navigation for precise planetary landing: Analysis and experiments. In *Robotics: Science and Systems III, June 27-30, 2007, Georgia Institute of Technology, Atlanta, Georgia, USA*. The MIT Press.

Muja, M. and Lowe, D. G. (2009). Fast approximate nearest neighbors with automatic algorithm configuration. In *International Conference on Computer Vision Theory and Application VISSAPP'09)*, pages 331–340. INSTICC Press.

Plescia, J. B. (2008). Lunar surface properties: what do we know, what don't we know, and what do we need to know? In *NLSI Lunar Science Conference*.

Rosten, E. and Drummond, T. (2006). Machine learning for high-speed corner detection. In *European Conference on Computer Vision*, volume 1, pages 430–443.

Shi, J. and Tomasi, C. (1994). Good features to track. In *IEEE Conference on Computer Vision and Pattern Recognition*, pages 593–600.

Shuster, M. D. (1993). A survey of attitude representations. *The Journal of the Astronautical Sciences*, Vol. 41, No. 4:439–517.

Torr, P. H. S. and Zisserman, A. (1999). Feature based methods for structure and motion estimation. *ICCV Workshop on Vision Algorithms*, pages 278–294.

Urbach, E. and Stepinski, T. (2009). Automatic detection of sub-km craters in high resolution planetary images. *Planetary and Space Science*, 57:880–887.

Xiong, Y., Olson, C. F., and Matthies, L. (2005). Computing depth maps from descent images. *Machine Vision and Applications*, 16(3):139–147.